SYNTHESIS AND FUNCTIONALISATION OF ONE-DIMENSIONAL TITANATE-BASED NANOSTRUCTURES

Ines Bračko

Doctoral Dissertation
Jožef Stefan International Postgraduate School
Ljubljana, Slovenia, June 2012

Evaluation Board:

Prof. Dr. Miran Čeh, Chairman, Nanostructured Materials Department, Jožef Stefan Institute, Jamova 39, Ljubljana, Slovenia

Prof. Dr. Maja Remškar, *Member, Condensed Matter Physics, Jožef Stefan Institute, Jamova 39, Ljubljana, Slovenia*

Prof. Dr. Dragan P. Uskoković, *Member, Institute of Technical Sciences of SASA, Knez-Mihailova 35/IV, Belgrade, Serbia*

MEDNARODNA PODIPLOMSKA ŠOLA JOŽEFA STEFANA
JOŽEF STEFAN INTERNATIONAL POSTGRADUATE SCHOOL

Ines Bračko

SYNTHESIS AND FUNCTIONALISATION OF ONE-DIMENSIONAL TITANATE-BASED NANOSTRUCTURES

Doctoral Dissertation

SINTEZA IN FUNKCIONALIZACIJA ENODIMENZIONALNIH TITANATNIH NANOSTRUKTUR

Doktorska disertacija

Supervisor: Prof. Dr. Danilo Suvorov

Co-Supervisor: Assist. Prof. Dr. Boštjan Jančar

Ljubljana, Slovenia, July 2012

Index

Abstract

One-dimensional hydrothermally synthesized nanostructures such as nanotubes and nanobelts composed of layered titanates from $A_2Ti_nO_{2n+1}$ family have attracted great interest due to their high specific surface area, ion-exchange ability and semiconducting properties, which make them promising candidates for potential applications in the field of catalysis, gas sensors, dye-sensitized solar cells, lithium batteries and photocatalysis.

Titanate-based one-dimensional (1D) nanostructures are characterized as a layered, lamellar structure with mesoporous morphology, which may facilitate the transport of ions to the surface of the elongated nanostructures. The ability of ion-exchange of titanate-based 1D nanostructures has been utilized for the formation of Ca-doped titanate nanotubes and nanostructured $CaTiO_3$. Implementation of titanate nanotubes as a template material ensures formation of modified or new materials of nano-dimensions with elongated structure inherited from the parent nanotubes.

In the field of photocatalysis several approaches that modify electron band structure of titanates have been successfully introduced to enhance the photosensitivity of titanate-based 1D nanostructures in the UV and visible regime. Recently, the increased photoactivity in the visible range was observed with the metallic nanoparticles/titanate nanocomposites.

Polyelectrolyte multilayer (PEM) film of desired thickness formed by the layer-by-layer self assembly of appositively charged polyions assembled on the surface of the one-dimensional titanate-based nanostructures can be utilized as nanoreactor for the *in-situ* synthesis of metallic nanoparticles. By this approach the surrounding polymer prevents aggregation of formed nanoparticles within PEM film and thus enables a control over the size and density of metallic nanoparticles in the nanocomposite.

The weak PEMs of polyallylamine (PAH) and polyacrylic acid (PAA) possessing ion-exchangeable carboxylic groups were assembled on hydrophilic surface of titanate-based nanobelts by the sequential deposition of polyions from an aqueous solution. PEM films fabricated by Layer by Layer (LbL) electrostatic assembly of weak appositively charged polyions were used to bind metal cations within the PEM film. The free carboxylic acid groups that do not electrostatically bind to the appositively charged groups of PAH during the film assembly are later used to bind the metal ions as the PEM is exposed to the metal salt solution at the nominally neutral pH. By subsequent chemical reaction of the metal ions, metallic (Ag, Cu) nanoparticles are formed within the PEMs. Due to the regeneration of the carboxylic acid groups upon nanoparticle formation, the control over the volume fraction, the size and the density of the particles within the polymer film was obtained by repeatedly cycling the synthesis process. By subsequent thermal treatment PEM is removed resulting in the metallic Ag(Cu) nanoparticles-titanate nanobelts composite formation.

Under photo-excitation the metallic nanoparticles in the composite act as electron traps and hence suppress the electron-hole recombination rate in the semiconductor (titanate nanobelts) and thus enhance photo-response of such hybrid material in UV region of solar spectrum. Additionally, visible photo-activity of metal-1D titanate nanostructures nanocomposites is obtained by the electromagnetic near field induced by the surface

plasmon resonance (SPR) of metallic (Ag, Cu) nanoparticles.

Furthermore, the PEM films formed by the layer-by-layer self assembly on the surface of titanate nanobelts were utilized for the fabrication procedure of titanate nanobelts thin films. Organic-inorganic PEM-titanate nanobelts composite was assembled in sequential steps with fully charged polyelectrolyte Poly(styrenesulfonic acid) (PSS) to fabricate 10 and 20 bilayered film assemblies. By applying PEM onto the surface of titanate nanobelts the negative surface charge of hydrophilic titanate nanobelts become positive which then enables electrostatic coupling with strongly negatively charged PSS polyelectrolyte yielding inorganic-organic multilayered thin film with linear film thickness increment as the number of layers was increased. After annealing at 450°C the inorganic films are composed solely of crystalline titanate nanobelts that are not oriented parallel with the substrate. Random orientation of nanostructures building as-formed thin film induces nanoscale porosity and hence renders these multilayers potentially effective photo-sensitive materials for the degradation of organic pollutants.

Povzetek

Raziskave na področju priprave in funkcionalizacije hidrotermalno sintetiziranih enodimenzionalnih nanostruktur z morfologijo nanocevk in nanotrakov na osnovi plastovitih alkalijskih titanatov s splošno formulo $A_2Ti_nO_{2n+1}$ so v zadnjem času pritegnile veliko pozornosti zaradi visoke specifične površine, dobre zmožnosti ionske izmenjave in polprevodniškega značaja titanatnih enodimenzionalnih nanostruktur in možnosti aplikacij le-teh na področju sončnih celic, plinskih senzorjev, heterogene katalize, litijevih baterij in fotokatalitskih procesov.

Hidrotermalno sintetizirane nanocevke na osnovi alkalijskih titanatov imajo plastovito, lamelarno strukturo in značilno odprto, mezoporozno morfologijo, ki omogoča prenos nabitih specij med plastmi, ki tvorijo stene večplastnih nanocevk, in na površino nanocevk. Uporaba takšnih enodimenzionalnih nanostrukturiranih templatov v nadaljnih procesih omogoča pripravo novih materialov in enodimenzionalnih produktov nanodimenzij, ki so prevzeli/ohranili morfologijo templata, vendar jih odlikujejo spremenjene lastnosti, kot so fotoaktivnost, biokompatibilnost in bioaktivnost. Zaradi njihove morfologije in zmožnosti ionske izmenjave smo titanatne nanocevke uporabili kot templat za pripravo s kalcijem dopiranih titanatnih nanocevk in nanostrukturiranega $CaTiO_3$.

Glede na že raziskane in znane fotokatalitske lastnosti TiO_2 je v zadnjih letih veliko raziskav usmerjenih tudi v študij in prilagajanje lastnosti titanatnih enodimenzionalnih nanostruktur za uporabo v fotokatalitskih procesih. Modificiranje elektronske strukture nanostrukturiranih titanatov z dopiranjem z različnimi specijami omogoča prilagajanje lastnosti titanatnih nanocevk in posledično poveča njihovo fotoobčutljivost v UV in predvsem v vidnem območju sončevega spektra. Še posebej za povečanje fotoodziva v vidnem območju pa se je izkazala kot uspešen pristop priprava nanokompozitov na osnovi kovinskih nanodelcev in polprevodniških nanostruktur.

Za kontrolirano pripravo nanokompozitov na osnovi kovinskih nanodelcev in polprevodniških nanostruktur smo uporabili večplastno polielektrolitno matrico pripravljeno z "Layer-by-Layer self assembly" metodo. Takšna organska matrica, nanešena na površino polprevodniške komponente nanokompozita, to je titanatnih nanotrakov, lahko deluje kot nanoreaktor za *in-situ* sintezo kovinskih nanodelcev. Dodatno organska matrica omogoča sterično stabilizacijo kovinskih nanodelcev, ki preprečuje njihovo aglomeracijo, in s tem kontrolo velikosti in gostote kovinskih nanodelcev v nanokompozitu.

Večplastni polielektrolitni nanos smo nanesli na hidrofilno površino titanatnih nanotrakov z izmeničnim nanašanjem šibkega polikationa polialil amina (PAH) in šibkega polianiona poliakrilne kisline (PAA) na osnovi elektrostatskega privlaka. Večplastni polielektrolitni nanos nam je služil za vezavo kovinskih (Ag, Cu) kationov iz vodnih raztopin njihovih soli. V večplastni matrici so prisotne proste funkcionalne skupine, ki se med pripravo večplastnega polielektrolitnega filma niso elektrostatsko vezale s funkcionalno skupino nasprotno nabitega poliiona in delujejo kot vezna mesta za kovinske ione. Z reakcijo redukcije se vezani kovinski kationi pretvorijo v kovinske (Ag in Cu) nanodelce. Pri tem se karboksilne skupine regenerirajo in so ponovno na voljo za

vezavo novih kovinskih kationov. Takšno ponavljanje sinteznih korakov (ciklov) omogoča kontrolo volumskega deleža, velikosti in gostote kovinskih nanodelcev v večplastnem polimernem filmu. Termična obdelava organsko/anorganskega kompozita rezultira v odstranitev organskega večplastnega nanosa in nastanek kristaliničnega anorganskega kompozita na osnovi kovinskih Ag (Cu) nanodelcev in titanatnih nanotrakov. Foto-vzbujeni kovinski delci delujejo kot past za elektrone, pri čemer se hitrost rekombinacije elektron-luknja v polprevodniku (titanatnih nanotrakovih) upočasni in vodi v povečan foto-odziv takšnega hibridnega materiala v UV območju svetlobe. Prav tako nanokompozit kovina-polprevodnik izkazuje povečan foto-odziv v vidnem območju svetlobe, kjer je foto-aktivnost posledica elektromagnetnega polja v bližini kovinskega (Ag, Cu) delca, ki ga povzroči površinska plazmonska resonanca delca.

Polielektrolitne nanose, nanešene na površino titanatnih nanotrakov z Layer-by-Layer metodo, smo uporabili za pripravo tankih plasti titanatnih nanotrakov. Kompozit na osnovi večplastnega polielektrolitnega nanosa in titanatnih nanotrakov smo nanašali na silicijevo podlago z zaporednimi nanosi kompozita in popolnoma nabitega polielektrolita polistiren sulfonske kisline (PSS), da smo dosegli 10 in 20 dvojnih plasti debel tanek film. Z zaporednim nanosom nasprotno nabitih komponent debelina tankega filma linearno narašča s povečevanjem števila nanešenih plasti. S termično obdelavo odstranimo organski del tanke plasti in kot rezultat dobimo tanko plast, ki sestoji iz titanatnih nanotrakov, ki pa niso orinetirani/poravnani vzporedno s silicijevo podlago. Naključna orientacija nanotrakov v tanki plasti na podlagi povzroči prisotnost nanoporoznosti ter s tem odpira možnosti za uporabo takšnih plasti kot potencialno učinkovitih materialov za razgradnjo organskih polutantov v vodah in zraku.

Abbreviations

SPR	=	Surface plasmon resonance
LSPR	=	Local surface plasmon resonance
DDA	=	Discrete dipole approximation
XRD	=	X-ray powder diffraction
TEM	=	Transmission electron microscopy
HRTEM	=	High-resolution transmission electron microscopy
SAED	=	Selected area electron diffraction
FESEM	=	Field-emission scanning electron microscopy
AFM	=	Atomic force microscopy
UV-vis	=	Ultraviolet-visible
QD	=	Quantum dot
Ti-NBs	=	Titanate-based nanobelts
Ti-NTs	=	Titanate-based nanotubes
Ag(N)/Ti-NBs	=	Ag nanoparticles/titanate-based nanobelts composite
Cu/Ti-NBs	=	Cu nanoparticles/titanate-based nanobelts composite
Ca/Ti-NTs	=	Ca^{2+} doped titanate-based nanotubes
PAA	=	Poly(acrylic acid)
PAH	=	Poly(allylaminehydroxide chloride)
PDDA	=	Poly(diallyldimethylammonium chloride)
PSS	=	Poly(styrenesulfonic acid)
PE	=	Polyelectrolyte
PEM	=	Polyelectrolyte multilayer
LbL	=	Layer-by-Layer polyelectrolyte method
MB	=	Methylene blue

1 Introduction

1.1 Nano-meter sized materials

Nanostructured materials are found in a wide variety of shapes such are spheres and polyhedrons, cylindrical tubes and fibres, or random and regular pores in solids. [1] Development and controlled fabrication of nanostructured materials with functional properties have attracted considerable interest in research community due to their unique behaviour and due to their potential for numerous applications. Physical, chemical, electronic and magnetic properties of nano-meter sized materials differ from their bulk properties. A broad range of phenomena obtained in nanostructures such as size–dependent excitation, ballistic conductance, and Coulomb blockade or single electron tunnelling originate from nano-meter sized dimensions. [2] By reducing the dimensions of the material the increased surface to volume ratio leads to the dominance of the surface atoms over the interior atoms influencing the surface energy of nano-scale materials due to the strongly lowered cohesive energy of incompletely bonded surface atoms. Together with confinement effects, at a nano-scale, the vast surface area can dominantly determine the properties of nano-sized materials. High surface area is advantageous for catalytic processes where the catalytic reactions occur on the surface of the catalyst.

Nanoscale one-dimensional (1D) materials have attracted great interest due to their importance in basic scientific research representing an ideal system for investigating the size and dimensionality dependence of electrical and mechanical properties and are expected to play an important role as interconnects and functional components in nanodevices. [2] Much of the interest in 1D nanostructured materials, especially in nano-tubular materials, was initiated by discovery of carbon nanotubes in the 1991 by Iijima [3] and it has been shown that many layered materials are able to form nanotubes [4].

1.1.1 One-dimensional (1D) titanate-based nanostructures: nanotubes (Ti-NTs) and nanobelts (Ti-NBs)

Nanostructured materials with elongated shapes i.e. 1D nanostructures are defined as shapes with aspect ratio greater than 10 where the aspect ratio is determined as the ratio of the elongated nanostructure's length to diameter. [1] However, 1D nanostructures are referred to various elongated morphologies: nanowires, nanofibres, nanorods, nanobelts, nanowhiskers, nanotubes, etc.

Among non-carbon 1D nanostructures the titanate nanotubes (Ti-NTs) and the titanate nanobelts (Ti-NBs) have been of particular interest. Ti-NTs and Ti-NBs are expected to exhibit enhanced physical and chemical properties in comparison to their respective bulk materials leading to a wide variety of potential applications. High specific surface area and high aspect ratio titanate-based 1D nanostructures have been studied as possible candidates for the catalyst supports in heterogeneous catalytic processes [5], the electrodes in dye-sensitized solar cells and rechargeable lithium batteries [6,7], and as materials for the photo-catalytic degradation of organic compounds [8, 9]. Titanate-based 1D nanostructures are characterized by the combination of properties of conventional

wide-band gap semiconductor TiO_2 and by the properties of bulk layered alkali metal titanates.

1.1.1.1 Crystallography of Ti-NTs and Ti-NBs

The alkali-metal titanates represented by the chemical formula $A_2Ti_nO_{2n+1}$ (A: Na, K, Cs, $3 \leq n \leq 9$) possess monoclinic symmetry and they have crystal structure of layered or tunnel-type titanates. Titanates with high alkali-metal content exhibit layered-type structure, while those with n = 6-9 show tunnel-type structure. In Figure 1 structures of layered-type $Na_2Ti_3O_7$ and tunnel-type $Na_2Ti_6O_{13}$ titanates are shown. The basic framework of layered-type is built up from three TiO_6 octahedra in one layer, and three at a distance *b/2* above and below, sharing edges at one level. These octahedra form blocks which are joined together through corners forming a two dimensional sheets with the $(Ti_3O_7)^{2-}$ composition held together by alkali-metal cations positioned in the interlayer space. [10, 11] The tunnel-type structure consists of blocks of the three through edges connected TiO_6 octahedra building a zig-zag ribbon extending in the *b* direction. Ribbons from one layer share all terminal corners with ribbons in levels above and below resulting in formation of tunnels with the alkali-metal cations situated along the channels. [12] The structure of alkali-metal titanates allows appreciable mobility of interlayer cations causing a good ion-exchange ability of layered-type titanates [10, 11], while the tunnel-type structured titanates exhibit higher thermal and chemical stability [13].

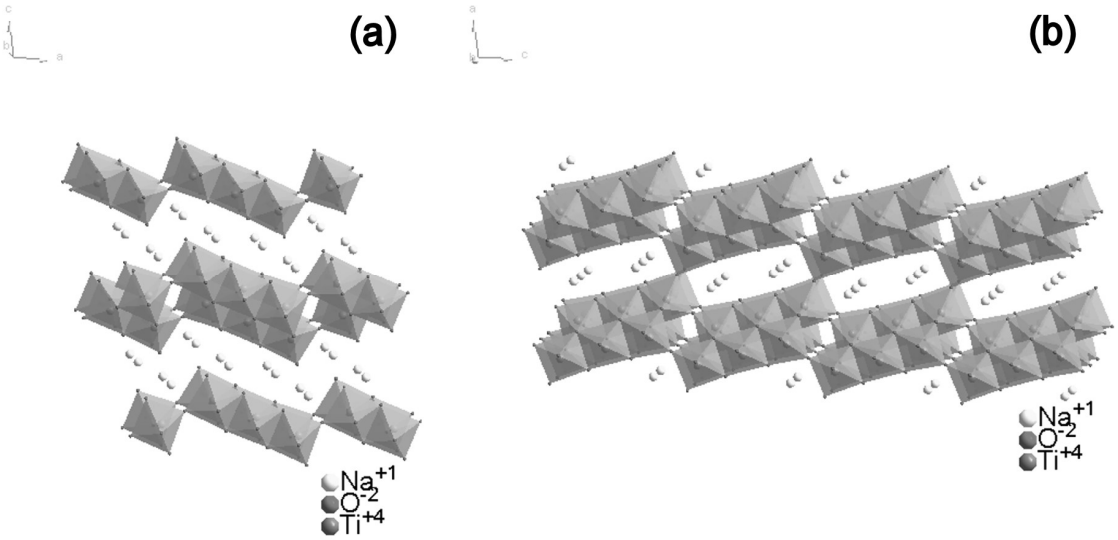

Figure 1: Crystal structure of alkali-metal titanates: (a) layer-type $Na_2Ti_3O_7$ and (b) tunnel-type $Na_2Ti_6O_{13}$.

Since the titanate nanotubes were hydrothermally synthesized for the first time by Kasuga et al. [14], they were characterized by tetragonal, monoclinic and orthorhombic symmetry. The crystal structure of 1D titanate-based nanostructures was interpreted, beside TiO_2 anatase [14, 15], as (Na or $H)_2Ti_2O_4(OH)_2$ [16, 17] $Na_2Ti_2O_5 \cdot H_2O$ [18], $A_2Ti_nO_{2n+1}$ (A: Na, H) [19, 20, 21, 22, 23] and lepidocrocite-type titanates $A_xTi_{2-x/4}\square_{x/4}O_4$ (A: Na or/and H, □: vacancy) [24, 25, 26]. Till today, in the international research community, the exact crystal structure of titanate-based 1D nanostructures is still under discussion. The exact determination of crystal structure of nanotubes is hindered by several difficulties arising from the nanostructures themselves. The small size of crystallites and the rolling of the nanosheets along certain crystallographic axis result in broadening of the XRD peaks and appearance of diffuse rings in SEAD patterns. Additionally, the low weight of hydrogen and sodium atoms render difficult to determine

their exact position and content in the structure.

Based on powder X-ray diffraction (XRD), differential thermogravimetric analysis (DTG), differential scanning calorimetric measurement (DSC), high-resolution transmission electron microscopy (HRTEM) and selected-area electron diffraction (SAED) the (Na or H)$_2$Ti$_2$O$_4$(OH)$_2$ nanotubes were characterized by layered structure of orthorhombic symmetry with the lattice constants a_0 = 19.26 Å, b_0 = 3.78 Å and c_0 = 3.00 Å. [16, 17] The nanotubes are formed by rolling of (100) plane around the *b* direction leading in the formation of multi-layered walls. The radial direction and the axis of the nanotubes correspond to *a* and *b* axis of the orthorhombic dititanate, respectively. [1] The obtained distances of 0.74 – 0.96 nm between adjacent layers building walls of the nanotubes correspond to the d_{200}. The variations in the interlayer distance are related to the dehydration of interlayered OH groups (Equation 1). [16, 17]

$$Na_2Ti_2O_4(OH)_2 \rightarrow Na_2Ti_2O_5 + H_2O \quad (1)$$

Second proposed model describing the crystal structure of titanate nanotubes is based on the lepidocrocite-type titanates with general formula of $A_xTi_{2-x/4}\square_{x/4}O_4$ (A: Na or/and H, □: vacancy). Nanotubes are formed by rolling of lepidocrocite (γ-FeOOH)-type sheets in (010) plane along [001] direction. The tube axis is parallel to [200] direction. [26, 27] Lepidocrocite-type layers are two-dimensional sheets built of edge-sharing TiO_6 octahedra forming flat layers situated at *a* x *c* planes [24] as shown in Figure 2. The peaks in XRD pattern were indexed to a orthorhombic $H_xTi_{2-x/4}\square_{x/4}O_4 \cdot H_2O$ with lattice parameters *a* = 3.783 Å, *b* = 18.735 Å and *c* = 2.978 Å. [26] The peaks in the XRD patterns can be assign to the reflections of the basal inter-layer (0*k*0) series and in-layer (200) and (002) planes of the orthorhombic lepidocrocite-type titanate. [25] Furthermore, the radial distribution of atoms (RDA) function calculated from extended X-ray absorption fine structure (EXAFS) spectra implies that the local structure of nanotubes might be closer to the lepidocrocite titanates. [25]

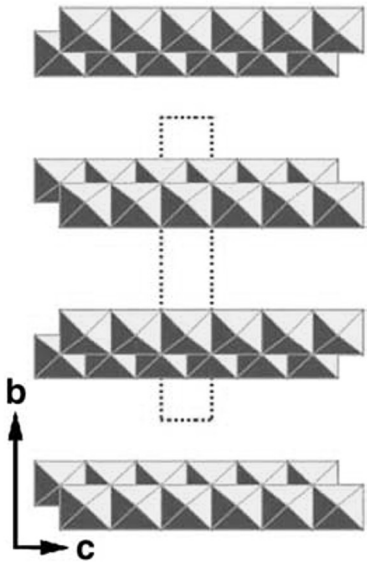

Figure 2: Structure model of lepidocrocite-type $A_xTi_{2-x/4}\square_{x/4}O_4$ titanate.

However, nowadays the most widely accepted structure model is the trititanate nanotube model. [27] Based on detailed XRD, SAED and HRTEM studies combined by structure simulations it was proposed that crystal structure of nanotubes corresponds to the $H_2Ti_3O_7$. [21, 28] The layered trititanate acid has monoclinic crystal structure with lattice parameters: a = 16.02 Å, b = 3.75 Å, c = 9.19 Å and β = 101.5°. [1] In Figure 3 shown structure of trititanate $H_2Ti_3O_7$ is composed of corrugated ribbons. Three edge-sharing TiO_6 octahedra wide ribbons are joined through corners to form stepped sheets that are separated by H^+ ions.

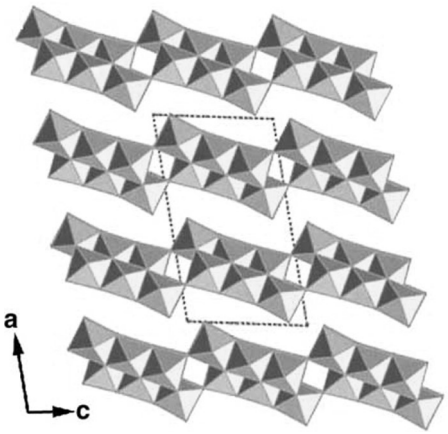

Figure 3: The structure of layered titanate $H_2Ti_3O_7$. Unit cell is indicated by dashed lines.

Nanotubes are multi-walled scrolls formed by rolling of (100) $(Ti_3O_7)^{2-}$ sheets along [001] direction of the $H_2Ti_3O_7$ structure. [20, 21] Obtained nanotubes have tube axis parallel to the axis *b* of monoclinic $H_2Ti_3O_7$. The radial direction from the centre of the tube towards the walls correspond to the *a* axis of the trititanate, and the tangential direction to the nanotube surface corresponds to axis *c*. [1]

By the hydrothermal treatment of TiO_2 in highly alkaline environment the fibrous rather than tubular nanostructures such as nanorods, nanobelts, nanowhiskers, nanoribbons and nanowires can be obtained. According to literature, the crystal structure of these fibrous nanostructures corresponds to the structures of various layered titanates including $A_2Ti_nO_{2n+1}$, where A stands for Na or H and n equals 3, 5, 6 or 8 [29, 30, 31, 32, 33, 34, 35, 36], lepidocrocite-type titanates [25, 37] and $NaTi_3O_6(OH)\cdot H_2O$ titanate [38]. Although there is still no consensus on exact crystal structures of hydrothermally synthesized fibrous titanates it is generally accepted that these nanostructures are layered structures consisting of parallel (100) planes with the interplanar distance corresponding to the characteristic interlayer spacing d_{200} which is intrinsic to all layered titanates. [1, 35] The single-crystalline nanoribbons/nanobelts indexed to monoclinic phase of $Na_2Ti_5O_{11}\cdot H_2O$ grow along the [002] direction showing layered structure with the characteristic interplanar distance of 0.82 nm, which corresponds to the *d*-spacing of the (200) plane. [29, 36] The rectangular morphology of these nanobelts originates from the intrinsic structural anisotropy and variation in growth rates of the three principal directions (001, 100 and 010). [36] The nanobelts' structure is composed of corrugated blocks built of five edge-sharing TiO_6 octahedra. Five octahedral wide blocks are further joined through corners to form stepped layers. Similarly, the main building blocks of nanobelts characterized by monoclinic layered $A_2Ti_3O_7$ and tunnel-type $A_2Ti_6O_{13}$ titanates are TiO_6 octahedra, which share edges to form three octahedral wide one-dimensional slabs. These slabs form stepped two-dimensional network by sharing octahedral corners. In tunnel-type titanates, one-dimensional blocks in one layer share corners with slabs

from layers above and below thus forming tunnels. [33, 34, 39] According to the XRD and SAED, the diffraction peak at $2\Theta = 11°$ corresponds to the (100) $A_2Ti_3O_7$ titanate plane indicating growth of nanobelts in this direction, which is one of the two prominent growth directions; i.e. [100] and [001]. [33, 34] The SAED pattern of monoclinic tunnel-type $A_2Ti_6O_{13}$ titanate nanobelts reveals elongation along the [010] direction with the two-dimensional framework built of TiO_6 octahedra running in [100] direction, parallel to the elongation of a nanobelts. [39]

In contrast to the monoclinic trititanates, which have corrugated layers built of three octahedra wide one-dimensional slabs, the lepidocrocite titanate lattice, $A_xTi_{2-x/4}\square_{x/4}O_4$ (A: $x \sim 0.7$, □: vacancy) belongs to the orthorhombic system and it consists of continuous two-dimensional layers of TiO_6 octahedra connected to each other via edges and cations situated between layers as shown in Figure 2. [1, 37] The SAED pattern indexed to (200) and (110) diffraction planes of the lepidocrocite structure was in agreement with obtained XRD and Raman results. [37]

In addition, according to XRD analysis the structure was also ascribed to the structures of titania polymorphs TiO_2(B), TiO_2 anatase and TiO_2 rutile. [32, 40] However, the synthesis procedure for formation of nanowires with TiO_2(B) or TiO_2 anatase structure includes post-heat treatments by which hydrothermally synthesized titanate-based one-dimensional nanostructures are transformed into titania polymorphs but preserving the elongated morphology. The titanate-based nanowires transform to TiO_2(B) at 400°C, followed by the transformation to anatase at 600°C and at 900°C rutile starts to form. [40]

However, recently electron diffraction data collected by automated diffraction tomography (ADT) technique were used for the *ab initio* structure determination of new phase of sodium titanate $NaTi_3O_6(OH)\cdot 2H_2O$, which was formed as an intermediate species in the synthesis of TiO_2 nanorods. [38] This type of titanate crystallizes in the monoclinic space group *C2/m*. The structure is composed of distorted TiO_6 and NaO_6 octahedra. In Figure 4 the individual TiO_6 octahedra sharing two common corners and six, four and five edges for Ti1, Ti2 and Ti3, respectively, are shown. Corrugated layers are built up from corner- and edge-sharing TiO_n polyhedra arranged parallel to the (001) plane. Based on the interatomic distances and thermogravimetric analysis combined with crystal chemistry considerations the final composition of $NaTi_3O_6(OH)\cdot 2H_2O$ assigned to this titanate phase includes one hydroxyl group and two water molecules. Since the $(Ti_3O_7)^{2-}$ layers are negatively charged the charge compensation is achieved by the intercalation of one hydrated sodium cation and a hydroxyl group in the space between two layers, while the water molecules situated in the interlayer space increase the ion-exchange ability of such materials by making their structure more open. In addition, edge dislocations and defects, such as mutual layer shifts, were obtained in the nanorods.

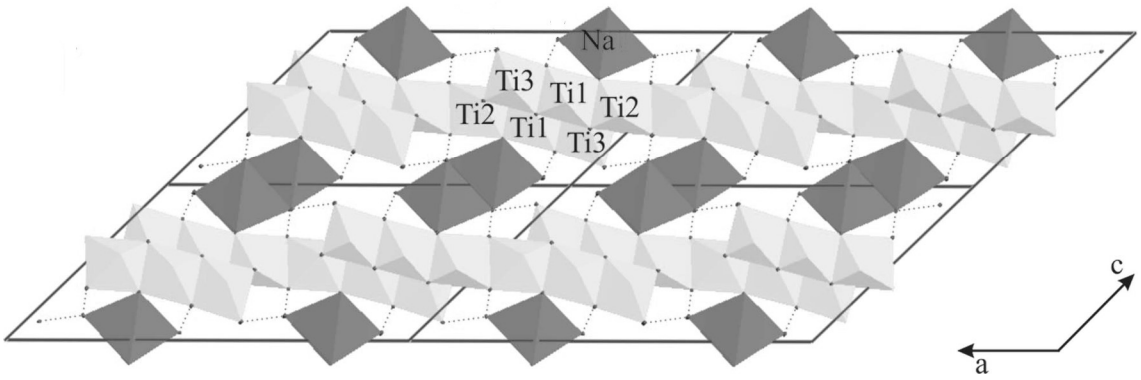

Figure 4: Model of $NaTi_3O_6(OH)\cdot 2H_2O$ crystal structure viewed in [010] direction.

1.1.1.2 Formation mechanisms of Ti-NTs and Ti-NBs under hydrothermal conditions

The exact formation mechanism of Ti-NTs and Ti-NBs formed under hydrothermal conditions is still controversial topic widely discussed in contemporary literature. Since the discovery of one-dimensional titanate-based nanostructures formed by wet-chemical methods, many attempts have been made towards understanding the formation mechanisms. However, it is now generally accepted that during transformation of three-dimensional TiO_2 (anatase, rutile, brookite or amorphous) structure under alkaline conditions maintained by concentrated NaOH, layered titanates in form of thin single- or multi-layered nanosheets are formed as intermediate phase playing a crucial role in the formation process of tubular nanostructures through folding/scrolling mechanism. [41, 42] The formation process proceeds through several stages. At the beginning of the formation reaction slow dissolution of TiO_2 powder, epitaxial growth and exfoliation of titanate nanosheets take place. In the next stage the nanosheets start to fold forming tubular nanostructures. As-formed nanotubes grow along their axis to reach the final dimensions. [41]

1.1.1.2.1 Formation mechanism of nanotubes: exfoliation/peeling and rolling of single-layered nanosheets

In this mechanism, the reaction of TiO_2 particles with highly concentrated NaOH solution under hydrothermal conditions starts by the diffusion of Na^+ and OH^- species towards the surface of TiO_2 particles causing the digestion of the particle's surface. Swelling and subsequent peel off of the surface leads to the formation of the titanate nanosheets followed by the rolling into nanotubes. [43] At the very beginning of the process, a highly disordered phase is formed. Inside the intermediate phase containing Na, Ti and O the formation of single sheets of $Ti_3O_7^{2-}$ or $Na_2Ti_3O_7$-like nanocrystals is plausible. If the formation of $Na_2Ti_3O_7$ nanocrystals is assumed, the excess of Na^+ cations intercalating in the interlayer space cause peeling of the single layers from the $Na_2Ti_3O_7$ nanocrystal's surface. In the disordered phase formed $Ti_3O_7^{2-}$ single sheets may start to grow in two- or

three-dimensional. In the case of two-dimensional growth the nanosheets simultaneously roll up into nanotubes, while in the case of three-dimensional growth the rolling of as-grown thick plates is not complete leading only in partial bending of edges. The increasing surface tension of growing nanosheets caused by the charge of the surface of sheets is a driving force the curling of nanosheets. Exfoliated single trititanate sheets curve forming nanotubes. [20, 44] By applying sonication pre-treatment step prior to the deagglomeration of the TiO_2 starting material the length of nanotubes can be controlled. Due to the narrow interparticle space of the agglomerated titania particles the diffusion rate of OH^- and Na^+ ions is uneven across the entire titania surface leading in the non-uniform peeling of swollen surface layers. Therefore smaller nanosheets and consequently shorter nanotubes are formed as shown. Schematic model of formation mechanism of nanotubes with controlled length is shown in Figure 5. [43]

According to the first-principle calculations and experimental thermodynamic data, even in alkaline environment the ion-exchange of Na^+ ions by H^+ ions occurs. The concentration and spatial distribution of these ionic substitutions are crucial for the exfoliation process of Ti_3O_7 sheets from the layered titanates and folding of as-exfoliated nanosheets into nanotubes. The bonding strength between the Ti_3O_7 sheets is decreased by the increasing degree of substitution of Na^+ by H^+ ions affecting the exfoliation process of Ti_3O_7 layers prior to the nanotube formation. [42] *Ab initio* calculations based on the density functional theory (DFT) performed for $H_2Ti_3O_7$ structures were employed for the evaluation of the effects of chemical environment on the two surfaces of the Ti_3O_7 sheets inducing cleavage and rolling of the sheets. [22, 23]

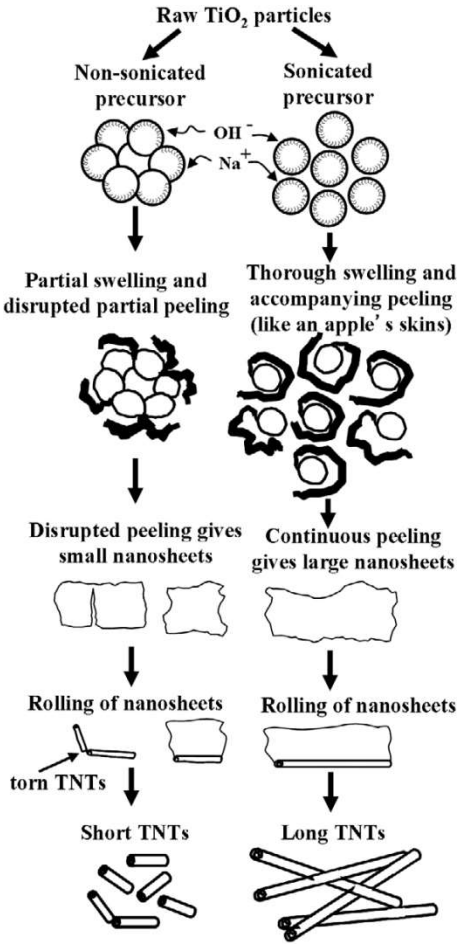

Figure 5: Scheme of the formation mechanism of the short and the long titanate nanotubes.

Since the $Na_2Ti_3O_7$ and $H_2Ti_3O_7$ are two closely related structures and $H_2Ti_3O_7$ may be obtained by the ion exchange reaction of interlayer Na^+ ions with H^+ by immersing $Na_2Ti_3O_7$ powder in HCl aqueous solution the formation mechanism of $H_2Ti_3O_7$-based nanotubes is applicable to the formation of $Na_2Ti_3O_7$-based nanotubes. However, although the frameworks of both titanates consist of $[TiO_6]$ octahedrons, which share edges and corners, the positions of Na^+ and H^+ are very different for the two titanates. The bond lengths are 1 Å for the H-O bond and well above 2 Å for the Na-O bond. The H^+ ions are considered as adsorbed on the surface of the Ti-O skeleton while Na^+ ions are between the Ti-O layers. There are seven distinct oxygen sites for hydrogen adsorption in the structure of octahedrons. Oxygen on these sites is bonded to one, two, three or four Ti atoms. In a stoichiometric $H_2Ti_3O_7$ crystal two hydrogen atoms are bonded to these seven oxygen atoms. Short O-H bond with oxygen located on different sites results in different total energies, which means that the capability of different oxygen sites for adsorbing hydrogen ion is different and results in different O-H bonding strength. Adsorption of hydrogen also causes transfer of certain amount of electrons from Ti-O bond to O-H bond and consequently Ti-O bond length increases.

For the surface layer of the $H_2Ti_3O_7$ in the solution of NaOH the chemical environment on both sides is different, because the concentration of OH^- and Na^+ ions in solution is much higher than in the interlayer region i.e. on the side where the surface layer is bounded to the layers beneath. The H^+ ions at the top of surface in contact with region of higher concentration of OH^- ions (solution) experience more frequent collisions by OH^- ions from solution in comparison to the other side of the layer which is bounded to the layers beneath the surface layer. In addition, the gain energy for the OH^- ion to carry away the surface H^+ ion is very large therefore the formation of water molecule is very likely. The negative charge of the surface layer, which is due to the loss of H^+ ions, is neutralized by Na^+ ions located near the surface. Nevertheless the surface is negatively charged, because Na^+ ions are only weakly bonded to the surface. As the hydrogen ions are neutralized by the OH^- ions a higher negative charge is accumulated on the surface. By the loss of H^+ ions from the surface and simultaneous accumulation of Na^+ ions close to the surface, an electric field is formed, with its strength proportional to the negative charge accumulated on the surface. On the other hand the limiting process preventing the decrease of the repulsive field strength is associated with the reduction of the Na^+ ions. The equilibrium between these two processes results in a negatively charged surface layer. Asymmetry of hydrogen content on the two sides of the surface layer may be described by an average number of H^+ loss per molecule (δ). When δ equals 1, it is assumed that all H^+ adsorbed on the surface side have been removed from the surface by OH^- ions and it corresponds to HTi_3O_7 layer. Hydrogen deficiency on the surface may induce the contraction of relevant Ti-O bonds on the surface and subsequent increase of the surface tension that provides sufficient driving force for the top most layer to be freed from the layers beneath and roll prior to the formation of $H_2Ti_3O_7$ nanotube.

The *ab initio* calculations of the surface tension, elastic strain energy, coupling energy between layers, and Coulomb force indicated that the driving force for the formation of the single-shell nanotubes arises from the asymmetric chemical environment induced by the deficiency of hydrogen ions (δ) at the surface of a single layer. [22, 23] Released hydrogen causes contraction in corresponding Ti-O bond on the top of the surface and the content of hydrogen on both sides becomes unequal. Hydrogen deficiency on one side of the surface layer introduces surface tension. Surface tension increases with increasing hydrogen deficiency resulting in enhanced tendency for the surface layer to bend. When hydrogen is removed from the surface the content of hydrogen on two sides of surface layer becomes unequal and the corresponding Ti-O bond on the top of surface will

contract. Thus the surface tension will increase. As the surface tension overcomes the coupling energy between the surface layer and the layers beneath, it starts to act as a driving force for peeling off of the surface layer from the crystal plate, most likely starting at the edge, and roll up into the nanotube. The surface tension due to the contraction of Ti-O bonds in certain plane may be decreased by the rolling of the trititanate layer along this direction with chiral angle $\theta = 0$. An example of contraction of Ti-O bonds located in (010) plane decreasing the tension by rolling the trititanate layer along [010] direction is shown in Figure 6.

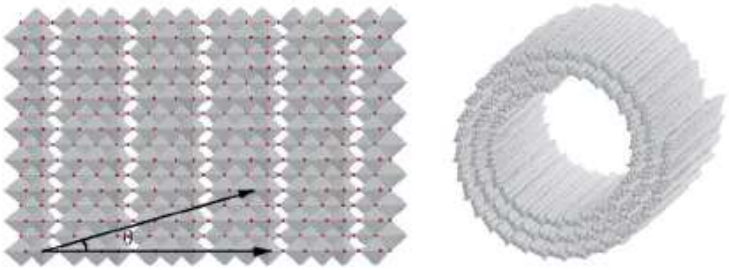

Figure 6: Model of the structure of the single titanate sheet and a nanotube formed by rolling of the sheet along the [010] direction with a chiral vector along the [001] direction and a chiral angle $\theta = 0$.

The surface tension energy favours bending of the layer. After releasing the hydrogen from an oxygen site the corresponding Ti-O bond will contract resulting in a surface tension which tends to bend the layer in order to minimize the tension. The surface energy may be written to a first order approximation using a Hook's law as

$$E_t = \frac{1}{2}\delta k(1 - \delta l_0)^2 \qquad (2)$$

- E_t the surface-tension energy,
- δ the hydrogen deficiency on the surface,
- l the difference in the arc length of the two sides of the layer,
- δl_0 the equilibrium value of l and
- δk the effective spring constant.

It is assumed that the effective spring constant δk is proportional to the hydrogen deficiency δ when the hydrogen vacancies on the surface do not interact strongly. When δ equals zero the equilibrium value of l reduces to zero and for a finite value of δ the surface tension reduces to zero when $\delta l_0 = l$.

The correlation between the arc length and the radius of the curvature of the layer is given by

$$l = \frac{c}{R} \qquad (3)$$

and

$$R_0 = \frac{c}{l_0}, \tag{4}$$

where c is a proportional constant. Then the surface-tension energy resulting from the relevant Ti-O bonds contraction after hydrogen desorption from the surface may be written in following form

$$E_t = \frac{1}{2}\delta k c^2 (\frac{1}{R} - \frac{\delta}{R_0})^2 \equiv \delta b (\frac{1}{R} - \frac{\delta}{R_0})^2, \tag{5}$$

where $b = \frac{1}{2}kc^2$.

The strain energy is independent of the hydrogen deficiency at the surface of the layer and results from the deformation of all angles and bond lengths when the layer is bent. The strain energy works against bending of the layer and as such contributes to the total energy. By use of continuum elastic model the strain energy of a bent $H_2Ti_3O_7$ fragment may be written as follows

$$E_s = \frac{a}{R^2}, \tag{6}$$

where R is the radius of curvature of the bent fragment and a is a proportional constant.

The total energy of the crystal layer is given by equation (7), where E_0 is the total energy per molecule for a perfectly flat layer with $\delta = 0$ and shows dependence of the total energy of a curved crystal layer on R

$$E_{layer} = E_s + E_t + E_0 = \frac{a}{R^2} + b\delta (\frac{1}{R} - \frac{\delta}{R_0})^2 + E_0. \tag{7}$$

The increase of the energy of a perfectly flat surface layer caused by the removal of the H^+ ions from the surface by the OH^- ions initiated the surface layer to start to break away from the layers beneath, since the coupling between them can no longer offset the energy increase due to the hydrogen deficiency on the surface. Although, the $H_2Ti_3O_7$ crystal plate is composed from the identical layers of atoms and the peeling may start anywhere in the crystal plate in general the coupling energy is not a constant and peeling would start at any place with minimum coupling energy.

Based on LDOS calculations only desorption of the hydrogen from oxygen bonded to two Ti atoms significantly contributes to the net charge of the surface layer and represents the principle driving force for formation of nanotubes. From the dependence of the total energy on radius of curvature the clear minimum was observed at ~ 4 nm. Therefore it was assumed that there exists a natural radius of formed nanotubes that minimizes the total energy of the layer. This minimum results not only from the surface tension energy but also from the strain energy.

Since the capability of different oxygen sites to adsorb hydrogen is not equal, different hydrogen atoms on different oxygen sites may have a different effect on the surface tension. Each oxygen site can adsorb two hydrogen atoms. The minimum energy

configuration corresponds to two hydrogen atoms being adsorbed at two different oxygen sites. The first site represents the oxygen, which is bonded to one Ti atom and the second site is the oxygen bonded to two Ti atoms. These two sites have the lowest energy for hydrogen adsorption forming the strongest O-H bond. Microscopically the surface tension energy and the optimal radius of curvature are determined mainly by the hydrogen atoms bonded to the oxygen bonded to two Ti atoms, whereas the hydrogen absorption at other oxygen sites rarely occurs due to the higher energy. By comparing the calculated and fitted energies for different radii of curved layers with the same hydrogen deficiency the energy minimum was again observed at optimum radius of curvature at ~ 4 nm. The optimized radius $\overline{R} = 4.3$ nm for a peeled off layer may be then obtained from equations 8 and 9.

$$\frac{\partial E_{layer}}{\partial R} = 0 \tag{8}$$

$$\overline{R} = \frac{(a+b\delta)R_0}{b\delta^2} \tag{9}$$

So far it was assumed that rolling of nanosheets into nanotubes occurs along the [010] direction with zero chiral angle (as shown in Figure 6). Since the surface tension is related to the contraction of the Ti-O bond due to the removal of H^+ from the surface and the rise of the surface tension is most effectively released by rolling the (010) titanate layer in [010] direction with the chiral angle $\Theta = 0$ the dependence of the surface tension on chiral angle comes into the equation for the total energy of the layer that can then be written as

$$E_{layer}(R,\Theta) = E_s + E_t + E_0 = \frac{a}{R^2} + b\delta\left(\frac{cos\Theta}{R} - \frac{\delta}{R_0}\right)^2 + E_0. \tag{10}$$

From the equation (10) it can be readily seen that the minimum energy corresponds to the zero chiral angle, which is in agreement with the experimental data showing the formation of nanotubes with the tube axis pointing along the [010] direction. The energies contributing to the curvature of a single trititanate sheet determined by first principle calculation are graphically presented in Figure 7.

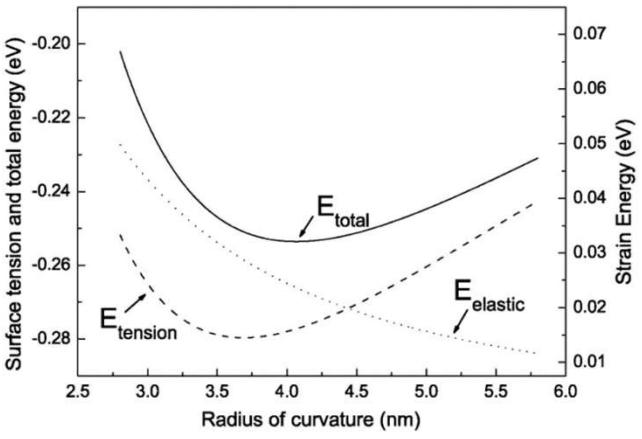

Figure 7: First principle calculations of energies contributing to the nanotube radius formed by rolling of a trititanate single sheet.

When nanotubes with more than one shell are formed additional factors, i.e. the coupling energy, the number of shells and Coulomb energy need to be considered. In the case of multi-shell nanotubes the coupling energy E_{coupl} between the shells results in lowering of the total energy and the radius of the nanotubes will deviate from the optimal curvature with increasing number of shells. The deviation of the radius from the optimal radius will increase the total energy of the crystal layer. On the other hand the repulsive Coulomb energy E_C evidently increases as the hydrogen deficient negatively charged crystal layers roll prior to the tube formation. The energy rise from the increase of the shell number is not sufficient to stop the rolling process since its contribution is much smaller as compared to that originating from the coupling between shells. However, the repulsive Coulomb energy, which rapidly increases the total energy of the rolled layer, may prevail over the coupling energy and therefore terminate the rolling process and limits the upper tube diameter. When the total energy becomes positive the peeling/rolling process will be terminated leading in the formation of four-shell nanotubes which is in good agreement with experimentally observed nanotubes. The contribution of different forms of energies contributing to the total energy of the rolling crystal layer related to the number of shells is shown in Figure 8.

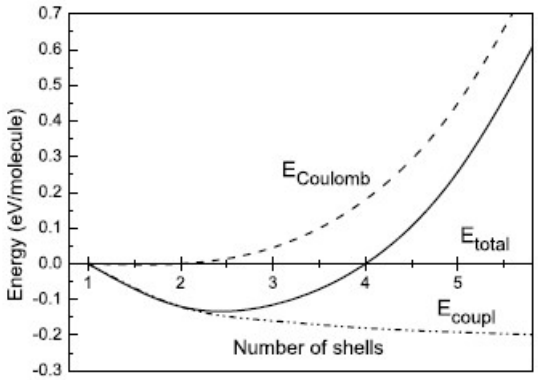

Figure 8: Contribution of the coupling and Coulomb energy to the total energy of the rolling crystal layer as a function of the number of shells in a formed multi-shell nanotube.

Van der Waals forces play central role in all phenomena involving intermolecular forces. Although they are not as strong as Coulomb interactions, they are always present and they are of long range. The van der Waals interaction free energy between two surfaces calculated using Hamaker summation method is as follows form equation (11). The van der Waals force between two geometrically identical bodies in the medium is always attractive. [45]

$$W = -\frac{A}{12\pi D^2} \tag{11}$$

A Hamaker constant,
D distance between two surfaces.

The coupling energy of a nanotube E^t_{coupl} results from van der Waals force between layers in $H_2Ti_3O_7$ bonding these layers together. The average number of shells may be

estimated as

$$N \sim \frac{L}{2\pi R_0}, \tag{12}$$

where L is the circumference of the nanotube, R_0 is the optimal radius of the nanotube exhibiting zero surface tension. The approximate average coupling energy of the nanotube per molecule is given as

$$E_{coupl}^{t} \sim \frac{N-1}{N} E_{coupl} \ , \tag{13}$$

where Ecoupl expresses the coupling energy between layers per molecule. In a nanotube the electrostatic force among positive charge coming from Na^+ ions and negatively charged Ti_3O_7 layers will enhance the coupling energy between shells giving the modified form of the tube coupling energy

$$E_{coupl}^{t} \sim \left[x k_{coupl}(d) + E_{coupl} \right] \frac{N-1}{N} \ . \tag{14}$$

A coupling constant k_{coupl} is related to the shell spacing d. The d spacing of 0.78 nm, which is characteristic for such nanotubes, was determined by the TEM analysis. Since the coupling energy is not sensitive to the hydrogen deficiency the main contribution due to the residual charge on the surface layer is included into equation for the total energy of a nanotube by the Coulomb repulsive energy.

The Coulomb interaction is very strong and of long range. The free energy for the Coulomb interaction between two charges, r apart, is given by:

$$w(r) = \frac{z_1 z_2 e^2}{4\pi\varepsilon_0 \varepsilon r} . \tag{15}$$

The Coulomb force is the strongest among the physical forces and it is stronger than most chemical binding forces. For like charges the force is repulsive, while for unlike charges the force is attractive. The dependence of the Coulomb force on the inverse-square distance range (equation 16) shows that Coulomb force is very long ranged. At the large distances the decay of the electric field is always exponential with the distance, therefore the Coulomb interactions between ionic crystals, charged surfaces and dissolved ions is of shorter range, but still of much longer range than covalent forces. [45]

$$F = -\frac{dw(r)}{dr} = \frac{z_1 z_2 e^2}{4\pi\varepsilon_0 \varepsilon r^2} \tag{16}$$

In the nanotube formation process the Coulomb energy results from the hydrogen deficient negatively charged $H_2Ti_3O_7$ layer that rolls into the nanotube. The negative charge may be partially compensated by electron exchange with surrounding Na^+ ions. A residual charge on the surface layer results from the balance between charging and discharging of the surface. The slowest process which determines the balance is the electron exchange between Na^+ ions and negatively charged surface layer. When such

negatively charged layer starts to roll into a nanotube, the tube is negatively charged and the repulsive Coulomb force starts to play an important role in the nanotube formation process. The Coulomb energy E_C increases rapidly with increasing number of shells N and it is proportional to the average radius of the nanotube and the spacing between shells. When the averaged radius of nanotube r_0 is much larger than the shell spacing d the Coulomb energy can be written as

$$E_C(N) = E_C(N-1) + (N-2)^2 E_C(3) \tag{17}$$

where $E_C(1)$ and $E_C(2)$ equal 0, $E_C(3) = k_C \rho^2 r_0^2 \ln(\frac{r_0+d}{r_0-d})$, and ρ is the average number of Na^+ ions per molecule located outside the outermost shell and inside the innermost shell. For the nanotubes with two or three shells the coupling energy prevails over the Coulomb energy enabling the rolling process to proceed. When the shell number increases the Coulomb energy increases rapidly and at about four shells the total energy of the multishell nanotube becomes positive and thus terminates the rolling process (shown in Figure 8). The formation of mostly four-shell nanotubes was also confirmed experimentally. [23]

1.1.1.2.2 Formation mechanism of nanotubes: bending of multi-layered nanosheets prior to the nanotube formation

In contrast to the nanotubes formation mechanism based on peeling and rolling of single-layered sheets, which does not support formation of the nanotubes via scrolling of multi-layered nanosheets [20, 22, 29] Bavykin et al. [1, 46] suggest a rolling of multi-layered nanosheets into nanotubes.

During the dissolution/crystallization process under hydrothermal conditions the growth of multilayered nanosheets proceeds at the edges of the individual layers rather than forming a new layer giving rise to the mechanical tension of the nanosheets. It is assumed that during growth process width of individual layers varies. The imbalance in the width therefore causes certain layers to move within the multi-layered nanosheet. During the shift of the layers and bending of the nanosheet the gain in the surface energy is sufficient to compensate the increase of the mechanical tension arising due to the curving of the nanosheets prior to the nanotube formation and it can be written as

$$\frac{k(\Delta y)^2}{2} < \sigma L \Delta x \ . \tag{18}$$

The left side of the equation (18) describes the mechanical energy of the bent nanosheet, where Δy is the curving of the deformed layer and k is the spring constant while the right side corresponds to the excess of the surface area due to the imbalanced layer in the nanosheet. σ is the excess surface energy per unit area at the solution–particle interface, L is the length of imbalanced layer and Δx is the imbalance in layers width. The driving forces responsible for curving of multi-layered nanosheets due to the imbalanced layer widths are schematically shown in Figure 9.

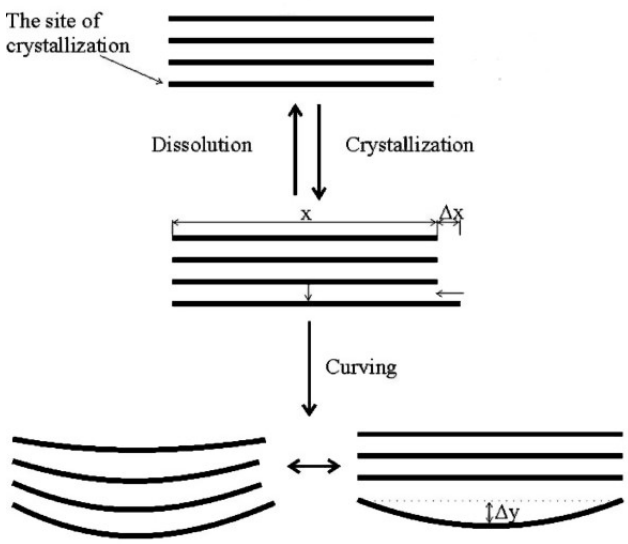

Figure 9: Scheme of the nanotube formation mechanism via bending and rolling of multi-layered nanosheet under hydrothermal conditions.

According to this formation mechanism after bending of multi-layered sheet different types of nanotubes are obtained depending on the sealing of the layers nanotubes (shown in Figure 10). When matching layers close up perfectly the nanotube cross-section is composed of concentric rings. For the sealing of the non-matching layers typically the scrolls or snail-type nanotubes are formed. However, in some cases the bending is not complete leading in the formation of the onion-type nanotubes with visible seam running along length of the nanotube.

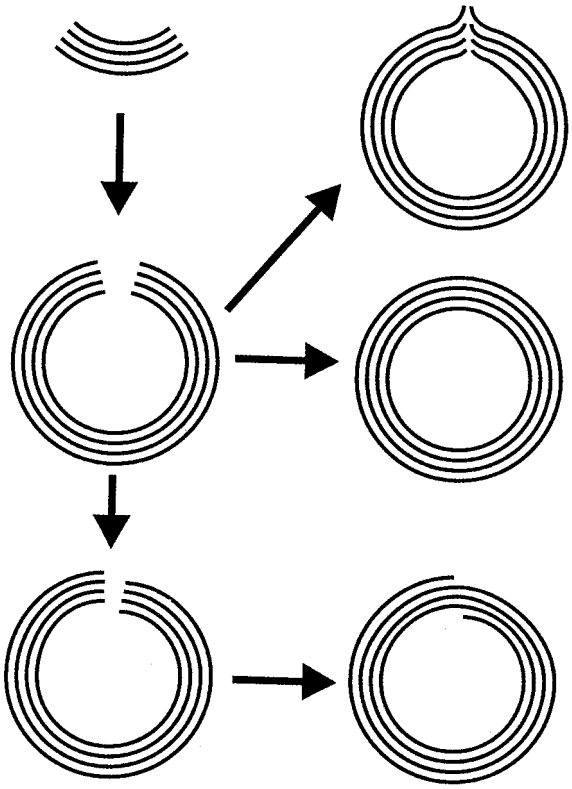

Figure 10: Types of nanotubes formed by different closing up mechanisms of layers building certain nanosheet.

1.1.1.2.3 Formation mechanism of nanobelts

Hydrothermal synthesis enables formation of titanate nanobelts by adjusting the temperature and duration of hydrothermal reaction. The transformation of nanosheets into the nanobelts requires higher temperatures of hydrothermal reaction as compared to the temperatures needed for the nanotubes synthesis. The sequence of events leading to the formation of titanate nanobelts under hydrothermal conditions is similar to the formation steps in the formation process of the nanotubes except for the absence of the rolling step. The rectangular morphology of the nanobelts originates from the intrinsic structural anisotropy and growth rate of the principal directions. The growth rate of the principal directions follows the order $r_{001} > r_{100} > r_{010}$. [35, 36] The preferable growth of nanobelts in the [001] crystallographic direction suggests maximized dissolution/crystallization rate along c axis causing the nanosheet to become too rigid to roll up into nanotube at higher temperatures of hydrothermal reaction leading in the formation of nanobelts elongated in [001] direction. [1]

Recently, another formation mechanism of the nanobelts via self-assembled bundles of nanotubes serving as an intermediate phase was suggested. By employing the rotating autoclave the unique flow was generated in the vessel reducing the surface-to-bulk ratio gaining the free enthalpy through transport of solution-phase material into hollow nanotubes and recrystallization within the nanotube channels. [47] It was assumed that the flow conditions in the revolving autoclave provided favourable environment for the self-assembly on nanotubes bundles by mixing-effect induced oriented attachment and the transformation into nanobelts is thermodynamically controlled regarding to the minimisation of the total free enthalpy of the system. In addition, for the explanation of

the formation of nanobelts through nanotube intermediate phase at temperatures higher than 170°C without introduction of revolving autoclave the combination of Ostwald ripening and oriented attachment mechanism was proposed. [48, 49] The coarsening of material occurred due to the bunching/coalescence of nanotubes by much faster oriented attachment mechanism followed by the filling of the nanotube channels through precipitation of dissolving titania via Ostwald ripening route resulting in the transformation of smaller nanotubes into larger nanobelts.

1.2 Hydrothermal synthesis

Although that today the hydrothermal synthesis is widely used for the preparation of various materials there is no unique definition for it available. Usually, the term "hydrothermal reaction" describes any heterogeneous reaction of materials performed under high pressure and temperature in a closed system in the presence of water, aqueous solvents or mineralizers to dissolve and recrystallize the material. [50] Under hydrothermal conditions reactants which are under ordinary synthesis conditions difficult to dissolve become soluble in a suitable solvent forming complexes and as such enter the reaction. In the hydrothermal reaction the reactants are sealed inside the autoclave usually made of various alloys where the mixture is externally heated in the temperature range from 100°C to 2000°C giving rise to the pressure that is controlled by the degree of filling of the vessel. By the temperature and the degree of filling of the autoclave related pressure established inside the autoclave may be evaluated from the *P/T* diagram of given solvent. As an example in Figure 11 the *P/T* diagram of water is shown. Due to the behaviour and specific properties of the solvents under hydrothermal conditions such are high solvation power, mass transport of solvents and high compressibility different reactions may be obtained [50]:

- Formation of new phases or stabilization of new complexes,
- crystal growth of inorganic compounds,
- preparation of non-agglomerated materials with controllable size and morphology,
- leaching of ores and metal extraction and
- decomposition, corrosion, etching.

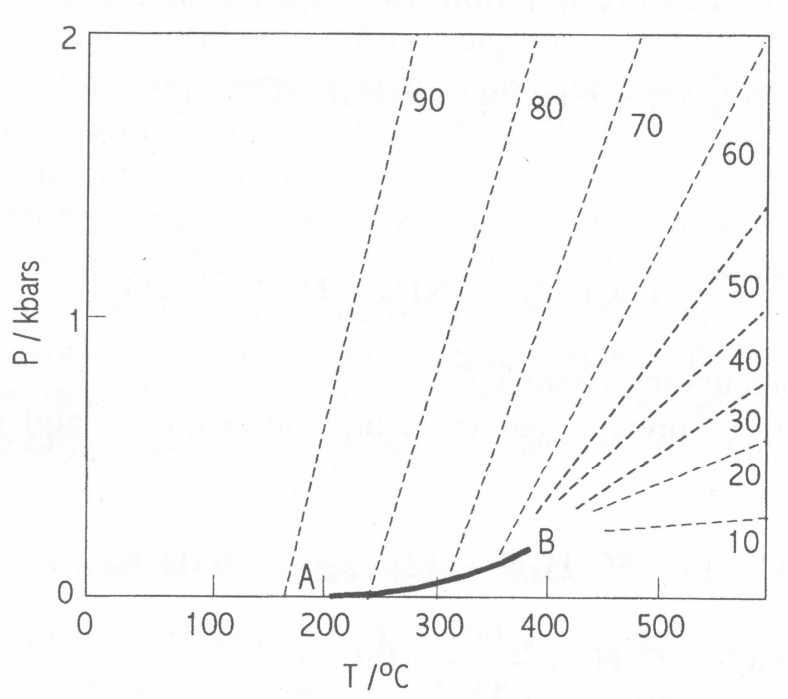

Figure 11: The pressure-temperature relationship of water at a constant volume inside a sealed container where the dashed lines represent the pressure and the numbers denote degree of the filling of the autoclave with water at ambient conditions. AB curve is the saturated steam curve that separates water from steam. At temperatures above 374°C the water is in the supercritical condition where the distinction between liquid and vapour states is no longer possible.

The hydrothermal synthesis can be performed in a wide variety of aqueous and solvent mixtures based system. Mineralizers entering the hydrothermal reaction may be organic or inorganic compounds playing the role of additive for pH adjustment and are usually employed at excessively high concentrations to increase the solubility of the reactants and to promote the reaction. [51] The type and the concentration of a solvent determine the hydrothermal process by influencing the solubility of reactants, quantity and composition of phases and the dissolution/crystallization process of various materials. For the selection of an appropriate mineralizer following properties of a solvent must be considered:

- Congruent dissolution of the reactant,
- a sharp enough change in the solubility under elevated temperatures and pressures,
- a specific quantity of absolute solubility of reactant,
- the formation of readily soluble complexes mobile in the solution and
- medium possessing a specific redox potential assuring the existence of ions of the required valence.

Although that the hydrothermal solution is in general considered as ideal one a significant deviation from the Rault's law due to the specific interaction between the solid components and the solvent in real hydrothermal solution occurs. The solubility of certain reactant in various solvents at constant temperature and pressure differs from solvent to solvent since the enthalpy and entropy of the solubility is different for different solvents as it can be seen from the expression for the change in the Gibbs free energy when reaching the equilibrium conditions shown in equation (19), where K is the equilibrium constant. [50]

$$\Delta G = \Delta H - T\Delta S = RTlnK \quad (19)$$

Since the water is low cost, environmentally benign throughout the nature widespread substance, it is the most important solvent and it is very often introduced into hydrothermal systems as a hydrothermal mineralizer. In the hydrothermal synthesis procedure of various materials by chemical reactions of reactants in water in a sealed container at high pressures above 100 kPa and temperatures above 100°C the water has a function of pressure-transmitting medium and acts as a mineralizer or a catalyst or additionally it can be reactant or product of the reaction. [50, 52, 53] The properties of water at elevated temperature and pressure are remarkably different from those at standard conditions influencing the reaction rates of chemical reactions. Water under extreme conditions exhibits macroscopic properties as a non-polar solvent, although that the single molecules preserve polar character, and therefore provides a unique reaction medium with unusual properties suitable for performance of various chemical reactions for the synthesis of wide range of materials with controllable physical and chemical properties, morphology, particle size, etc. [53, 54] The temperature and pressure dependent solubility of dissolving species is decreased for polar and ionic compounds and is increased for those having nonpolar character. The increase or decrease in solubility of the compounds in water under elevated temperature and pressure is consequence of the drop of the water polarity.

The change of the ionic hydration is strongly related to the decrease of the dielectric constant and density of water with increased temperature and/or pressure. The reaction rates of the chemical reactions under high temperatures and pressures can be controlled by variation of the relative dielectric constant of water and by the water ionic product. The relative dielectric constant and ionic product increase with the increasing pressure. The water under high pressure can exhibit the ionic product of some orders of magnitude higher as compared to the ionic product of water at ambient conditions. Due to the high concentrations of H_3O^+ and OH^- ions water at elevated pressures may act as an acid or base catalyst. However, since the detailed mechanism of a reaction occurring in the hydrothermal procedure in water is not described yet it is nearly impossible to predict to which extent does the change in the relative dielectric constant and the ionic product of water influence the hydrothermal reaction with a polar activated complex. [53]

Although the hydrothermal technique is suitable for preparation of non-oxide materials such as pure elements, selenides, tellurides, nitrides, carbon nanostructures and oxides it has been mainly introduced for synthesis of oxide materials, both simple oxides (ZrO_2, TiO_2, ZnO, etc.) as well as complex oxides (perovskites, ferrites, etc.), which are materials widely used for preparation of advanced electronic ceramic, particularly for dielectrics. The classical production procedure of electronic ceramic based on solid state reactions usually includes high temperature, long lasting treatment and additional milling, while in general liquids under hydrothermal conditions provides an effective medium for acceleration of diffusion, adsorption, nucleation, crystallization and growth rate. By employing hydrothermal conditions the reaction temperatures are drastically decreased while the milling step is eliminated from the fabrication procedure of advanced materials for electronic components resulting in a reduced production costs. The complex reactions enhanced by the mineralizer under elevated temperatures and pressures in a closed system enable formation of fine anhydrous crystalline powders of highest degree of purity and very low level of aggregation with controlled particle size, morphology, microstructure and stoichiometry. Variety of morphologies and forms of the ceramic materials prepared by the hydrothermal synthetic route such are powders, elongated structures (fibers), cubes, spheres, coatings on various substrates, single crystals, etc. is controlled by the

precipitation process of crystalline powders directly from the solution that regulates the nucleation rate, growth and aging of as-synthesized materials. [55] The decreased temperature ensures precise stoichiometry since there is no loss of components due to the volatilisation at high temperatures and enables formation of cracks-free ceramic since the stress-induced defects caused by phase transformation during cooling process are minimized. Since the microstructural features such as grain size influencing the electric properties of the produced material the microstructure is a crucial parameter in the manufacturing process of electronic multilayer components. [56] For this reason the optimisation of sintering temperature plays important role in tailoring of the properties of fabricated products. The hydrothermally prepared ceramic materials require moderate sintering conditions as compared to the conventionally synthesized powders since they are prone to high reactivity toward effective sintering.

In the field of synthetic routes towards fabrication of free standing nanostructured materials the hydrothermal method is of considerable interest for practical applications since it is cost effective, energy saving, simple, environmentally friendly technique that enables higher solubility and reaction rates as well a better control over the nucleation, shape and morphology of nanostructures in comparison to the other conventional synthesis processes and provides an effective route towards formation of nanomaterials of high purity obtained even from impure starting materials. In a substrate assisted hydrothermal process the hydrothermal reaction can be performed on large areas and/or flexible substrates in which the low reaction temperature enables utilization of temperature sensitive substrates such as plastics or textiles, and provides the ability to fabricate aligned nanorods on pre-treated substrates that control the nucleation of nanostructures.

Titanate-based 1D nanostructures are mainly obtained by the template method, anodization and wet chemical methods. However, the first two methods are not able to yield very low dimensional, well separated nanotubes without thermal post treatment [46, 57], while the hydrothermal method has proved as a suitable method for production of nanotubes with a small diameter. [9, 46, 57] By adjustment of pH value, reagent and mineralizer concentration, degree of autoclave filling, temperature and pressure of the hydrothermal reaction the control over morphology, size, chemical composition and crystal structure of the products is obtained. [50, 58, 59] Utilization of an alkaline environment and hydrothermal conditions provides an effective reaction environment and has proved as a simple, effective and non-expensive synthetic route for the synthesis of various one-dimensionally nanostructured materials. [59, 60, 61] Furthermore, introduction of hydrothermally derived precursors with corresponding morphology and/or chemical and crystal structure into the optimized hydrothermal process enables controllable formation of 1D nanostructures through the topochemical reaction, in which the morphology/shape of a template material is inherited by the products, while the chemical composition is altered, and provides a promising methodology for the template-assisted fabrication of one-dimensional nanostructures of various materials. [61] A typical hydrothermal treatment of TiO_2 in crystalline or amorphous form in highly concentrated NaOH yields titanate-based one-dimensional nanostructures of various morphologies depending on the employed reaction temperature of hydrothermal process. The hydrothermal method offers many advantages over other used methods for the synthesis of alkali metal titanates such are solid state reaction, melt reaction, and flux growth although that hydrothermal reaction rate is slow and it is not suitable for large scale production due to the autoclave volume limitation. By the hydrothermal technique synthesized titanate nanostructures are of high purity, controlled shape and exhibit uniform size distribution. [32]

With the variation of reaction parameters required for the formation of titanate nanostructures under the hydrothermal conditions the tailoring of the morphology of as-formed nanomaterials is obtained. The morphology of these nanostructures affects their thermal, chemical and structural stability, degree of crystallinity and mesoporosity, specific surface area, and physico-chemical properties. [62] Hydrothermal formation process in highly alkaline environment ensured by the addition of NaOH and/or KOH mineralizers applied for the production of single crystalline titanate nanotubes and nanobelts includes several steps which are described by the proposed "TiO_2 precursor-nanosheets-nanotubes-nanowires" transformation mechanism[48]. The partial dissolution of the titanium source in alkaline solution leading in the release of Ti^{4+} species mainly in form of mono- or poly-titanic ions [63], which concentration in solution is temperature dependent [46], into the reaction mixture is followed by the formation of thin single- or multiwalled titanate-based nanosheets acting as an intermediate phase that is in dynamic equilibrium with Ti(IV) species in the solution. Since the nanotubes are formed rapidly once the Ti(IV) species are obtained in the solution the rate of titanate nanotubes formation and the yield of nanotubes is strongly related to the release of Ti^{4+} species from the precursor crystallite's surface into the alkaline solution. [64] The consumption of the precursor and consequently the concentration of Ti^{4+} species in alkaline solution is regulated by the kinetics of the precursor dissolution process. The zero-order kinetics of anatase dissolution indicates that the dissolution process was not depended on the precursor concentration and solubility resulting in a higher yield of formed nanotubes as compared to the yield of nanotubes formed from slower second-order dissolution process of rutile. [64] The hydrothermal formation process including crystallization/dissolution events and growth of nanosheets accompanied by their transformation into nanotubes or nanobelts is finished when the entire initial amount of the titanium source is converted into one-dimensional titanate nanostructures exhibiting one of the two morphologies. Formation of either nanotubes or nanobelts is controlled by the concentration of Ti^{4+} species in the alkaline (NaOH or KOH) solution at elevated temperatures which can be approximated by following expressions [65]:

$$\ln\left(c_{NaOH}^{Ti(IV)}\right) = 0.355 - \frac{2623}{T+273} \tag{20}$$

and

$$\ln\left(c_{KOH}^{Ti(IV)}\right) = -0.359 - \frac{2056}{T+273}. \tag{21}$$

Titanate nanosheets experience both the growth in all crystallographic directions as well the scrolling into nanotubes depending on the kinetics of both transformation processes. The morphology of titanate 1D nanostructures formed by the transformation of titanate nanosheets is controlled by the variation of synthesis conditions that ensure appropriate Ti^{4+} concentration which would favour the formation of either nanotubes or nanobelts. The favourable formation of nanobelts may be consequence of an increase in the local Ti^{4+} concentration, which may accelerate the rate of nanosheet growth and hinder the rate of nanosheets rolling process. [65] Rapid nanosheet growth results in the increment of nanosheet thickness that make the sheet too rigid to bent and render its rolling prior to the nanotube formation impossible.

Since the implementation of hydrothermal method for the synthesis of titanate- and

titania-based nanostructures many efforts have been made toward understanding of the reaction kinetics and thermodynamics of hydrothermal processes. The lack of the insight into the hydrothermal reaction is hindered by the use of autoclaves. To optimize the synthesis conditions which would provide an effective methodology for the fabrication of titanate-based nanostructures with the controlled morphology and chemical composition the understanding of the influence of the type and concentration of mineralizer in the reaction solution as well as initial raw materials on the properties of final products, impact of the temperature, pressure and/or degree of autoclave's filling on the nanostructure's morphology is needed. By this knowledge the tailoring of nanostructures physicochemical properties may be possible.

1.3 Nanostructured composites

Development of multifunctional materials that exhibit improved properties of individual components, the so called composites or hybrid materials, is an extremely active research field. The synthesis and characterisation of semiconductor-based hybrid materials is essential for efficient performance of various devices. In scope of these investigations, semiconductors normally prone to an extremely high degree of recombination of photo-generated charge carriers resulting in a low photo-efficiency could be manipulated. Nanosized semiconductor/semiconductor and metal/semiconductor interfaces can be made to avoid low bulk photo-efficiency and they can facilitate a charge harvesting in these hybrid systems. [66]

1.3.1 Semiconductor-based nanocomposites

The complementary and size dependent optical properties of metal and semiconductor nanostructures of various morphologies make them very attractive as potential candidates for environment friendly applications related to the photo-induced phenomena occurring in these combined nano-scale materials. Within the field of catalysis, photo-catalysis, electrochemistry and sensing semiconductor-based hybrid materials have been increasingly studied prior to the controlled designing of composites with improved and tuneable catalytic and sensing properties arising from the interactions of their phases/counterparts at the interfaces.

By the transition of inorganic materials from bulk towards nano-scale region several changes in their optical and electronic properties that are uniquely controlled by the size and shape of nanocrystals occur. As particle dimensions are reduced to certain size limit quantum confinement behaviour of nanoparticles become distinctive. For semiconductors in nano-regime the nanostructures exhibit properties between those of molecules and bulk materials. In the nanometer length scale the wave functions of electrons and holes in the conduction and valence band are confined by the nanometric dimensions leading in a development of discrete energy levels. As a result of quantum confinement of charge carriers these quantized nanoparticles exhibit modified optical and electrical responses. In comparison to the semiconductor nanostructures the quantum size effect and essential change in the energy spectrum due to the quantum confinement occurs in metal nanoparticles at smaller sizes. As a metal nanoparticle size is reduced down to few hundred atoms the density of state is decreased to an extent that the continuous energy structure is replaced by quantized levels. By decreasing the size of metallic nanoparticles, a high percentage of particle atoms is on the surface leading in an increased dominance of

the surface atoms over the atoms in the interior of the particle making the electronic properties of the material much more sensitive to the surface changes. Consequently, in metallic nano-sized structures an enhancement of surface phenomena is obtained, in particular surface plasmon resonance (SPR), whereas the SP frequency is controlled by the shape and size of a nanoparticle.

1.3.1.1 Localized surface plasmon resonance (LSPR)

The interaction of nano-sized metallic structures with light is characterized by the coherent surface charge density oscillations of the free electrons within the conduction band induced by the incoming electromagnetic field leading in an in-phase oscillation that is in resonance with the incident light frequency.

In a metallic particle with dimensions (diameter) much smaller than the wavelength of incoming light ($d<<\lambda$) the oscillating electric field of the irradiation that is essentially uniform across entire particle induces the displacement of weakly bounded electrons within conduction band and give rise to the polarization of negative charges at the surface of nanoparticles relative to the positive nuclei. [67, 68] As the electron cloud is displaced upon irradiation relative to the positive lattice the surface polarization is the main restoring force resulting in the formation of dipolar oscillation within the entire nanoparticle between the negatively charged electron cloud and positively charged nuclei network as shown in Figure 12. As a result of the collective oscillations of nanoparticles' conduction electrons a surface phenomenon i.e. the localized surface plasmon resonance (LSPR) is obtained. The surface denotes the polarization of surface charges resulting from the collective electron oscillations that are confined and enhanced on the surface of nanoparticle and the plasmon is in analogy to the collective oscillations within gaseous plasma. The excitation of surface plasmons is a resonant process with the dipole plasmon frequency that is primarily controlled through the electron density of the material. However, the oscillation resonant frequency is tunable by several parameters such are the shape and size of the charge distribution, the effective electron mass, the composition, size, and shape of the metallic nanoparticle, and its dielectric environment. [68, 69] When the exciting light frequency correspond to the intrinsic electron oscillating frequency the interference of the collective oscillation of the electron cloud relative to the nuclear network with the incident photon frequency will cause the light of specific wavelengths to be absorbed resulting in generation of strong surface plasmon absorption bands. [70] Since each excited metal nanoparticle smaller than the wavelength of the exciting light acts as an electric dipole the excitation of localized surface plasmons causes selective photon absorption and generation of locally enhanced electromagnetic near-fields that are localized within a few nanometers of a surface of the metallic nanocrystal.

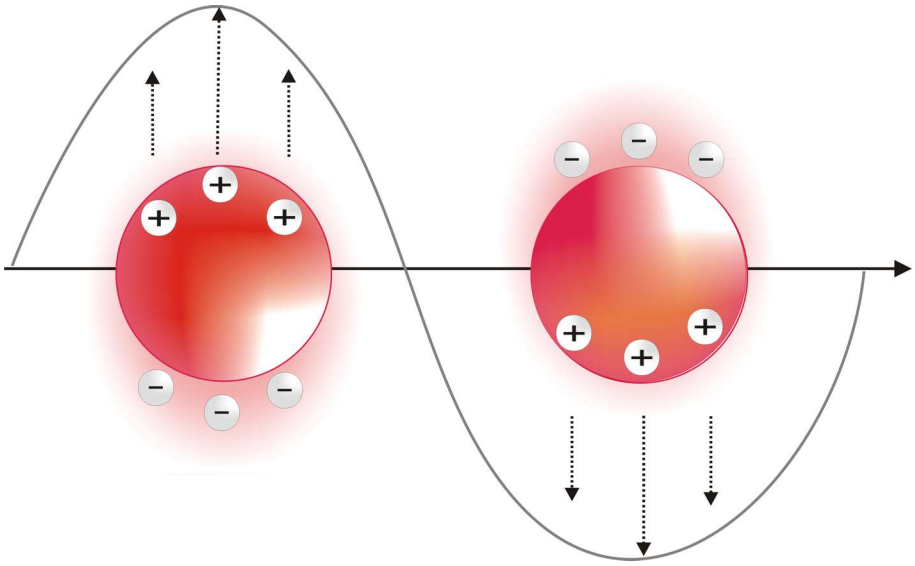

Figure 12: The displacement of the conduction electrons relative to the positive nuclei resulting in the excitation of dipolar surface plasmons in a spherical metal nanoparticle induced by the electromagnetic irradiation with a wavelength of a visible light.

In order to tune the optical and electronic properties of nanostructured metals of various shapes and sizes the fundamental relationship between surface plasmons and light as well the applications associated to the SPR drive great interest in this field. Therefore spectral features of surface plasmons of metal particles have been extensively studied and applied to the Maxwell's equations. The intensities and frequencies of SPR bands strongly depend on the size and shape of particles, and reflect the local surrounding dielectric properties. As result of particle interaction with electromagnetic oscillation the strong optical extinctions in conductive metal particles arise. By introduction of appropriate boundary conditions, Mie [71] was first who solved the Maxwell's equations for interaction of an electromagnetic wave with small spherical particles that leads to a series of multipole oscillations for the extinction cross section of the nanoparticles. The total extinctions cross section composed of absorption and scattering is given as sum of all electric and magnetic multipolar plasmon oscillations. [72]

In the extrinsic regime i.e. for particle size comparable to the wavelength of the exciting radiation the solution of Maxwell equation for the electrodynamic calculations leads to the non-uniform electric field distribution along the particle, inhomogeneous and incoherent electron cloud polarization in each point of the particle and results in the excitation of higher-order multipolar plasmon oscillations. For the particles larger than 20 nm the extinction cross section is dependent on these oscillations and the extinction spectrum is dominated by the higher-order multipole absorption and scattering. [72] For the extrinsic size effects, these higher oscillation modes depend on the particle size solely and its peak is shifted toward lower energies resulting in the plasmon band red shift and increased bandwidth as the particle size is increased as shown in Figure 13. [72]

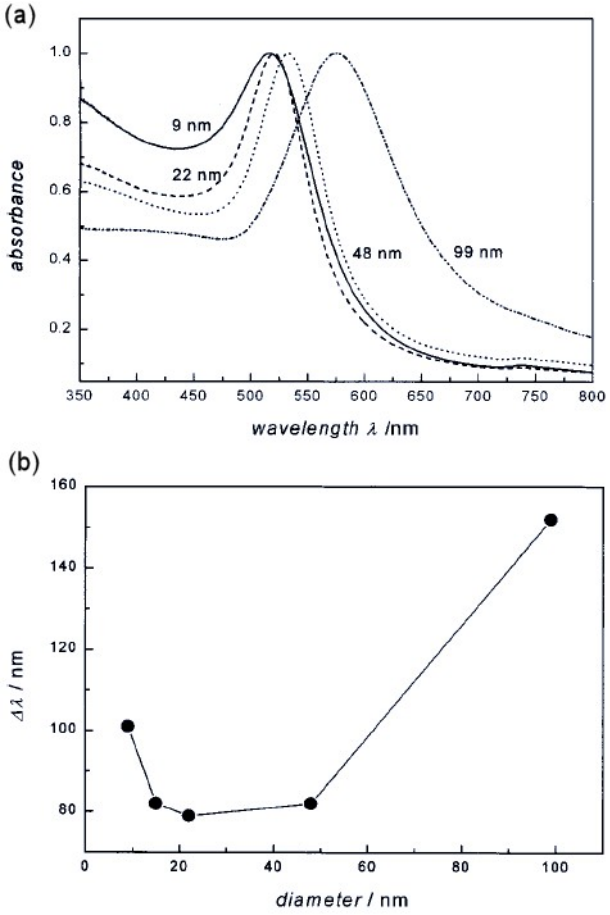

Figure 13: Dependence of the SPR on particle size in the extrinsic region. (a) UV-vis absorption spectra of four different size gold nanoparticles in region from 9 to 99 nm showing red-shift of plasmon absorption maximum, (b) the plasmon bandwidth as a function of nanoparticles diameter.

For nanoparticles small compared to the wavelength of the incident light the absorption is within a narrow wavelength range. As the nanoparticle's size approaches to the mean free path of the conduction electrons the intrinsic size effect in the optical spectrum features of these nanoparticles occurs. [73] The particles experience a resonantly enhanced constant electric field within interior of the particle (the quasi-static limit), which, in the small particle limit, is homogenous throughout the particle's volume. The optical absorption spectrum for particles of size much smaller than the wavelength of irradiation in the surrounding medium has been obtained by solving the Maxwell's equations for scattering electromagnetic waves by spherical particles as it was conducted by Mie. Since in the intrinsic size region only the dipole oscillations contributes to the extinction cross-section, the analytical solution of Maxwell equation is simplified by introduction of quasi-static approximation, which is suitable for nanoparticles in this size regime. Assuming that nanoparticles behave as a material with frequency-dependent dielectric constant same as bulk metal Mie's solution yields the particle extinction cross-section, σ_{ext}, as written in equation 22. [73, 74]

$$\sigma_{ext}(\omega) = 9\frac{\omega}{c}\varepsilon_m^{3/2}V\frac{\varepsilon_2(\omega)}{[\varepsilon_1(\omega)+2\varepsilon_m]^2+\varepsilon_2(\omega)^2} \tag{22}$$

where V is the particle volume, ω is the angular frequency of the exciting light, c is the

speed of light, and ε_m and $\varepsilon(\omega)=\varepsilon_1(\omega)+i\varepsilon_2(\omega)$ are the bulk dielectric constant of the surrounding material and the particle, respectively. The dielectric constant of matrix material, ε_m, is assumed to be frequency independent, while the dielectric constant of particle is a function of energy where the real part determines the wavelength position of the resonance and the imaginary part determines the bandwidth. [75] A strong resonance (a band maximum) occurs roughly at the frequency ω where $\varepsilon_1(\omega)= -2\varepsilon_m$, if ε_2 is small or weakly dependent on ω, the surface plasmon resonance frequency, which is for gold, silver and copper at visible frequencies, is determined. [67, 75] Within the dipole approximation the extinction cross-section (coefficient) does not depend on particle's size as it was observed experimentally. This discrepancy is ascribed to the assumption in the Mie's solution that electronic bands and dielectric constant of the particles are equal to those in their bulk form, which is no longer valid as the particle size is decreased. As well the assumption of bulk electronic and optical properties associated with the electronic structure of the nanoparticles is questionable. Furthermore, as the average particle diameter is below 20 nm the size dependence of the dielectric constant is introduced. As the diameter of the particle becomes smaller than the mean free path of the conduction electrons the electron surface scattering becomes significant. The electron mean free path describes the quasi-elastic scattering of conduction electrons. For the silver the electron mean free path is around 50 nm. Since the mean free path of electrons is limited by the physical dimensions of the nanoparticles, the electrons faster reach the surface, scatter and lose their coherence as the size of nanoparticles is reduced. Consequently, the plasmon band width increases as the radius of nanoparticles is decreased and it is inversely proportional to the particle radius. By the modification of Mie theory, by accounting for the size effects in term of the reduction of the effective electron mean free path and enhanced electron scattering at the particle surface, the size dependence of the optical absorption spectra of metal nanoparticles is correctly explained. Following the model of reduction of the effective electron mean free path and enhanced electron surface scattering the phenomenological damping constant, γ, is introduced as function of the particle radius (equation 23). For a bulk metal the damping constant is expressed as a sum over all reciprocal relaxation times of electron-electron, electron-phonon, and electron-defect scattering process, while for very small particles the surface acts as an additional scatterer where the interactions of conduction electrons with the surface prevail and the electron-surface scattering processes become dominating.

$$\gamma = \gamma_0 + \frac{Av_F}{r} \tag{23}$$

where γ_0 is the bulk damping constant dependent on the electron scattering frequency, r is the radius of the particle, v_F is the velocity of the conduction electrons at the Fermi energy and A includes details of scattering process (scattering process constant). This model provides the correct dependence of plasmon bandwidth and particle dielectric constant on the size for nanoparticle described by the dipole approximation in the intrinsic size regime. In this size region, where the material dielectric function is size dependent, the absorption wavelength increases while the peak width decreases with increasing particle size. [76]

The existence of the plasmon resonance is obtained due to the collective motion of electrons in a metal nanoparticle where any individual electron is not significantly displaced from its origin position. The charge separation as the main restoring force for electron oscillation in a metal nanoparticle is the most important factor in determining the frequency and intensity of plasmon resonance. The energy of this collective mode can be tuned by varying the size and the shape of metal particle. For the non-spherical particles

where surface plasmons are unevenly distributed around particle in particular the shape-dependence of surface plasmon resonance is pronounced. Since the exact solutions of Maxwell's equation are geometrically limited, for various particles shapes, an approximation is required for solving the equation. For the isolated nanoparticles of arbitrary geometry the discrete dipole approximation (DDA) is a particularly powerful numerical method.

DDA method is very advantageous since every problem can be approached in the same way by defining sufficiently fine grids that represent complex environment and provides converged results. [68] In a DDA method the nanoparticle is discretized and it is represented as cubic lattice of N polarisable points, where each point represents the polarizability of a discrete volume of the material. Under the electromagnetic field the dipole moment in each point is obtained. For the steady state conditions each dipole is polarized by the field of both the incident light and other dipoles in the array. As a result of determined absorption and scattering cross section, and cross-sectional area, the dimensionless optical coefficients corresponding exactly to the N point array, are obtained. [68,77] Based on discrete dipole approximation calculations (DDA) for 40 nm silver nanosphere, the particles primarily absorb blue light, while the extinction, absorption and scattering, spectra shows a presence of two resonance peaks. The main peak at 410 nm is ascribed to the dipole resonance, whereas a smaller peak at 370 nm corresponds to quadrupole resonance. The dipole resonance arises from appositively charged sides of a sphere surface which induces a dipole moment in the particle that reverse sign at the same frequency as the incident irradiation. Energy losses that make the incident light nonuniform across the sphere induces the quadrupole resonance, characterized by two parallel dipoles of opposite sign. As the shape deviates from the spherical more nongenerate modes arise and many more peaks over a broad spectral range are obtained in the optical spectrum as compared to only one plasmon resonance (all possible modes are degenerate) for the spherical particle. The number of peaks exhibited in optical spectrum of non-spherical particles compared to the single resonance frequency for spherical particle is increased due to the increasing number of distinct symmetries for dipole resonance. In Figure 14 shape-dependent number of SPR bands obtained for particles of various geometries is schematically illustrated.

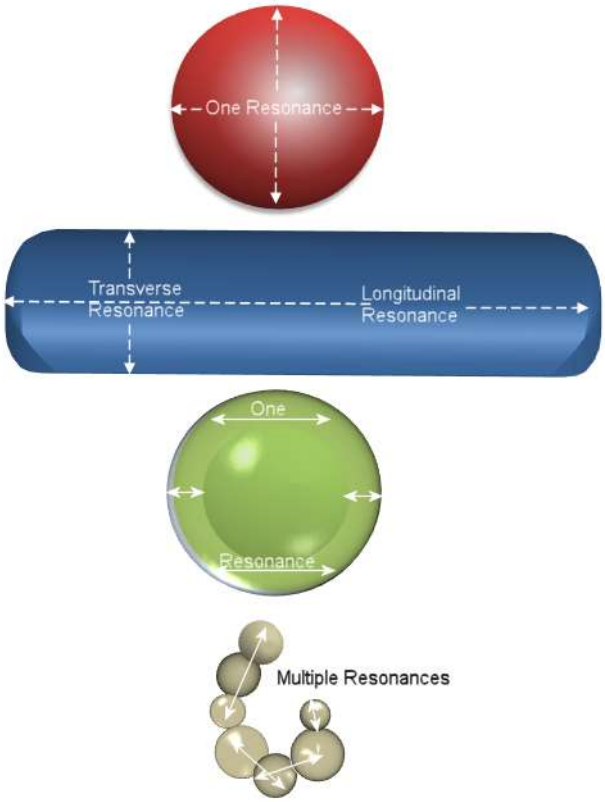

Figure 14: Schematic illustration of plasmon resonance bands in particles of various geometries: (a) spherical nanoparticle, (b) nanorod, (c) hollow sphere and (d) aggregate.

Furthermore, the red shift of the most intense SPR peak compared with that of the sphere is often observed for nanostructures with sharp edges. For these nanostructures surface charges accumulate at sharp corners, which increases charge separation and thereby reduce the restoring force for the electron oscillation. Therefore the weaker restoring force is manifested in a red shifted resonance peak. Among cube, tetrahedron and octahedron the tetrahedron has the most red-shifted SPR peaks because it has the sharpest corners. Figure 14 shows the DDA calculations representing several ways in which the shape of the nanostructure affects the features of nanostructure scattering and absorption characteristics. Similar trends are observed for the hollow spheres (shells) originating from existence of surface charges inside and outside the shell induced by the incident electromagnetic field. DDA calculations show that due to the greater charge separation within shell the near-field is four times enhanced compared to those of sphere.

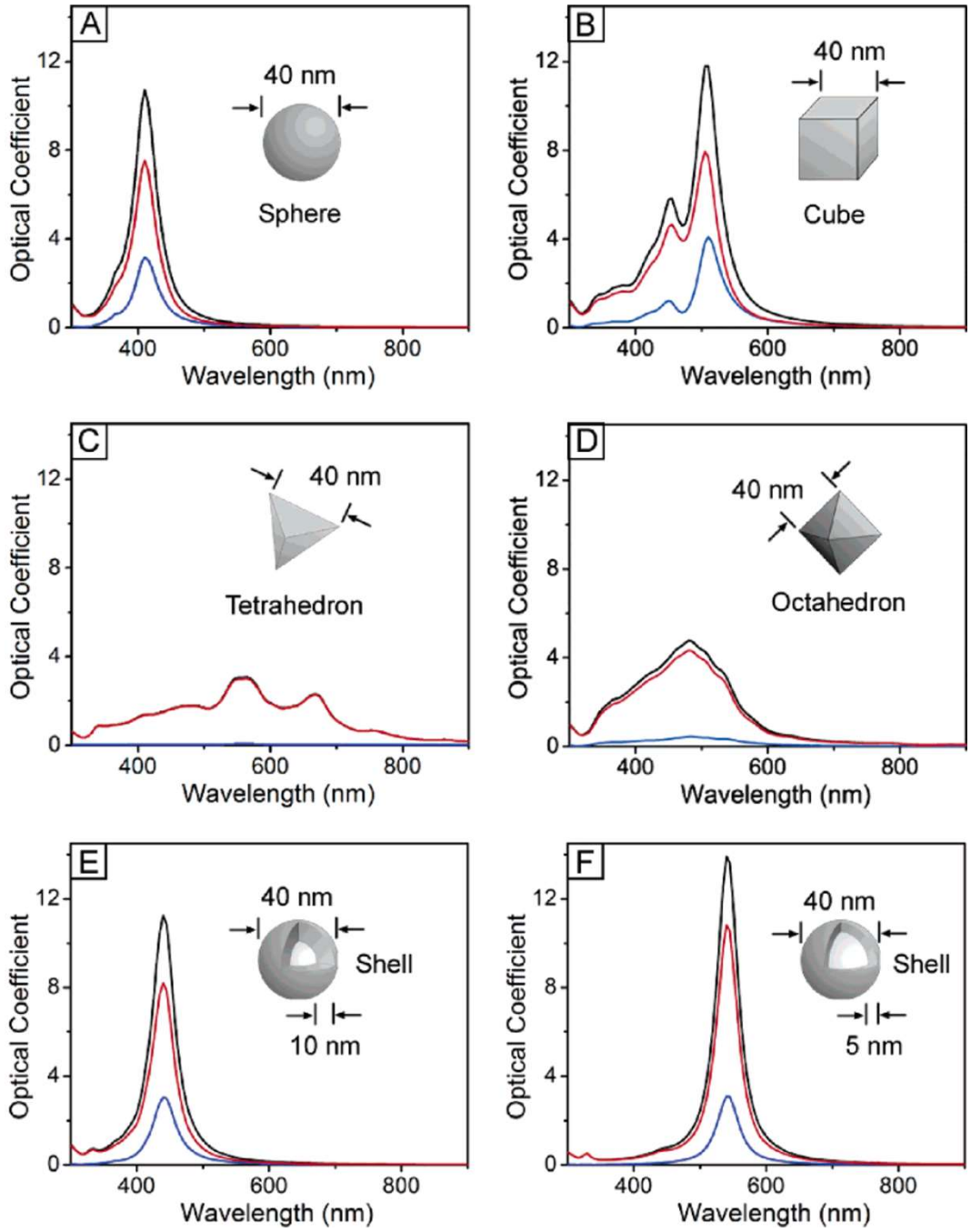

Figure 15: The calculated UV-vis extinction (black), absorption (red), and scattering (blue) spectra of silver nanostructures, illustrating the effect of a nanostructure's shape on its spectral characteristics. Isotropic sphere (a) exhibit spectra with a single resonance peak. Anisotropic structures: cubes (b), tetrahedra (c) and octahedra (d) exhibit spectra with multiple, red-shifted resonance peaks. The spectra of a triangular plate (e) and circular disc (f) illustrate how resonance peaks red-shift for particles with 2D anisotropy. [77]

For metallic elongated structures the plasmon resonance splits into low- and high-energy absorption bands that depend on their aspect ratio. The high-energy band corresponds to the oscillations perpendicular to the major i.e. long axis referred as the transvers plasmon absorption, while the low-energy or longitudinal surface plasmon absorption band is caused by the oscillations of the free electrons along the major axis. As the aspect ratio increases the separation between the two plasmon peaks becomes more pronounced as shown in Figure 16. [78]

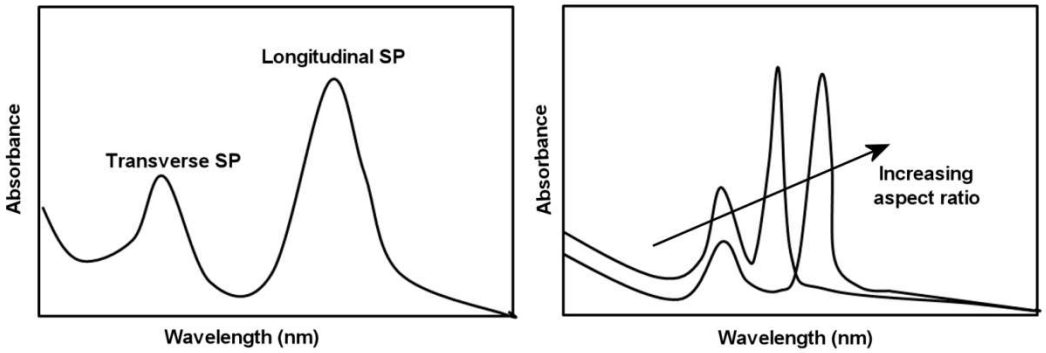

Figure 16: LSPR absorbance spectrum for a non-spherical metallic structure i.e. nanorod. (a) in the metallic nanorod the plasmon resonance splits to a transverse and longitudinal SP and (b) as the aspect ratio is increased the separation between the two peaks becomes more pronounced.

However, the LSPRs that typically arise in nanostructures of noble metals resulting in enhanced and geometrically tuneable resonances are not limited only to metal nanostructures and can be achieved in semiconductor nanoparticles that are characterized with appreciable free carrier concentrations. Recently, well defined LSPRs were demonstrated in semiconductor QDs arising from p-type carriers in vacancy-doped semiconductor $Cu_{2-x}S$ QDs. A set of the absorbance peaks attributed to quantum confined excitons with the lowest energy peak corresponding to the quantized bandgap, which blue-shifts with decreasing QD size. The free carriers are holes rather than electrons as in the case of metals. Well-defined, sharp plasmon absorption peaks in the free-carrier absorption NIR region are related to the high monodispersity and low degree of inter-particle aggregation. [79] As doping allows the modification of electronic, optical and magnetic properties of semiconductor nanocrystals the ability to control the vacancy densities in these nanocrystals opens new possibilities for active tuning of nanoplasmonic responses. For copper(I)oxide nanorods increasing density of free carriers due to copper vacancies generation emerge occurrence of LSPR band in NIR region with progressively increase of intensity and blue-shifts as the density of formed free-carriers is increased.

1.3.1.2 Quantum confinement effect in nanosized semiconductors

The reduction in particle size leads to significantly different physical, in particular optical properties. By the reduction of nanoparticle size a pronounced effect on the energy level spacing, that is increased as the particle become more confined, is obtained. In nanometer regime the semiconductors exhibit different properties due to the confinement effect. Once the diameter of the particle is decreased to the size comparable to the average distance between electron and hole, known as the bulk exciton Bohr radius, the quantum confinement effect can be observed. These nanoentities exhibit optical features that result from an incomplete band structure caused by the limited number of atoms. In an ideal semiconductor the electrons occupy the completely filled valence band which is separated from energetically higher empty conduction band by the gap between them i.e. bandgap. Depending on the size of the bandgap which can be manipulated by varying the particle size, a semiconductor can absorb light of any wavelength. As the semiconductive nanoparticle size is reduced to the size comparable to the material's exciton Bohr radius electrons start to feel the particle boundaries. As a result of confining dimensions to the nanoscale, the continuous energy bands of bulk material become discrete similar to electronic structure characteristic for atoms. [80, 81] The electronic structure of bulk and

quantum dot semiconductor is schematically represented in Figure 17.

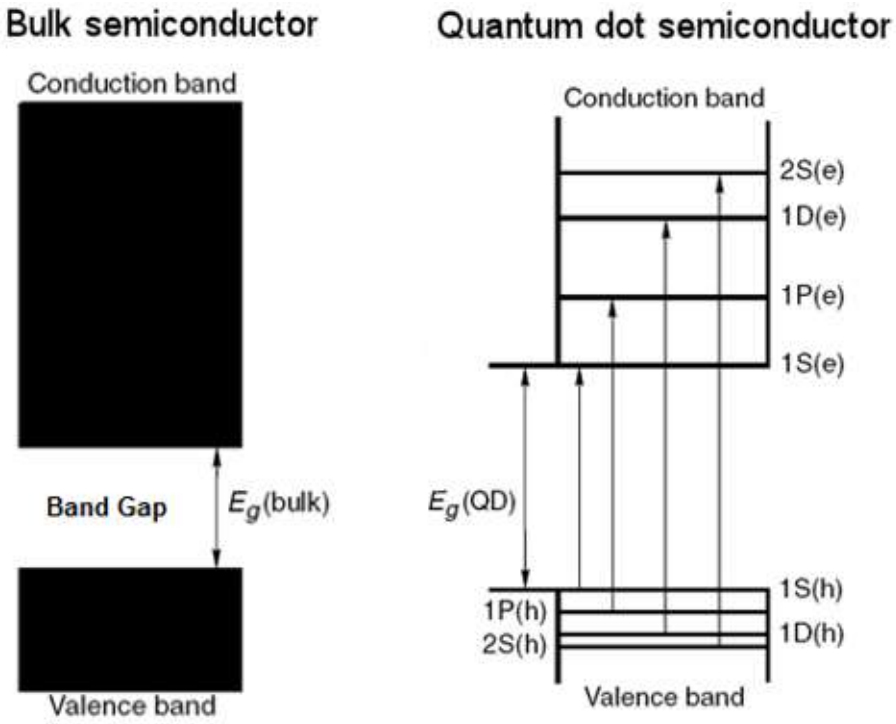

Figure 17: A bulk semiconductor with continuous conduction and valence energy bands separated by an energy gap, Eg (band gap), which is for a bulk semiconductor fixed. Electrons normally occupy all states up to the edge of the valence band, whereas states in the conduction band are empty. (left) A quantum dot is characterized by discrete atomic-like energy states that are size dependent. These well-separated QD states can be labeled with atomic-like notations, such as 1s, 1p, and 1d. (right)

The quantum confinement effect can be described by the particle in box model, in which the electron motion is restricted in all three dimensions. The energy of the band gap of a nanoparticle differs from bulk by

$$E_g(QD) \approx E_{g_0} + \frac{\hbar^2 \pi^2}{2 m_{eh} R^2} \tag{24}$$

where $\hbar$ is the Planck's constant, m_{eh} is the effective mass. The effective mass is defined as

$$m_{eh} = \frac{m_e m_h}{m_e + m_h} \tag{25}$$

where m_e and m_h is the free electron mass and hole mass, respectively.

As deduced from the equation 24 the energy gap of a QD depends on the size of the dot. For a spherical nanoparticle with radius R, a size dependent contribution to the energy gap is proportional to $1/R^2$, which implies that the band gap becomes size dependent. As the nanocrystal size decreases the gap increases. Consequently, the optical absorption of nanocrystals shifts to the blue (higher) energies as the size of the nanocrystal is decreased. Therefore by varying the size of the nanostructures their optical characteristics can be manipulated. [82, 83] For QDs, in addition to quantum size effects doping of nanoparticles with different materials enables control over the dimensions of

the band gap of nanoparticle. By doping additional energy levels are introduced into the electronic structure of material that enables nanostructured semiconductors to absorb visible light.

Due to the nanosized dimensions and a large surface to volume ratio a significant number of the atoms is located on the surface of the particle. In order to tune their properties the control over the crystal structure and surface defects of nanosized particles is necessary.

Apart of semiconductor nanoparticles the semiconductor oxide nanowires and nanotubes have been extensively investigated due to their unique electronic and optical features, such as the high surface to volume ratio, quantum confinement effect, charge transport and carrier lifetime. These unique properties enable their potential applications in many areas; in photocatalytic processes, hydrogen generation, heterogeneous catalysis and in nanoscale electronic and optoelectronic devices including high-performance nanowire-based field-effect transistors (FETs), sensors, dye-sensitized solar cells etc. Sensing behaviour is one of the most important properties of metal oxide materials, since metal oxides sensors usually exhibit much higher sensitivity, selectivity and stability to their chemical environment in comparison to chemical/biosensors. The enhanced sensitivity of the 1-D systems to the chemical environment is usually interpreted as a result of large surface to volume ratio. With a large surface to volume ratio and a Debye length comparable to the nanowire radius, the electronic property of the nanowire is strongly influenced by surface processes, yielding superior sensitivity than bulk counterpart. In particular, due to their semiconductive nature, high optical and chemical stability, high aspect ratio and specific surface area the TiO_2- and titanate-based (Ti-O-based) one dimensional nanostructures are widely applied in the dye sensitized solar cells, hydrogen sensors and photo-electrochemical processes such as photo-catalysis, photo-splitting of water and self-cleaning ability under UV irradiation.

1.4 One-dimensional Ti-O-based nanostructures-assisted photocatalysis

For the effective photoexcitation of certain semiconductor photocatalyst, application of light with energy higher than its bandgap energy that results in existence of electrons in conduction band and holes in valence band is required. Upon radiation the valence electrons are delocalized and excited to the conduction band creating the electron-hole pair called exciton. Most of the excited electrons and holes undergo recombination, while a fraction of photogenerated electrons and holes migrate to the surface of photocatalyst, where they are trapped in metastable surface states and participate in redox reactions with chemicals adsorbed on the surface. When suitable species (electron donor or electro acceptor) are available to trap the hole or electron, recombination is suppressed resulting in subsequent photocatalytic reactions on the semiconductor surface. Photocatalytic reaction at the surface occur either direct via valence band hole or via the surface-bound highly powerful oxidizing species hydroxyl radical (•OH) obtained by surface reaction between trapped valence band hole and –OH or H_2O. Highly powerful •OH radicals are non-selective and thus attack wide spectrum of organic compounds that after sufficiently long irradiation time and proper reaction conditions result in the degradation of pollutant to CO_2 and H_2O (mineralization).

The photocatalytic activity of the material is controlled by the light absorption coefficient and coefficient of the photocatalyst, oxidation and reduction rates on the surface by the electron and hole, and the recombination rate. Additionally, photocatalytic activity is related to the specific surface area of photocatalyst. The larger the surface area of the photocatalyst the higher is photocatalytic activity. However, surface defects

characteristic for large surfaces make the surface to act as defective site resulting in the faster recombination rate, since the defective sites represent recombination centers that enhance electron-hole recombination rate.

In Figure 18 a general mechanism of photocatalysis in the presence of most widely investigated and applied semiconductor photocatalyst TiO_2 is shown. TiO_2 has a wide-band gap of 3.2 eV, which limits its optical activity to the UV region of the solar spectrum. Since, the UV wavelengths represent only 3-4% of the total spectrum of sun radiation, the TiO_2-based photocatalyst utilization is limited only to the outdoor applications. In order to extend the photocatalyst's activity to a wider region, in particular, to the visible wavelengths of the sunlight, modification of semiconductor electronic band structure that will suppress the recombination rate is required. Several approaches have been proposed such are cation or anion doping of the semiconductor lattice and fabrication of metal/TiO_2 composites.

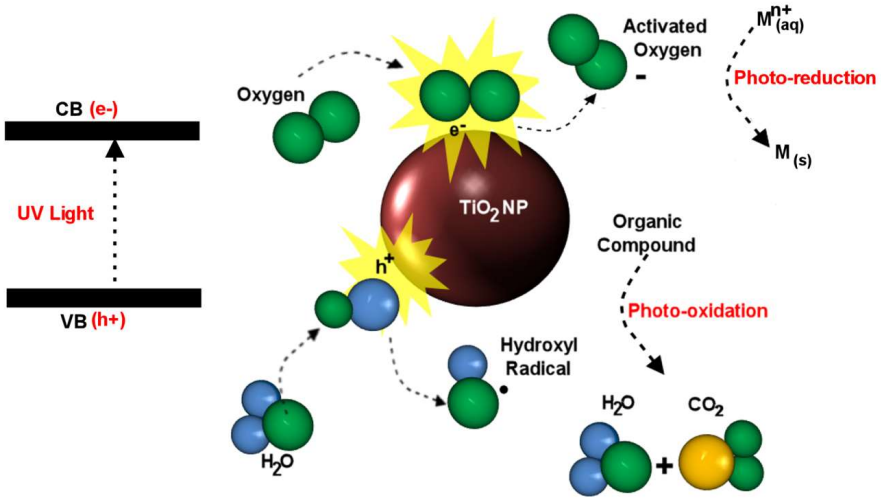

Figure 18: Mechanism of TiO_2 photocatalytic degradation process. Under UV illumination, the wide bandgap semiconductor TiO_2 photocatalyst absorbs photons with energy equal or higher than its band gap energy (< 385nm) and undergo charge separation. These photo excited charge carriers initiate the degradation of the adsorbed chemical species.

For the photocatalytic efficiency of Ti-O-based materials the limiting factor is electron transport since the structure of those materials is a crucial parameter that influences the electron transport. In particular, the structural disorder at the interface of two crystalline nanoparticles results in decreased mobility of electrons due to the enhanced scattering caused by the increased amount of defects, structural imperfections acting as scattering sites. The efficiency of the photocatalytic process on the surface of the TiO_2 particles with a large surface area primarily depends on the crystalline structure that facilitates the photon induced electron–hole pairs generation with reduced recombination rates. Beside the crystallinity that determines efficiency of the photo-induced process, and dimensions, for the control over the selectivity of the photocatalyst the morphology is an important parameter. One-dimensional (1D) nanostructured materials, such as nanotubes and nanofibers, are of particular significance due to their superior physicochemical properties, such as remarkable electronic, magnetic, optical, catalytic, and mechanical properties.

The elongated morphology, nanosized inner cavities and channels, the high specific area and semiconductor electronic properties render one-dimensional titanate-based nanostructures including nanotubes, nanowires, nanorods and nanobelts promising

materials for many applications such as solar cells, hydrogen sensing and storage, lithium batteries, catalysis and photocatalysis. A highly crystalline nature, which can reduce the recombination of photogenerated electron-hole pair, a high specific surface area needed for acceleration of the interfacial rate and an abundance of surface –OH groups required for the generation of OH radicals during photocatalytic reactions are features by which the best TiO_2 photocatalysts are characterized and are intrinsic to one-dimensionally nanostructured titanates. [1] Although that all aforementioned properties make the elongated titanate- and TiO_2-based materials promising materials for photocatalytic reactions, the relatively short wavelength necessary for photo-response of these materials limit their commercialization and widespread industrial use. Several approaches for sensitisation of one-dimensional titanate-based nanostructures to visible range of solar spectrum were explored and reported in the literature. One of the successful approaches to enhance the sensitivity of titanate-based one-dimensional nanostructures in visible range of light is to dope it with nitrogen by which additional energy levels are introduced into the forbidden zone of band gap of titanate. Recently, enhanced photocatalytic activity was observed in various semiconductor–noble metal nanocomposites [17, 18]. With the high noble metal–semiconductor contact area, under photo-excitation the metallic nanostructures in the composite act as electron traps and hence suppress the electron-hole recombination in the semiconductor. The lower Fermi level of the noble metal compared to the semiconductor thermodynamically favours an interfacial electron transfer from semiconductor to metallic nanostructures, which results in charge equilibration, yielding an enhanced catalytic efficiency for the composite system [19]. Additionally, visible photocatalytic activity induced by surface plasmon resonance (SPR) was observed in various noble metal–titania and titanates nanocomposites [20, 21]. It was suggested that an electric near-field in the vicinity of the metal nanoparticles in the nanocomposites may yield an electron excitation from the metal nanoparticles to the semiconductor, which results in an improved photocatalytic activity. The characteristics of the SPR and thus the plasmonic effect in the photocatalyst highly depend on the metal's particle size and shape [22].

2 Aims and Hypothesis

Titanate-based one-dimensional (1D) nanostructures are characterized as a layered, lamellar structure with mesoporous morphology, which may facilitate the transport of ions to the surface of the elongated nanostructures. The ability of ion-exchange of titanate-based 1D nanostructures has been utilized for the formation of Ca-doped titanate nanotubes and nanostructured $CaTiO_3$. Implementation of titanate nanotubes as a template material ensures formation of modified or new materials of nano-dimensions with elongated structure inherited from the parent nanotubes.

For the realization of enhanced photo-catalytic efficiency of elongated titanate-based nanostructures in broader region of solar spectrum i.e. extended in the visible regime several approaches that modify electronic band structure of titanate-based nanostructures by introducing the additional energy levels within their band gap have been introduced. However, additional energy levels can also act as electron-hole traps, and hence reducing photo-efficiency.

Recently, various fabrication routes utilized for the noble metal-semiconductor 1D titanate nanostructures nanocomposites have been introduced toward obtaining hybrid materials with enhanced photosensitivity in the visible range of solar light. Visible photo response is induced by the electromagnetic near field triggered by the characteristic local surface plasmon resonance of metallic nanoparticles which is metal's particle size and shape dependent. The synthesis approaches for the preparation of metal-titanate nanocomposites discussed in the literature are mostly based on the precipitation of metal oxide from the aqueous solution of metal salt followed by subsequent thermal, chemical or photochemical reduction yielding metallic nanoparticles. Common to all these synthetic routes is the lack of any ability to control the size and the density of the metallic nanoparticles in the composite nanostructures, which may limit their efficiency for photocatalysis. On the other hand, the use of organic matrixes has proven to be an effective route to obtaining control over the size and the density of the metallic component.

The layer-by-layer self assembly technique has been used to fabricate organic-inorganic composites with controlled polyelectrolyte multilayered film thickness. Moreover, due to its ability of precise size and density control the layer-by-layer self assembled polyelectrolyte multilayer (PEM) film on the surface of various nanostructures has been applied as a nanoreactor for the *in-situ* metallic nanoparticle synthesis. With this approach obtaining the control over the size, size distribution, density, morphology and crystallinity of the metallic component building nanocomposite is crucial for the tailoring of the properties of the metallic nanoparticles-semiconductor nanocomposites.

The thesis focuses on semiconductive titanate based one-dimensional hydrothermally synthesized nanostructures (nanotubes and nanobelts) as templates for fabrication of nanostructured materials and one-dimensional nanocomposites. Weak polyelectrolyte multilayer films formed by the layer-by–layer self assembly technique on the surface of titanate nanostructures prior to the one-dimensional nanocomposites fabrication were implemented as a nanoreactor for the inorganic nanoparticles (metallic Ag and Cu) controlled wet chemical *in-situ* synthesis. Furthermore, weak PEM was also utilized in the two-step fabrication procedure of titanate-based nanobelts thin films.

The goals of this thesis were

- To control the morphology, size, crystallinity and crystal structure of the nanosized titanate-based one-dimensional materials by changing the synthesis condition
- To introduce hydrothermally synthesized one-dimensional titanate-based nanostructures as template for fabrication of Ca-doped titanate-based elongated nanostructures and $CaTiO_3$ nanocrystals by hydrothermal method, and utilization of these titanate nanostructures as a one-dimensional nanostructured component forming semiconductor based nanocomposite
- To elucidate the formation mechanism of nanostructured perovskite through topotactic reaction under hydrothermal conditions
- To develop fabrication procedure of one-dimensional nanocomposite based on titanate-based nanostructures and metallic (Ag, Cu) via self assembly of weak polyelectrolytes
- To control and evaluate the growth characteristics of the metallic Ag and Cu nanoparticles formed within the weak polyelectrolyte multilayer assembled on the surface of one-dimensional titanate-based nanostructures
- To tailor the optical properties and photocatalytic activity of one-dimensional nanocomposites: Ag nanoparticles/titanate nanobelts, Cu nanoparticles/titanate nanobelts
- To employ the polyelectrolyte assisted synthesis and assembly as an effective fabrication strategy for the formation of 3D nanostructures (thin films).

3 Materials and Methods

3.1 Hydrothermal synthesis and characterization of 1D titanate-based nanostructures and nanostructured $CaTiO_3$

Anatase TiO_2 powder (99.9 %, Alfa Aesar) and NaOH (>97 %, Carlo Erba) were used for the synthesis of 1D titanate-based nanostructures; i.e. nanotubes (Ti-NTs) and nanobelts (Ti-NBs). $Ca(OH)_2$ (95%, AlfaAesar) was used for the synthesis of Ca-doped 1D titanate-based nanostructures and nanocrystals of $CaTiO_3$.

The Ti-NBs and Ti-NTs were hydrothermally synthesized using Anatase TiO_2 powder and NaOH. The reaction mixture was composed of 4.4 g of TiO_2 and 30 ml of 10 M NaOH, stirred for 5 minutes and then sealed in a 100-ml, Teflon-lined, stainless-steel container. The hydrothermal reaction was performed at 200°C, 48 hours for the synthesis of Ti-NBs and at 165°C, 72 hours for the preparation of Ti-NTs, respectively. After the reaction the Ti-NBs and Ti-NTs were rinsed with distilled water by centrifugation (Eppendorf, Centrifuge 5810R), dried over night at 80°C in a drying oven and stored under ambient conditions.

In the fabrication procedure of Ca-doped 1D titanate based-nanostructures and $CaTiO_3$ perovskite nanocrystals the sodium titanate nanotubes/nanobelts were used as a template material that provides the anisotropic shape for the final product. As starting materials, 0.5 g of hydrothermally synthesized Ti-NBs and Ti-NTs, 30 ml of deionized water and 0.85 g of $Ca(OH)_2$ (95%, Alfa Aesar) were used. An excess of $Ca(OH)_2$ served as the reagent for maintaining the alkaline environment and as a source of calcium cations. The ion-exchange reaction was carried out at various temperatures (100°C, 130°C, 150°C and 200°C) and times (12 h and 5 days) in a 100 ml Teflon-lined stainless steel autoclave. The as-prepared products were washed with a copious amount of distilled water using a centrifuge (Eppendorf, Centrifuge 5810R) and then dried over night at 80°C in a drying oven. Samples were stored under ambient conditions.

In order to synthesize the nanostructured perovskite $CaTiO_3$ without using a 1D titanate-based template, the hydrothermal treatment of 0.5 g of Anatase TiO_2 powder, 0.85g $Ca(OH)_2$ and NaOH was performed at 200°C. Aqueous solution of NaOH was added drop-wise in order to maintain the same initial pH value of the reaction mixture as in the case of reaction mixtures used in the hydrothermal treatment of the 1D precursors in the presence of $Ca(OH)_2$. The reaction was performed in a sealed, Teflon-lined stainless steel autoclave. The 100 ml autoclave was filled up to 30% of a Teflon reactor volume (as in the case of the hydrothermal treatment of the 1D titanate-based precursors). The products were washed with a copious amount of distilled water, centrifuged (Eppendorf, Centrifuge 5810R) and dried at 80°C over night in the oven.

The electrophoretic mobility of the Ti-NBs was measured to determine their zeta-potential using a ZetaPal (BIC, USA). The reported value of the zeta-potential is an average of ten measurements made under constant conditions.

The Brunauer-Emmett-Teller (BET) surface area of the hydrothermally synthesized 1D titanate-based nanostructures was determined by N_2 adsorption-desorption isotherms recorded with a Gemini II 2370 Surface Area Analyzer (Micromeritics Norcross, Georgia,

USA). The samples were out-gassed at 110°C in He for 15 hours. The specific surface area was calculated in the relative pressure range 0.05 < P/P0< 0.2.

For the determination of the phase composition of the synthesized products, the X-ray powder diffraction (XRD) patterns were recorded in the ranges of 2Θ = 5° - 70° and 2Θ = 15° - 70°, using two X-ray powder diffractometers: a Bruker AXS D4 Endeavor (radiation wavelength CuKα = 1.5406 Å) and a PANalytical X'Pert PRO (radiation wavelength CuKα = 1.5406 Å) with a Johansson monochromator.

A transmission electron microscopy (TEM) was employed for the determination of the morphology of all products by using a transmission electron microscope Jeol, JEM-2100 equipped with an energy-dispersive spectrometer (EDS, JEOL, EX – 24063JGT). The morphological, structural and growth characteristics were examined using high-resolution transmission electron microscopy (HRTEM). The energy-dispersive spectroscopy (EDS) and selected-area electron diffraction (SAED) were used for determination of the chemical composition and the crystal structure of the products, respectively. Additionally, the chemistry of titanate-based nanostructures and $CaTiO_3$ was studied by the electron-energy-loss spectroscopy (EELS) using JEOL, JEM-2010F transmission electron microscope.

3.2 Synthesis of Ag/Ti-NBs composites by weak-polyelectrolyte assisted Layer-by-Layer self-assembly method

The positively charged polyelectrolyte Poly(allylamine hydrochloride) (PAH, Sigma Aldrich) and the negatively charged polyelectrolyte Poly(acrylic acid) (PAA, 25% aqueous solution, Polysciences) were used for the fabrication of the polyion multilayer on the surface of Ti-NBs. Silver acetate - CH_3COOAg (anhydrous, 99%, Alfa Aesar) was used as the source of the silver (Ag^+) for the formation of the silver (Ag^0) nanoparticles. Deionized water with a pH value of ~ 5.0 was used in the fabrication process of the polyion multilayer and nanocomposites. The pH value of this water was adjusted by the drop-wise addition of 0.1 M HCl.

The polyelectrolyte multilayers (PEMs) of PAH and PAA were assembled on the surface of the hydrothermally synthesized Ti-NBs by first immersing them into the PAH solution with a concentration of 0.01 M (by repeat unit) for 5 minutes, followed by rinsing with water and centrifugation. The Ti-NBs were then immersed into the 0.01 M solution of PAA for 5 minutes, followed by the washing procedure and centrifugation. By repeating the polyelectrolyte adsorption and washing steps a PEM film of 10.5 PAH/PAA polyion bilayers was formed on the surface of the Ti-NBs, where one bilayer of the PEM is defined as a single adsorption of polycation (PAH), followed by an adsorption of the polyanion (PAA). After the assembly, the Ti-NBs-PEM composites were dried over night at 95°C in a drying oven and then stored under ambient conditions.

The Ag nanoparticles were synthesized within a 10.5 PAH/PAA bilayered polyion multilayer matrix assembled on the surface of the Ti-NBs with the *in-situ* methodology. For the *in-situ* synthesis of Ag nanoparticles the Ti-NBs-PEM nanocomposites were immersed in an aqueous solution of silver acetate with a concentration of 0.01 M overnight, where the acid protons of the PAA are exchanged by the silver cations. After the ion-exchange reaction the composite was washed, centrifuged several times with deionized water and dried in a drying oven at 95°C. The number of reaction cycles (N) of the Ag nanoparticle synthesis in the PEM, composed of the silver cation binding to the ionized carboxylic groups of PAA and the subsequent formation of Ag_2O nanoparticles within the PEM matrix was varied from N = 1 to N = 3 (the thus-synthesized inorganic-organic composite will be denoted in the text as Ag_2O(N)/Ti-NBs-PEM, where the

number of Ag-ion loading cycles is marked by N). Finally, the crystalline nanocomposites Ag/Ti-NBs were obtained by a subsequent removal of the organic PEM film during annealing at 600°C for 0.5 h in air (the thus-formed metallic Ag/Ti-NBs composite nanostructures will be assigned in the text as Ag(N)/Ti-NBs, where N denotes the number of Ag-ion loading/precipitation cycles in the PEM). The composite fabrication procedure is shown in Figure 19.

The chemical and phase composition of the Ti-NBs and the Ag_2O(N)/Ti-NBs-PEM composites were evaluated from the energy-dispersive spectroscopy (EDS) and X-ray powder diffraction (XRD) patterns recorded in the range of 2Θ = 5–70° by using a D4 Endeavor, Bruker AXS X-ray diffractometer (radiation wavelength CuKα = 1.5406 Å).

Transmission electron microscopy (TEM) using a JEOL JEM-2100 was employed for the determination of the morphological characteristics of the composites. Based on the TEM images, the diameters of approximately 100 nanoparticles were measured to evaluate the average Ag nanoparticle size in each sample. The density of Ag_2O and Ag nanoparticles within a PEM matrix and on the surface of Ti-NBs prior to, and after, the annealing was then calculated from the TEM images by scanning an $81*10^{-4}$ μm^2 area of the nanocomposite. The structural characteristics of the as-formed Ti-NBs and composites Ag/Ti-NBs and the growth characteristics of Ag nanoparticles were determined by high-resolution transmission electron microscopy (HRTEM) and selected-area diffraction (SAED) performed on multiple nanostructures.

The Brunauer-Emmett-Teller (BET) surface area of the Ti-NBs and Ag(N)/Ti-NBs nanocomposites was determined by N_2 adsorption-desorption isotherms recorded with a Gemini II 2370 Surface Area Analyzer (Micromeritics Norcross, Georgia, USA). The samples were out-gassed at 110°C in helium atmosphere for 15 hours. The specific surface area was calculated in the relative pressure range $0.05 < P/P0 < 0.2$.

The optical spectra of the Ti-NBs and Ag(N)/Ti-NBs nanocomposites were measured using a UV–vis transmission spectrophotometer (Hewlett-Packard 8453). The photocatalytic activities of the Ti-NBs and Ag(N)/Ti-NBs nanocomposites were examined by measuring the photodegradation rates of the Methylene blue (MB) dye using a Tecan Saphire microplate spectrophotometer. After being kept in the dark for 30 min to achieve adsorption equilibrium, the nanostructures in the MB solution were irradiated using a 150W xenon lamp with a 400-nm-UV, cut-off filter and a 36W UV lamp to evaluate the photocatalytic activity in the visible and UV regimes, respectively. After selected time intervals, the residual concentration of the MB dye was measured using a UV-vis spectrophotometer at the characteristic absorption maximum of MB at 662 nm. The self-degradation of the MB under UV and visible light was comprised in the measurements.

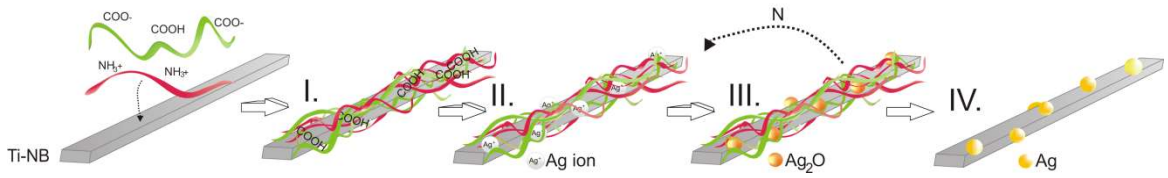

Figure 19: Scheme of the Ag(N)/Ti-NBs composite fabrication procedure.

3.3 Synthesis of Cu/Ti-NBs composites by polyelectrolyte-assisted Layer-by-Layer self-assembly method

The positively charged weak polyelectrolyte Poly(allylamine hydrochloride) (PAH, Aldrich) and the negatively charged weak polyelectrolyte Poly(acrylic acid) with Mw=90 000 (PAA, 25% aqueous solution, Polysciences) were used for the fabrication of the polyelectolyte multilayer film (PEM) on the surface of the Ti-NBs. Anatase TiO_2 powder (99.9 %, Alfa Aesar) and NaOH (>97 %, Carlo Erba) were used for the hydrothermal synthesis of titanate-based nanobelts (Ti-NBs). Copper(II)acetate – $(CH_3COO)_2Cu$ (99.999%, trace metals basis, Aldrich) was used as the source of the copper cations (Cu^{2+}) for the *in-situ* synthesis of copper nanoparticles within PEM matrix. $NaBH_4$ (99.99%, Sigma Aldrich) was used for the reduction of copper cations and subsequent formation of the metallic copper nanoparticles (Cu^0). The positively charged strong polyelectrolyte Poly(diallyldimethylammonium chloride) (PDDA, 35% aqueous solution, Sigma Aldrich) and the negatively charged strong polyelectrolyte Poly(styrenesulfonic acid) sodium salt (PSS, Polysciences) were used for the fabrication of the multilayer film assemblies.

In Figure 20 fabrication procedure of PEM/Ti-NBs and Cu/PEM/Ti-NBs precursors for thin films assembly is schematically shown. The positively charged weak polyelectrolyte Poly(allylamine hydrochloride) (PAH, Aldrich) and the negatively charged weak polyelectrolyte Poly(acrylic acid) with Mw=90 000 (PAA, 25% aqueous solution, Polysciences) were used for the fabrication of the polyelectolyte multilayer on the surface of the Ti-NBs. Deionized water with a pH value of ~ 5.0 was used in the fabrication process. A PEM film of 6.5 polyelectrolyte PAH/PAA bilayers was assembled on the surface of Ti-NBs by immersing them first into 0.01 M solution (per monomer unit) of PAH for 5 minutes, rinsed with water. Following the centrifugation, Ti-NBs were immersed into 0.01 M solution (per monomer unit) of PAA for 5 minutes, washed and centrifuged yielding PEM coated Ti-NBs (PEM/Ti-NBs). Cu-loaded PEM/Ti-NBs precursor structures were formed by immersion of PEM/Ti-NBs structures to the 0.01 M solution of copper acetate for 1 hour. In order to obtain the metallic copper nanoparticles within the PEM, the Cu ion loaded PEM/Ti-NBs were then exposed to the solution of $NaBH_4$ for 1 hour, again washed with distilled water and centrifuged.

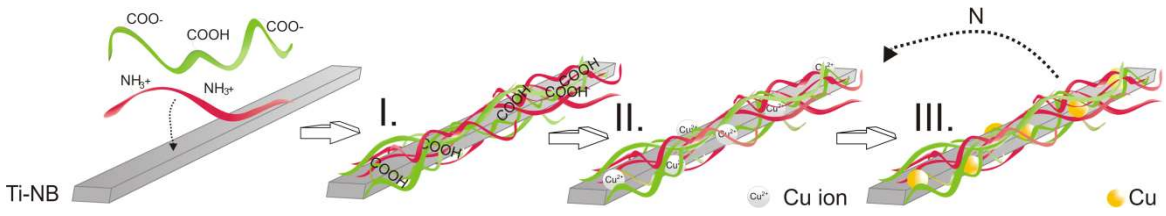

Figure 20: Fabrication of PEM/Ti-NBs precursor and Cu loaded PEM/Ti-NBs precursor structures for the multilayer film assembly.

The X-ray powder diffraction (XRD) was employed for the determination of phase composition of the Cu/Ti-NBs composites. The XRD patterns were recorded in the range of 2Θ = 5–70° by using a D4 Endeavor, Bruker AXS X-ray diffractometer (radiation wavelength CuKα = 1.5406 Å).

The Brunauer-Emmett-Teller (BET) surface area of the Ti-NBs and Cu/Ti-NBs were evaluated by N_2 adsorption-desorption isotherms recorded with a Gemini II 2370 Surface Area Analyzer (Micromeritics Norcross, Georgia, USA). In order to measure BET surface

area the structures were scratched from the substrates. The samples were out-gassed at 110°C in helium atmosphere for 15 hours. The specific surface area was calculated in the relative pressure range $0.05 < P/P_0 < 0.2$.

The morphology of the Cu/Ti-NBs composite nanostructures was examined by using a transmission electron microscopy (TEM, Jeol JEM-2100). Based on the TEM images, the diameters of approximately 100 Cu nanoparticles were measured in order to determine their average size distribution. The structural characteristics of the composite nanostructures and growth characteristics of copper and copper oxide nanoparticles were determined by selected-area electron diffraction (SAED) and high-resolution transmission electron microscopy (HRTEM).

Surface analyses were carried out on a PHI-TFA X-ray photoelectron spectrometer (XPS) (Physical Electronics, Inc., Frickenhausen, Germany) exciting a sample's surface by X-ray radiation from an Al-monochromatic source. The survey and narrow-scan spectra of the emitted photoelectrons were taken with 187 eV and 29 eV. The data were treated with the Multipak program, version 8.1. The sensitivity of the applied method is up to 0.05 at.%. All the data were obtained by averaging at least three repeated integrations of the peaks.

Optical spectra of the composites were measured by using a UV-vis spectrophotometer Hewlett-Packard-8453. The photocatalytic activities of the nanocomposites were studied by measuring the degree of the degradation of the organic cationic dye Methylene blue (MB) under UV and visible light by using a UV-VIS-NIR spectrophotometer (UV-3600 Shimadzu). After being kept in the dark for 30 min to achieve adsorption equilibrium, the composites in the MB solution were irradiated by a 4.5 W LED Parathom PAR16 20 lamp with a irradiation wavelength region of λ = 400 - 700 nm and a 3.5 W Blacklight Blue Lamp to evaluate the photo-catalytic activity in the visible and UV regimes, respectively. The residual MB concentration in the samples taken after particular time intervals was measured by a UV-VIS-NIR spectrophotometer (UV-3600 Shimadzu) at the characteristic absorption length of MB at 662 nm. Self-degradation of the MB under UV and visible light was considered in the measurements.

3.4 Fabrication of Ti-NBs thin films

The silicon (Si (111) oriented single-crystals) and quartz wafers (Si-Mat, Germany) were used as substrates for the fabrication of film assemblies. Prior to the multilayer assembly, the wafers were cleaned in a Piranha solution (H_2SO_4/H_2O_2=75:25 v/v) for 20 minutes and subsequently washed with copious amount of deionized water. To modify the surface charge of the wafer, 2 polyelectrolyte bilayers of positively charged Poly(diallyldimethylammonium chloride) (PDDA, 35% aqueous solution, Sigma Aldrich) and negatively charged Poly(styrenesulfonic acid) sodium salt with Mw=70 000 (PSS, Polysciences) were first assembled on the substrate surface. Wafers were first immersed into PDDA solution for 10 minutes, followed by immersion into water, as a rinsing procedure. Wafers were then immersed into the solution of negatively charged polyelectrolyte PSS for 10 minutes and rinsed by dipping the wafers into water. The adsorption and rinsing steps were repeated to obtain 2 (PDDA/PSS) bilayers. Polyelectrolyte solutions with a pH value of ~ 9.0 were used in the fabrication process. The pH value of this water was adjusted by the drop-wise addition of 0.1 M NaOH.

Modified silicon wafers were utilized for the multilayer film assemblies of the PEM/Ti-NBs precursor structures. Aqueous dispersions of PEM/Ti-NBs were deposited onto wafers mounted on the sample holder of spin coater by vacuum and rotated at speed 2000 min^{-1} for 10 seconds. The multilayers were formed by Layer-by-Layer self-assembly of the precursor structures and appositively charged PSS, rinsed with water after

each sequential step. The sequential deposition of the precursor structures and PSS were repeated until the desired number of bilayers was obtained. To vary the thickness of the films 10 and 20 bilayers of PEM/Ti-NBs precursor structures and PSS were spin coated on the wafers. In order to obtain inorganic Ti-NBs nanostructured films, the PEM/Ti-NBs-PSS (10/20) thin multilayer films were thermally treated at 500°C for 30 minutes in air (scheme in Figure 21). Since dust and other impurities in the working environment greatly influence the quality of thin films, the deposition was carried out in a protective work-bench LFV 12 with a controlled level of contamination.

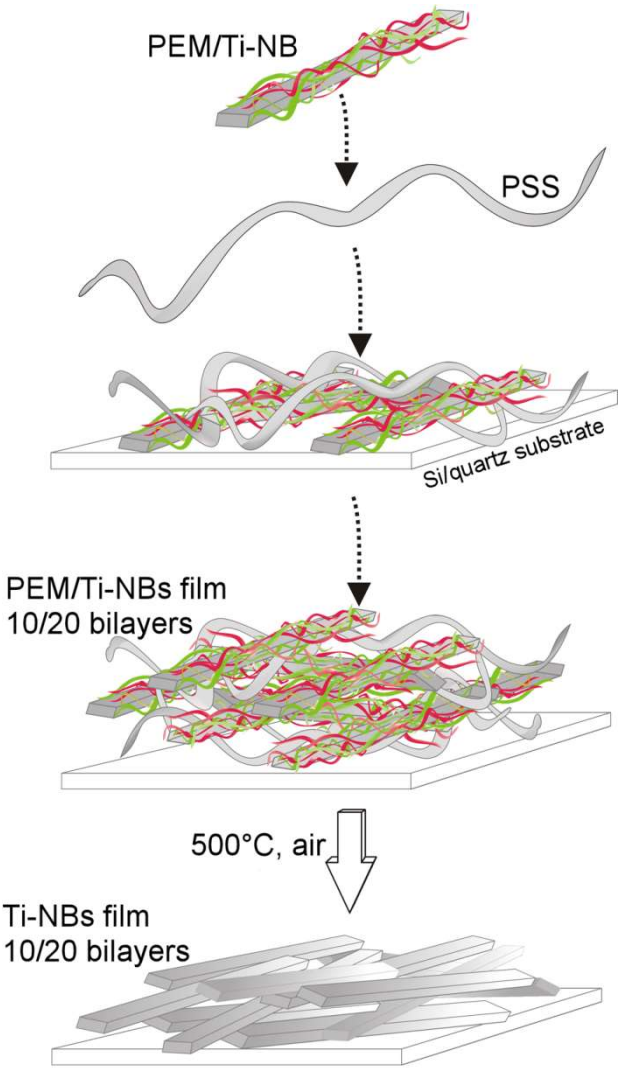

Figure 21: Fabrication procedure for Ti-NBs multilayered films by LbL self-assembly methodology.

The surface morphology of the inorganic multilayer films on the silicon substrates was examined using a field-emission scanning electron microscope (FE-SEM, SUPRA 35VP,Carl Zeiss, Oberkochen, Germany), while roughness of the films was assessed with an atomic-force microscope (AFM, Veeco DI 3100, Nanoscope 4) in a tapping mode.

4 Results and Discussion

4.1 Hydrothermally synthesized 1D titanate-based nanostructures: nanotubes (Ti-NTs) and nanobelts (Ti-NBs)

The hydrothermal treatment of anatase TiO_2 in a highly alkaline solution of NaOH typically results in the formation of various titanate-based nanostructures, where the morphology is temperature dependent. For the temperatures of the hydrothermal reaction below 130°C the two-dimensional nanostructures in form of nanosheets are formed. In the temperature range from 130°C to 165°C the hydrothermal reaction results in the formation of nanotubular structures, while at higher temperatures nanobelts are thermodynamically the favourable morphology. As a result of the hydrothermal treatment at 165°C for 72 hours in a highly alkaline environment the titanate–based nanotubes were obtained. Figure 22(a) shows a typical bright-field TEM image of an aggregate of the nanotubes. As evaluated directly from the TEM images, the individual multiwalled nanotubes were up to several 100 nm long and exhibit uniform outer and inner diameter of 10 nm and 5 nm along their length, respectively. The walls of nanotubes consist of 3-5 layers, while the number of layers on the two sides of the tube usually differs for one (Figure 22(c)). The interlayer distance between neighbouring layers forming nanotube wall obtained directly from the TEM images was evaluated to be approximately 0.9 nm. Additionally the TEM investigations revealed the coexistence of nanotubes and unrolled or partially rolled sheets formed at the early stage of hydrothermal reaction. The presence of partially rolled sheets shown in Figure 22(b) and the uneven number of walls on the two sides of nanotubes (Figure 22(c)) indicate that the nanotubes are hollow scrolls, as clearly shown in Figure 22(d), formed by the rolling of the thin titanate sheets [22, 23].

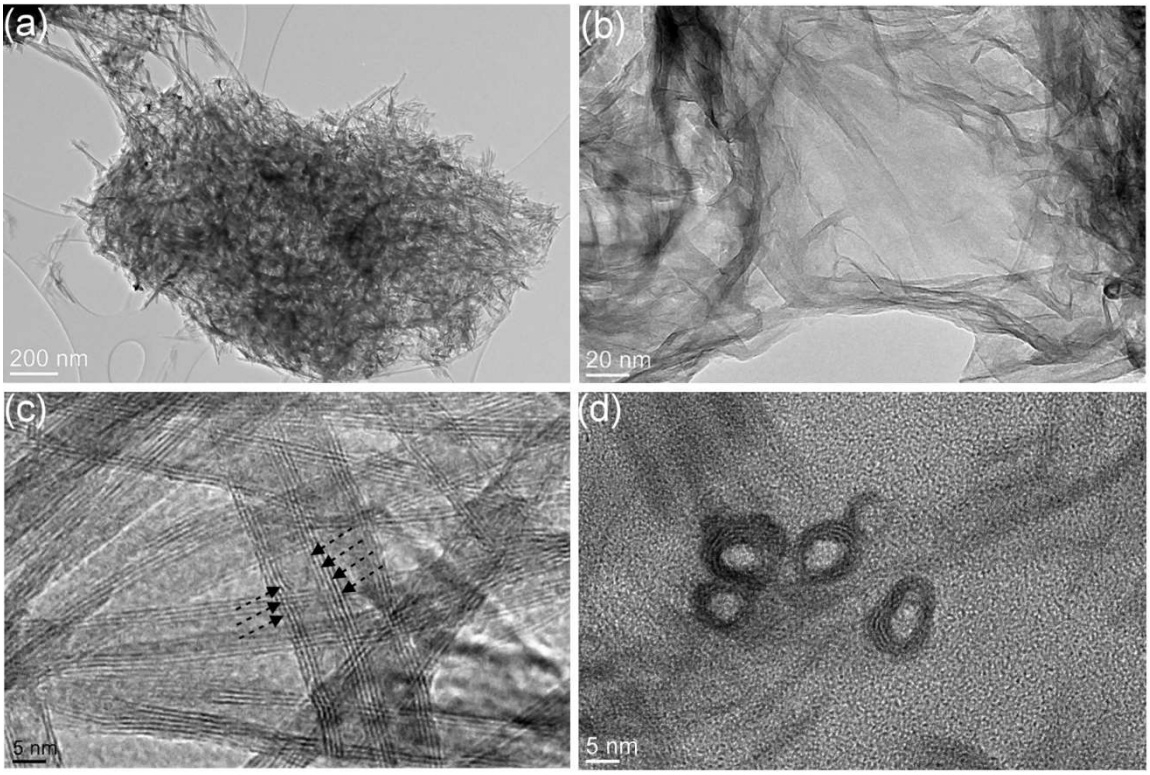

Figure 22: Bright-field TEM image of (a) an aggregate of nanotubular precursor, (b) unrolled titanate nanosheets, (c) high-resolution TEM image of a nanotube and (c) cross-section of nanotubes.

In Figure 23 the XRD pattern (red) of the hydrothermally synthesized nanotubes is shown. The peak obtained at 2Θ angle of ~ 10° is ascribed to the layered structure of the Ti-NTs walls, while other broad peaks of low intensity at 2Θ angles 24°, 28°, 48°and 62° are characteristic for the Ti-NTs containing Na [84]. The similarity of the reflections at small angles in the XRD pattern of various titanates [16, 17, 19, 22-26] ascribed to the nanotubes hinder distinguishing among these structures and thus exact determination of the crystal structure of the nanotubes. Well defined, layered structure with the interlayer distance of approximately 0.9 nm (obtained from the HRTEM images) combined with a characteristic reflection (200) (obtained in the XRD pattern at small 2Θ angles of approximately 10° and denoted by an arrow in Figure 23), the low isoelectric point of ~ 3 and negative value of zeta-potential in aqueous solutions of Ti-NTs, and the presence of approximately 5 at% of sodium determined by the TEM-EDS clearly indicate that the structure of the synthesized Ti-NTs corresponds to one of the titanates and not to the anatase[14, 46] (black pattern in Figure 23). The dimensions of Ti-NTs and the dominance of surface atoms over interior atoms that is intrinsic to nano-sized structures are strongly reflected in the value of specific surface area thus the BET surface area of hydrothermally synthesized Ti-NTs of uniform size distribution, established from the nitrogen adsorption isotherm, was 240 m^2/g.

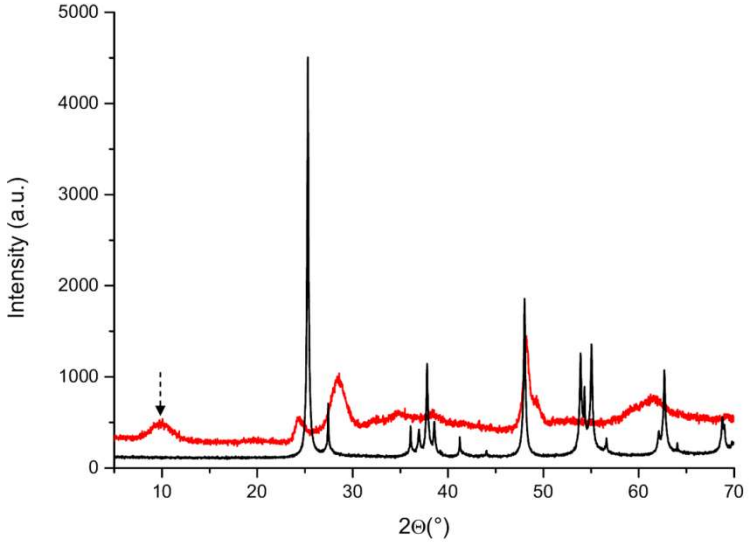

Figure 23: XRD pattern of the titanate-based nanotubes (red) and anatase powder (black). The characteristic peak at d~10Å indicates the formation of the titanate-based nanotubes.

Since the nanostructured titanates formed under hydrothermal conditions exhibit belt-like morphology at reaction temperatures above 165°C, the synthesis performed at 200°C resulted in formation of the phase–pure Ti-NBs [13, 32, 63]. In Figure 24(a) a bright-field TEM image of the hydrothermally synthesized Ti-NBs is shown. The length and the width of the Ti-NBs evaluated directly from the TEM images reveal the broad size distribution of the NBs. The length of the Ti-NBs is in the range between 500 nm and several micrometres, whereas their width typically varies from 50 to 300 nm. The XRD pattern, shown in Figure 24(d) combined with TEM-EDS analysis indicates that synthesized nanobelts are chemically Na-titanates [32].

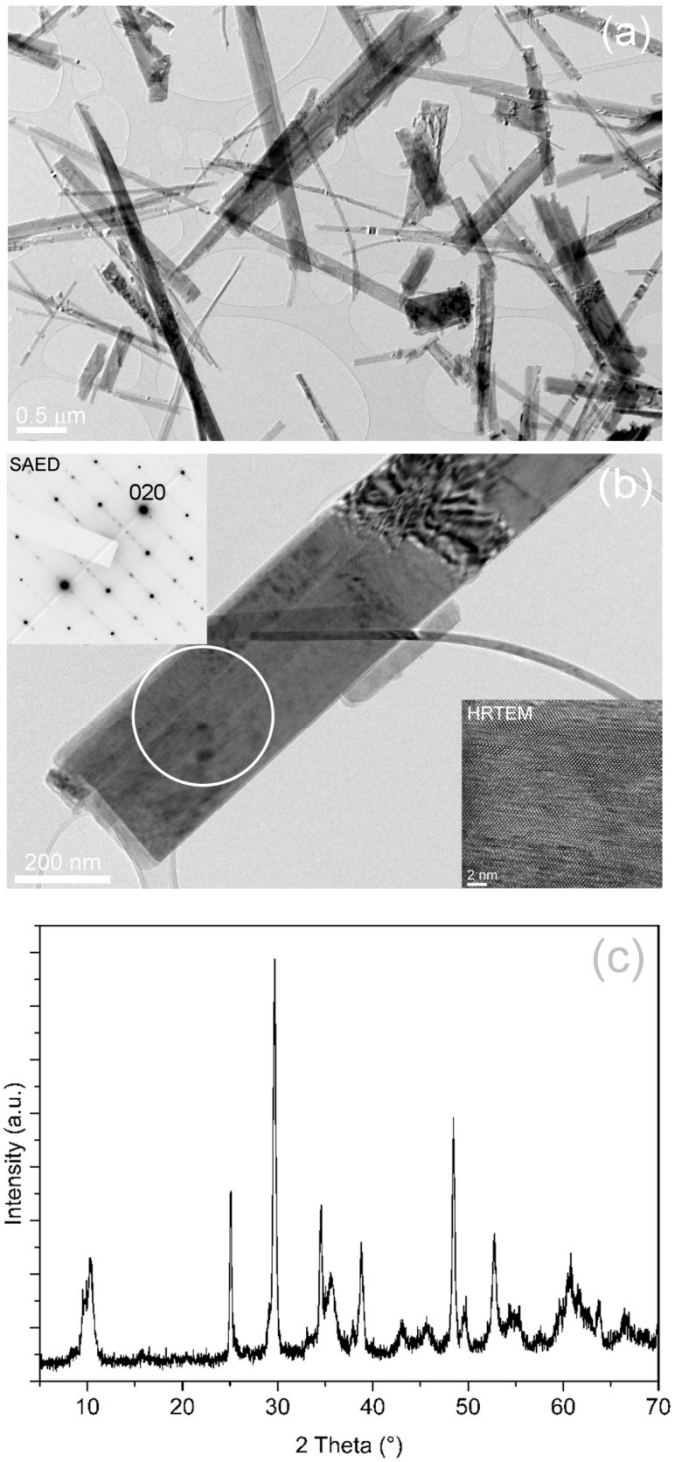

Figure 24: (a) Bright-field TEM image of Ti-NBs, (b) bright-field TEM image of individual Ti-NB with the marked area and corresponding SAED pattern (z = [001]), and HRTEM image of Ti-NB and (c) XRD pattern of hydrothermally synthesized Ti-NBs.

The selected-area diffraction (SAED) pattern shown in the inset of Figure 24(b) indicates that individual Ti-NBs are single crystals. Single crystalline Ti-NBs are elongated in the [010] direction. As is common to all of the monoclinic layered sodium titanates, the layers of Ti-octahedra are parallel to the [010] direction. Furthermore, the sharpness of the peaks in the XRD pattern (Figure 24 (c)) indicates the high crystallinity of the Ti-NBs, as it also confirmed by the HRTEM (inset in Figure 24 (b)). The measured BET specific surface area of the Ti-NBs is about 25 m^2/g. A ten times lower S_{BET} as

compared to the specific surface area of Ti-NTs is ascribed to the dimensions and high crystallinity degree of Ti-NBs. The negative zeta-potential, obtained from the measured electrophoretic mobility of the Ti-NBs, indicates a high concentration of hydroxyl groups on the surface of the Ti-NBs in the solutions with a pH above 2 [1].

4.2 Ca-doped titanate nanotubes (Ca/Ti-NTs) and nanostructured $CaTiO_3$ (CT)

One-dimensional nanostructures are of particular interest since they offer possibilities for fundamental scientific investigations and expand the application-oriented opportunities resulting from their size- and dimensionality-influenced properties. On the other hand inorganic hollow and/or porous nanomaterials have gain great attention as promising bio-active and biocompatible materials for drug-delivery carriers, specific targeting and controlled release systems, implants inducing enhanced regeneration, etc. [85, 86, 87]. In order to realize novel applications, the development is oriented toward the assembly of novel materials and functionalised nanostructures of various morphologies into ordered nanostructures and composites exhibiting novel enhanced properties.

For the designing of functionalised titanate-based nanostructured materials with novel properties a wide range of synthetic approaches has been introduced. Among them template-assisted approach was extensively adopted for the functionalisation of nanoporous, hollow elongated titanate nanostructures [87] and nanosized perovskites [59, 61, 90, 91]. The layered structure of 1D titanate template renders intercalation of various species (alkali metal cations, alkaline earth cations, transition metal cations, nanoparticles, etc.) into interlayer galleries feasible. This enables modification of tubular nanostructured titanates for different applications, among which the photo-catalytic and biomedical applications are of great interest. Intercalation of calcium in the structure of 1D titanate-based nanostructures result in formation of bio-active and bio-compatible Ca-doped Ti-NTs and $CaTiO_3$. In particular utilization of Ca-doped Ti-NTs and $CaTiO_3$ for enhanced apatite formation resulting in faster bone regeneration, minimization of inflammatory response to implants and promoted osteointegration is of great interest. [87, 88, 89]

The hydrothermally synthesized titanate-based nanotubes were used as a precursor/template in hydrothermal ion-exchange reaction. Due to a high mobility of interlayer ions ensured by the layered structure of the titanate precursor the ion-exchange of interlayer sodium cations with Ca^{2+} cations was obtained. The extent of intercalation of calcium into the structure of the Ti-TNs precursor depends on temperature and duration of performed hydrothermal reaction. The topochemical reaction, in which by the ion-exchange reaction the formed products inherited the morphology/shape from a template, while the chemical composition and the crystal structure are changed, was introduced as a synthetic approach for the preparation of calcium doped Ti-NTs and nanostructured perovskites $CaTiO_3$ (CT).

The morphology and the dimensions of template in the form of Ti-NTs are preserved and inherited by the products after the hydrothermal ion-exchange reaction of the interlayer ions by the calcium cations (Ca^{2+}) performed at temperatures up to 130°C and are independent of the reaction duration (Figure 25). The Ca-exchanged nanotubes were from 100 nm up to several μm long, the outer and the inner diameters were about 10 nm and 5 nm, respectively, while the interlayer distance measured directly from the TEM images was approximately 0.9 nm. The EDS analysis revealed the presence of calcium and a small amount of sodium, which is present due to the incomplete ion-exchange reactions or insufficient washing after the reactions. With the prolonged duration of the reaction at 100°C the Ca/Ti ratio after 12 h and after 5 days of reaction was 0.4 and 0.5,

respectively. With the increase of reaction temperature up to 130°C and reaction time the morphology of the applied template is successfully preserved, whereas the maximum amount of about 11 at% of intercalated calcium was achieved.

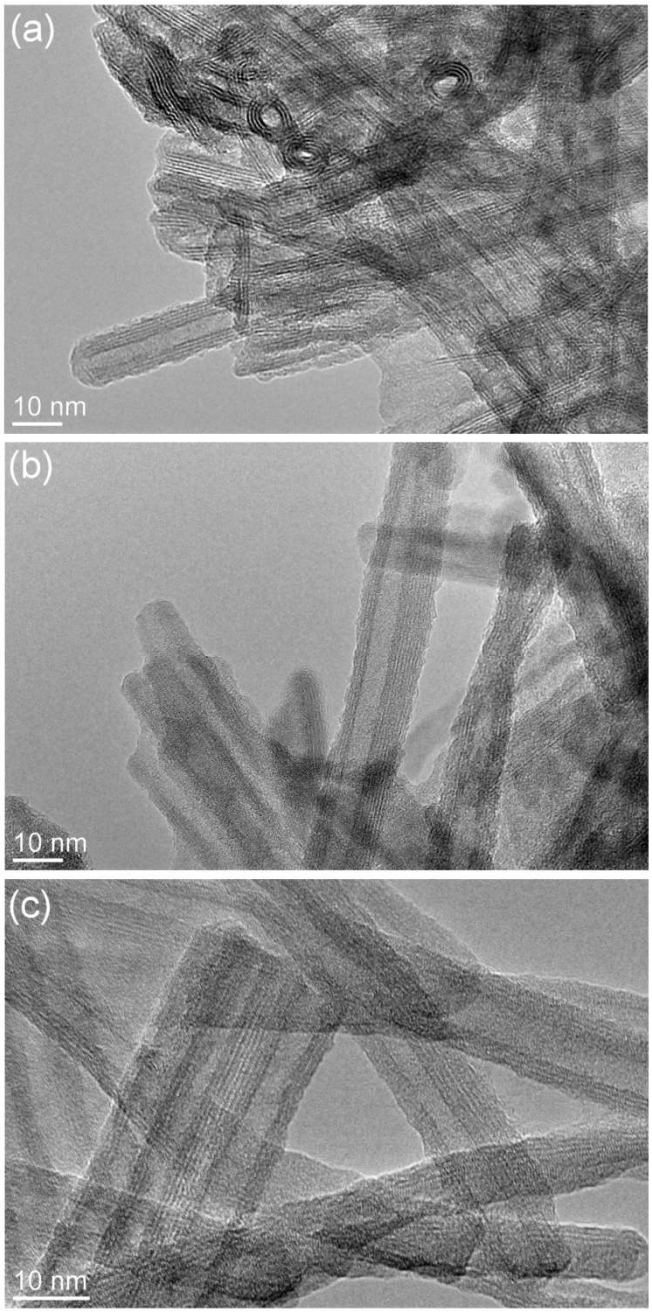

Figure 25: Bright-field TEM images of Ca/Ti-NTs after hydrothermal reaction performed at (a) 100°C for 12 hours, (b) 100°C for 5 days and (c) at 130°C for 12 hours.

The increase of the temperature of the hydrothermal reaction resulted in the formation of anisotropic crystals. In Figure 26 clusters composed of nanostructured crystals formed during hydrothermal treatment of Ti-NTs in presence of $Ca(OH)_2$ at 150°C and 200°C are shown. From the bright-field TEM images the estimated length and width of the crystals were 500 nm to 800 nm and 100 nm to 300 nm, respectively. The Ca/Ti ratio of the as-formed crystals, determined by the EDS, was approximately 1. A typical SAED pattern

shown in the inset of Figure 26(b) indicates formation of single crystalline $CaTiO_3$ nanocrystals with orthorhombic crystal structure. The crystals joined in an individual cluster are oriented in the same direction, while the crystal growth proceeds in the [010] direction with respect to the orthorhombic perovskite unit cell.

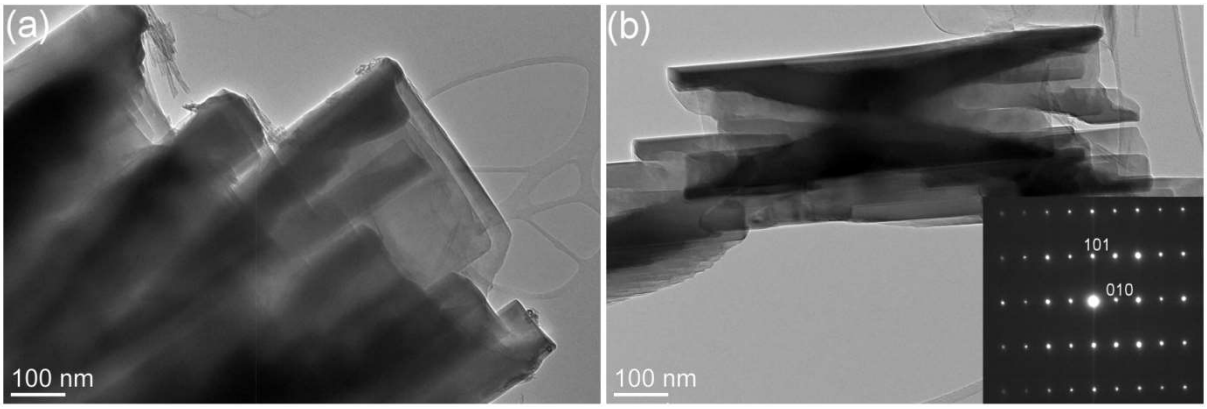

Figure 26: Bright-field TEM image of anisotropic crystals with curled edges formed by the hydrothermal treatment of a nanotubular titanate precursor at (a) 150°C for 12 hours and (b) at 200°C for 12 hours (inset: SAED pattern of a single-crystalline orthorhombic $CaTiO_3$, z = [-101]).

The XRD patterns shown in Figure 27 indicate the formation of highly crystalline crystals of $CaTiO_3$ as the temperature is increased to the 150°C, while the degree of crystallinity and the dimensions of crystals are not significantly influenced by further increase of the reaction temperature (200°C). Since the hydrothermal reaction is performed in highly alkaline environment maintained by the addition of the excess quantities of $Ca(OH)_2$, after reaction some amount of the residual $Ca(OH)_2$ may react with the CO_2 from the ambient air and/or water forming $CaCO_3$ as indicated by the additional peaks in the XRD patterns shown in Figure 27.

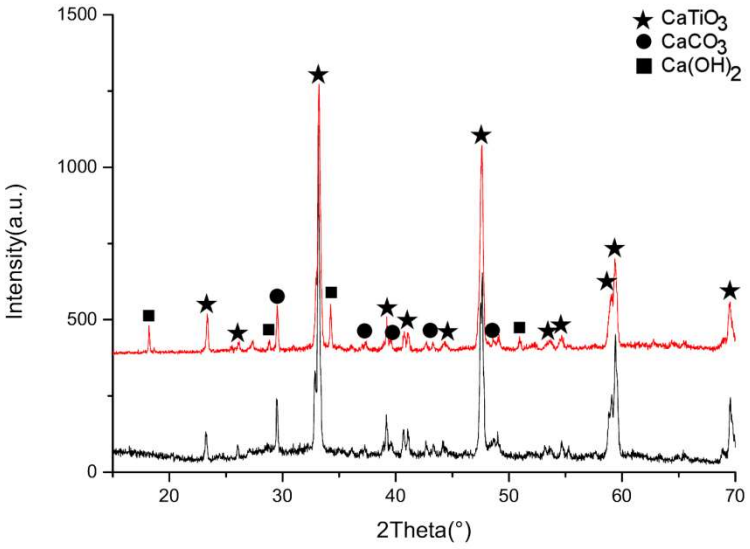

Figure 27: XRD pattern of $CaTiO_3$ hydrothermally synthesized at 150°C, 12 hours (black pattern) and (b) 200°C, 12 hours (red pattern).

The morphology, the inner and the outer diameters, the length and the width, and the Ca/Ti ratio of the nanostructures formed during the hydrothermal treatment of the nanotubular titanate-based template performed at different synthesis conditions are summarized in Table 1.

Table 1: Morphology, dimensions and Ca/Ti ratio of nanostructures formed by the topochemical reaction of nanotubular template.

Hydrothermal conditions	Morphology	Inner diameter or Width (nm)	Outer diameter or Length (nm)	Ca/Ti ratio
100°C, 12 h	Nanotubes	4-5	100-several 100	0.4
100°C, 5 days	Nanotubes	4-5	100-several 100	0.5
130°C, 12 h	Nanotubes	4-5	100-several 100	0.4
150°C, 12 h	Nanosized crystals	100-300	500-800	1
200°C, 12h	Nanosized crystals	100-300	500-800	1

Furthermore, the TEM analysis (Figure 26) revealed formation of $CaTiO_3$ crystals with irregular edges, curled perpendicular to the growth direction of the crystals. Although for other perovskites such as $BaTiO_3$ and $SrTiO_3$ any potential template effect, even at lower temperatures, has been questioned,[90,91] for the $CaTiO_3$ is assumed that the evolution of the perovskite structure during the hydrothermal treatment of the titanate-based nanotubular template and the formation of $CaTiO_3$ single crystals with the observed morphology are template-assisted.

On the other hand single-step reaction i.e. the hydrothermal treatment of commercially available anatase TiO_2 powder in presence of $Ca(OH)_2$ at 200°C resulted in the formation of flat crystals with regular edges, as shown in Figure 28. After the single-step reaction solely flat rectangular crystals with regular edges were obtained. From the TEM images directly evaluated the width and the length of as-formed nanocrystals were 80-200 nm and 150-350 nm, respectively. EDS elemental analysis of the crystalline nanocrystals showed stoichiometric ratio of calcium and titanium that corresponds to $CaTiO_3$. Typical SAED pattern shown in the inset of Figure 28 indicates formation of single crystalline orthorhombic $CaTiO_3$ crystals that are slightly elongated in [010] direction.

According to the observations based on TEM analyses of crystals synthesized by both approaches it is assumed that unconventional morphology of $CaTiO_3$ crystals formed by the hydrothermal treatment of the nanotubular template may result from the tubular morphology of the template entering the hydrothermal reaction.

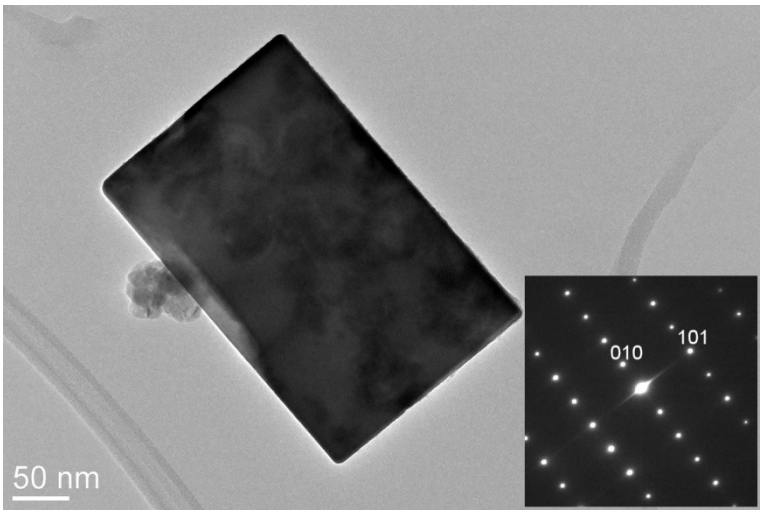

Figure 28: Bright-field TEM image of nanosized rectangular crystal synthesized by hydrothermal treatment of anatase powder at 200°C for 12 hours. Inset shows SAED pattern indicating formation of single crystalline orthorhombic $CaTiO_3$, [z = -101].

4.3 Metallic nanoparticles/Ti-NBs composites

In the field of environmental chemistry the photocatalysis has become an area of vast research interest. In this regard nanostructured titania (TiO_2) as multifunctional material with remarkable chemical, electronic and optical properties is frequently utilized as a photo-active material for fabrication of efficient photocatalysts that are employed in processes of photo-degradation of various pollutants triggered by the mechanism of charge generation, photon induced charge separation and electron transfer related to the titania bandgap (~3.2 eV) which makes it photoactive in UV portion of the solar spectrum. Due to the limited activity of titania to the UV region of light, for the sensitization into visible region and improvement of charge separation the 1D titanate nanostructures are of particular interest. It was established that they exhibit enhanced photo-activity, in comparison to other TiO_2-based low dimensional materials, associated to their elongated morphology that slows down the exciton recombination dynamics, which is favourable for the photo-catalytic process. However, in spite of the increased photo-sensitivity of titanate-based nanostructures, the photo-response of these materials is still dominated in UV region. This limits their wide spread use and commercialization. To extend their photo-sensitivity into visible range, a variety of methods that modify the electronic band structure of titanate-based nanostructures and improve charge separation by decreasing the recombination have been introduced.

Since the enhanced photocatalytic activity in UV and visible regime was observed in various noble metal – semiconductor nanocomposites, recently, high-aspect-ratio titanate-based one-dimensional nanostructures, synthesized by the alkaline hydrothermal treatment of TiO_2, and characterized by high specific surface area and semiconducting properties have been utilized as templates or catalyst supports for one-dimensional assemblies of functional noble metal nanoparticles with high surface-to-volume ratio, such as Au, Ag and Cu. A high surface-to-volume ratio and strong optical absorption arising from the surface plasmon resonance of metal nanoparticles and large metal-semiconductor contact area are unique features that make such composites suitable for performance of photo-catalytic processes in wide region of wavelengths of the light.

Due to the higher work function of the noble metal compared to the electron affinity of

the semiconductor an interfacial charge transfer from semiconductor to metallic nanostructures occurs, which results in equilibration of the Fermi levels of the two systems. [92] Photoexcited nanostructured semiconductor in contact with metal nanoparticles undergoes charge equilibration. Such composites exhibit shift of the Fermi level toward more negative potentials, which enhances efficiency of charge transfer, yielding an enhanced catalytic response for the composite system. Additionally, visible photocatalytic activity assisted by the near-field amplitudes of the localized surface plasmon resonance (LSPR) of the metallic nanoparticles was observed in various noble metal–titanates nanocomposites [93, 94]. The characteristics of the LSPR and thus the plasmonic effect in the photocatalyst are dependent on the metal's particle size and shape and can potentially influence electronic properties of nanocomposite[95]. For this reason, an effective synthesis approach for fabrication of a nanocomposite with the ability to obtain control over the metallic nanoparticle size and concentration is required.

4.3.1 Ag/Ti-NBs composites

Among the noble metals, silver (Ag) exhibits the lowest Fermi level and is therefore the one most often chosen for the preparation of metal/semiconductor photocatalytic nanocomposites. Previously, the composite Ag/Ti-nanostructures were fabricated by ion-exchange/precipitation method. With this method first Ag_2O nanoparticles precipitated on the surface of titanate-based nanostructures usually from an aqueous solution of $AgNO_3$. [96, 97, 98]. After annealing above 400°C, chemical reduction with NBH_4 or UV treatment Ag ions were completely reduced to metallic Ag nanoparticles. Certain control over the size and density of the primary formed Ag_2O nanoparticles on the surface of Ti-nanostructures can be obtained by varying the pH and concentration of the metal ion solution. High surface coverage with small sized nanoparticles is limited by the extended aggregation of primarily formed particles. Furthermore, subsequent heat treatment resulted in increased Ag particle size and large size distribution of the as formed Ag nanoparticles on the surface of Ti-nanostructures (the size range between 10-40 nm was observed). By this method, with very low Ag ion concentrations Ag particle size above 10 nm were obtained. [96, 97] Due to the broad size distribution the precise evaluation is not possible. The lack of the ability of obtaining control over the size and size distribution of the Ag nanoparticles formed by ion exchange/precipitation procedure hinders control over the final photocatalytic properties of the as formed composite nanostructures. While on the contrary, the utilization of organic templates has proven to be an effective route to obtaining control over the size and the concentration of the metallic component [95, 99]. In particular, weak polyelectrolyte multilayer (PEM) templates formed by the Layer-by-Layer (LbL) self-assembly of appositively charged polyions have been shown to be promising as nanoreactors for the synthesis of *in-situ* silver nanoparticles. In this synthetic approach, by changing the pH value of the polyelectrolyte assembly and/or by repeating the ion-loading/precipitation reaction cycles the control over the size and particle concentration on the surface of elongated titanate nanostructures is obtained. [99, 100].

4.3.1.1 Fabrication, and structural and morphological characterization of Ag/Ti-NBs composites

A PEM template composed of polyallylamine (PAH) and polyacrylic acid (PAA) were first assembled on hydrophilic surface of titanate-nanobelts with the Layer-by-Layer self-

assembly technique. At an assembly pH value of 5.0 a 10.5 bilayered multilayer with an average thickness of 25 nm was obtained on the surface of Ti-NBs, as can be seen from Figure 29.

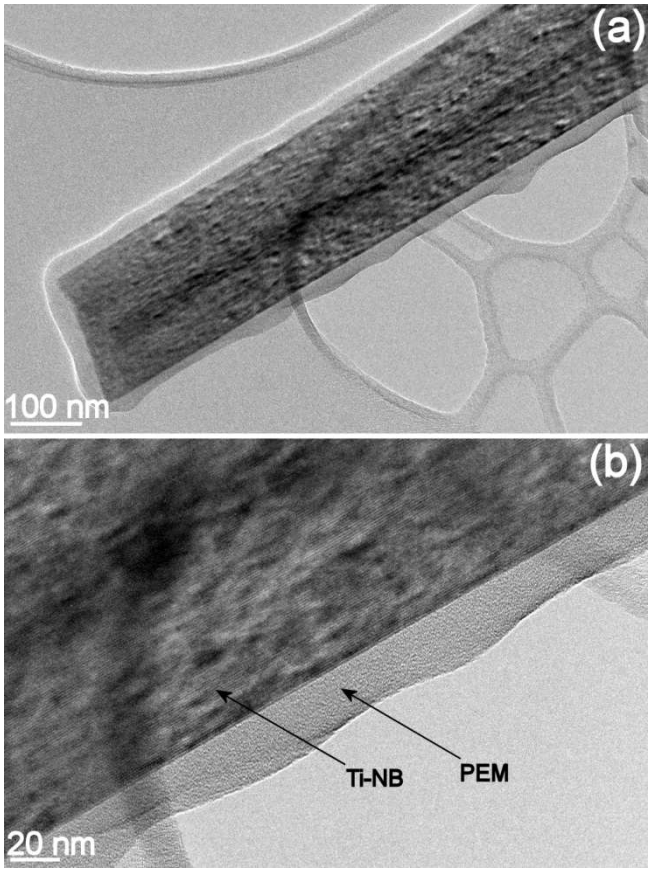

Figure 29: Bright-field TEM image of Ti-NBs-PEM composite.

At the assembly pH of 5 a certain content of unionized carboxylic acid groups exists within the PEM [101]. As the PEM-coated Ti-NBs are exposed to the Ag^+ ion solution at pH values higher than those during the polyelectrolyte assembly, Ag^+ ions infiltrate within the PEM, where they bind to the carboxylate groups [95]. With the *in-situ* nanoparticle synthesis approach in polyelectrolyte multilayer (PEM) the primary particles are formed within the nanopores of the multilayer assembly. The surrounding polymer chains prevent nanoparticle agglomeration and thus enable the precise control over the nanoparticle size with narrow size distribution. After a six-hour exposure of PEM-coated Ti-NBs to the aqueous solution of Ag^+ ions the Ag_2O nanoparticles were formed within the PEM. Formation of the Ag_2O nanoparticles within PEM voids was indicated by the XRD pattern shown in Figure 30.

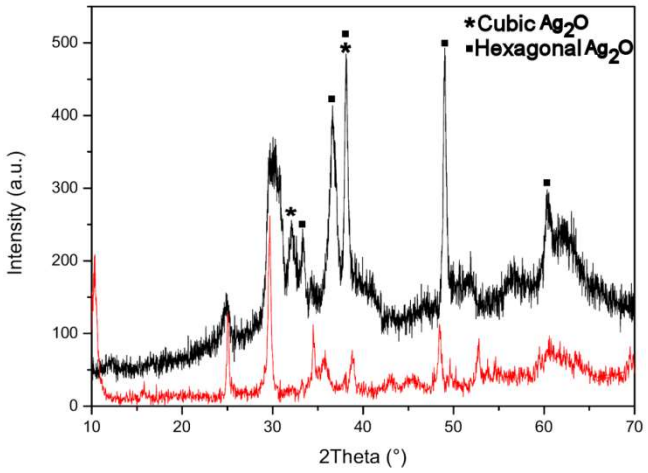

Figure 30: XRD pattern of Ag_2O/Ti-NBs-PEM composite (black) and pure Ti-NBs (red).

The primary Ag_2O nanoparticles are formed within PEM template by subsequent chemical reaction of the silver cations proposed by Equation 26. With the *in-situ* nanoparticle synthesis approach in PEM the incorporated Ag ions react with the hydroxyl groups detached from the surface of Ti-NBs. These hydroxyl groups may penetrate into the PEM, where they react with incorporated Ag cations resulting in the formation of the intermediate Ag_2O particles. It is assumed that the high concentration of the surface hydroxyl groups on the Ti-NBs induces the precipitation of the Ag_2O nanoparticles [97, 102] within the PEM by the direct reaction of the Ag^+ and OH^- ions. The control over the concentration and the size of the particles within the polymer film was obtained by cycling the synthesis process.

$$2Ag^+ + OH^- \rightarrow Ag_2O + H_2O \qquad (26)$$

TEM images (Figure 31) of the PEM-coated Ti-NBs with the in-situ precipitated Ag_2O particles after N = 1, N = 2 and N = 3 reaction cycles indicate that the as-formed Ag_2O nanoparticles within the PEMs are spherical and homogeneously distributed throughout the multilayer film.

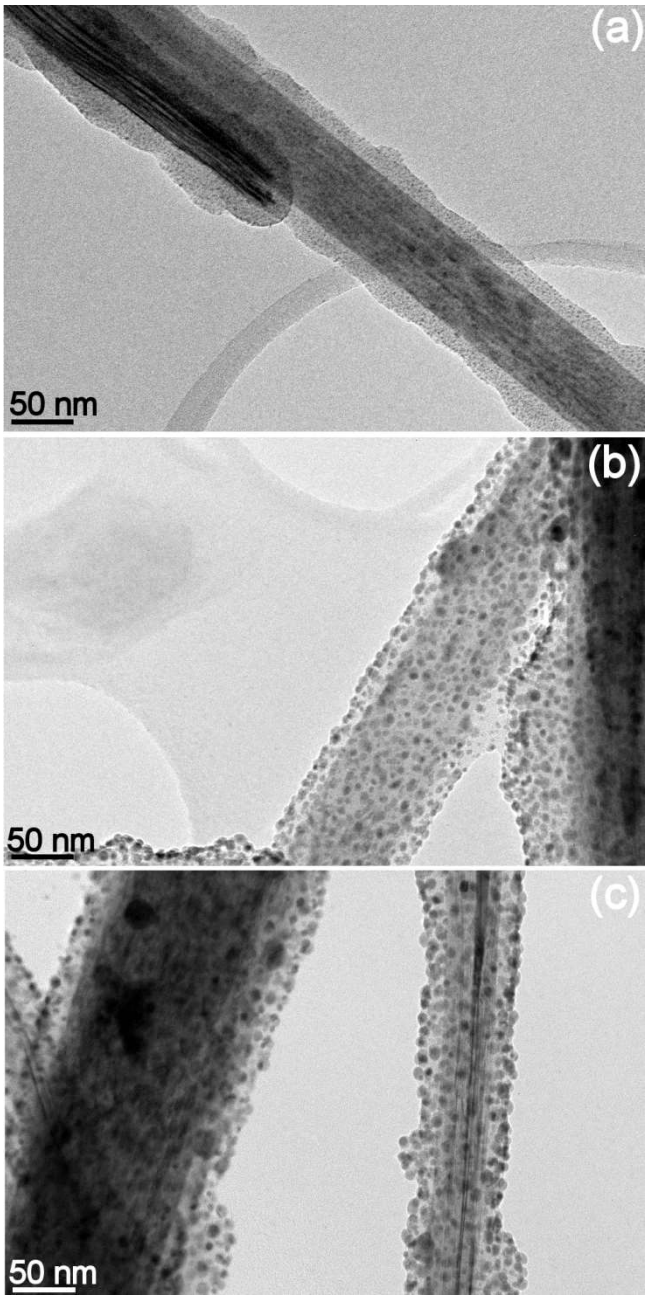

Figure 31: Bright-field TEM images of (a) Ag_2O(1)/Ti-NBs-PEM, (b) Ag_2O(2)/Ti-NBs-PEM and (c) Ag_2O(3)/Ti-NBs-PEM.

As the reaction cycle was repeated from N = 1 to N = 3 an increase in the size of the Ag_2O nanoparticles from 2.4 nm to 8.3 nm was observed (Table 2).

Table 2: Size and density of Ag_2O nanoparticles in Ag_2O(N)/Ti-NBs-PEM nanocomposites

Number of reaction cycles	Ag_2O nanoparticle size (nm)	Ag_2O nanoparticle density ($*10^4$ μm^{-2})
n=1	2.4±0.6	8.2
n=2	4.9±1.4	1.4
n=3	8.3±2.3	0.8

After the first reaction cycle of the Ag_2O particle formation the carboxylic groups within the PEM overlayer are regenerated, which enables further Ag-ion loading. Although the Ag_2O nanoparticles formed in the PEM are sterically stabilized by the surrounding polymer matrix, each subsequent binding of Ag^+ ions into the proximity of the existing particles after their reaction with hydroxyl groups favours the dissolution-precipitation growth of larger particles at the expense of smaller ones within the PEM [100]. Consequently, a decrease in the particle density with the increasing average size of the Ag_2O nanoparticles in the PEM is observed as the reaction cycle is repeated.

In general, the precipitation reaction of the metal ions within the PEM results in the formation of single-crystal, inorganic, spherical particles [95, 100]. Previously examined growth characteristics of inorganics in PEM suggest that the initially formed Ag_2O particles within the PEM are single crystals, and with annealing above 280°C the Ag_2O thermally decomposes into metallic silver and oxygen [103, 104]. The thermally induced release of oxygen from the Ag_2O nanoparticles results in the formation of nanoparticulate Ag within the PEM that may retain the single-crystal structure. Above 400°C [105] the surrounding polymer matrix gradually decomposes, forming the crystalline Ag(N)/Ti-NBs nanocomposite.

With the subsequent annealing to 600°C the PEM is removed whereas Ag_2O nanoparticles convert to metallic Ag. The subsequent gradual removal of the polyelectrolyte above 350°C prevents agglomeration of the as formed Ag nanoparticles. As a result after annealing no obvious difference in the particle size was observed. After the annealing of the Ag_2O(N)/Ti-NBs-PEM at 600°C in air inorganic composites of Ag(N)/Ti-NBs were formed. After annealing, a uniform distribution of Ag nanoparticles over the Ti-NBs surfaces was obtained, as shown Figure 32.

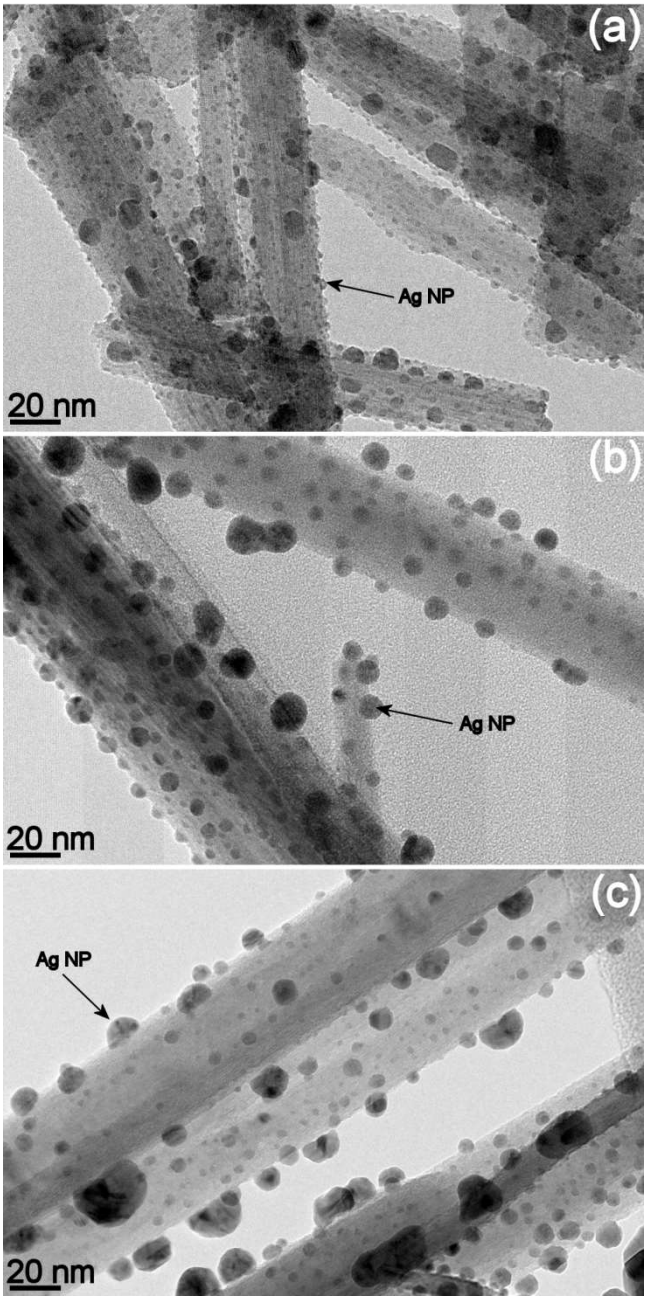

Figure 32: Bright-filed TEM images of the composites (a) Ag(1)/Ti-NBs, (b) Ag(2)/Ti-NBs and (c) Ag(3)/Ti-NBs after annealing at 600°C.

A typical SAED pattern of such composites shown in Figure 33 indicates the coexistence of highly crystalline, cubic, Ag nanoparticles and the single-crystalline titanate phase. Beside the weak reflections of Ag nanoparticles the reflections corresponding to various Ti-NBs additionally render the SAED analysis of the observed samples difficult. In order to enhance the intensity of Ag reflections in the SAED pattern the SAED analysis was performed on several Ti-NBs covered with Ag nanoparticles. Additional spots of titanate structure in the SAED are assigned to the diffraction of the neighbouring Ti-NB. In order to minimize additional Ti-NBs reflections in the SAED pattern the SAED analysis was performed on the composite shown in Figure 32(c). The spots in the SAED pattern correspond to the reflections of the metallic Ag nanoparticles and the two nearly parallel Ti-NBs in upper part of Figure 32(c), solely.

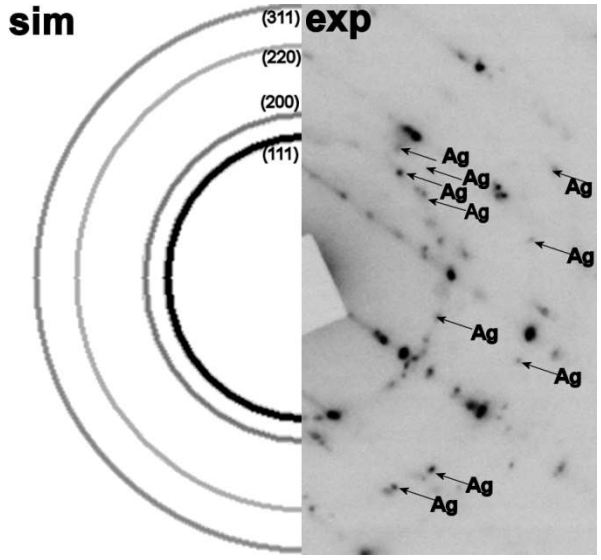

Figure 33: The experimental SAED pattern of the crystalline inorganic composite Ag(3)/Ti-NBs shown in figure 6(c) and simulated SAED pattern of cubic Ag.

The decrease in BET surface area was obtained in composite Ag(N)/Ti-NBs as compare to pure Ti-NBs. The BET surfaces of 20.5 m^2/g, 22.3 m^2/g and 23.4 m^2/g were measured for Ag(1)/Ti-NBs, Ag(2)/Ti-NBs and Ag(3)/Ti-NBs, respectively. The size of the Ag nanoparticles in the composite Ag(N)/Ti-NBs was evaluated based on TEM images. Average diameters of 4.5±2.1 nm, 7.9±3.1 nm and 9.6±4.2 nm were measured for the Ag nanoparticles in the composites Ag(N)/Ti-NBs formed by one, two and three ion-loading/reduction cycles in the PEM, respectively. Simultaneously, the densities of the Ag nanoparticles on the surface of the Ti-NBs decrease to $4.7*10^4/\mu m^2$, $0.9*10^4/\mu m^2$ and $0.2*10^4/\mu m^2$ (Table 3). In contrast to the composite Ag/Ti-NBs prepared with a commonly used ion-exchange/precipitation method where Ag nanoparticles with average size between 10 and 40 nm were obtained [96, 97], with the in-situ synthesis approach in PEM, Ag nanoparticles with size below 10 nm were formed on the surface of Ti-NBs.

Table 3: Size and density of Ag nanoparticles in Ag(N)/Ti-NBs nanocomposites.

Number of reaction cycles	Ag nanoparticle size (nm)	Ag nanoparticle density ($*10^4\ \mu m^{-2}$)
n=1	4.5±2.1	4.7
n=2	7.9±3.1	0.9
n=3	9.6±4.2	0.2

The decrease in Ag nanoparticle density after annealing indicates particle growth as the PEM matrix is removed during the thermal treatment. Ag nanoparticles formed on the surface of the Ag(N)/Ti-NBs appear to be composed of differently oriented smaller units, as can be seen from Figure 34. Such a polycrystalline structure of the Ag nanoparticles in composite Ag(N)/Ti-NBs suggests that after annealing, more primary particles of different orientations tend to form larger Ag clusters. With the annealing, thermal decomposition of the Ag_2O particles in the PEM may yield single-crystal, metallic Ag nanoparticles, whereas gradual removal of the surrounding polymer results in the

aggregation of the adjacent particles. Without steric stabilization of the particle surface, which is ensured by the PEM, due to their high surface energy, primary particles tend to form larger clusters on the surface of the Ti-NBs by a random-aggregation mechanism. The coalescence of primary Ag nanoparticles is more pronounced at a high particle density, which results in a larger increment of the Ag particle size formed by one ion-loading/precipitation cycle in the PEM (Table 3). After coalescence, spherical Ag nanoparticle clusters were obtained (Figure 34). These rounded particles exhibited a smaller number of surface atoms and thus a lower energy. As the annealing temperature exceeds 500°C, due to the thermodynamic constraints, irregular-shaped nanoparticles may convert to rounded particles [106]. Thus, during the annealing to 600°C, due to surface diffusion, spherical Ag nanoparticles were formed on the surface of the Ti-NBs.

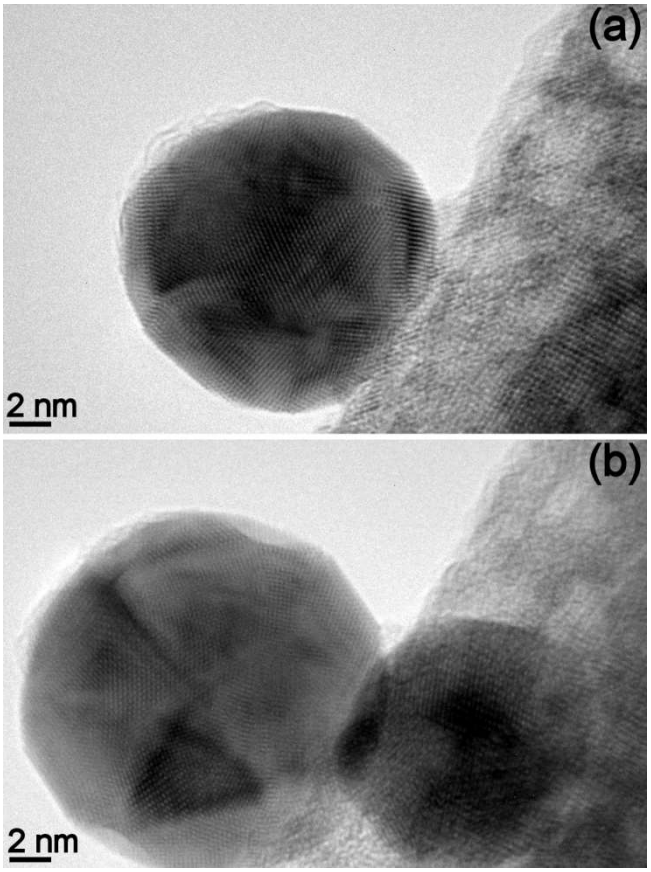

Figure 34: HRTEM images of nanosized Ag crystals on the Ti-NBs surface formed by (a) one and (b) three Ag loading cycles.

4.3.1.2 Optical properties and photocatalytic activity of Ag/Ti-NBs composites

Within the field of photoelectrochemistry/photocatalysis the figure of merit of the composite's performance is its electrical or optical response. The control over optical response of semiconductor is obtained by its bandgap energy, which represents a threshold energy for electron to be transferred from the highest occupied state i.e. in valence band to the lowest unoccupied state in conduction band. The charge separation is obtained upon irradiation of the semiconductor of the energy equal or greater than the energy of material's bandgap. While most of the charge undergoes recombination, a fraction of photogenerated electrons reaches the surface and participates in the surface redox reactions. Since the modification of the density of states (DOS) of electrons is strongly related to the dimensional confinement, the optical and redox properties (and electrical) of the semiconductor can be efficiently tailored by the variation of its physical dimensions i.e. size and morphology. In general, charge carriers in semiconductor experience confinement of motion in one, two or three spatial dimensions as one or more dimensions of the nanostructure are in the nanoregime. For the 1D nanostructures the electrons are confined in two dimensions and the transport is possible only in the direction along the axis of the nanostructure. The transition to 1D nanostructures is reflected in the divergence of the DOS of each sub-band at the band edge giving rise to van Hove singularities. Van Hove singularities in the energy DOS of carbon nanotubes result in modification of their optical properties, while the bandgap energy is increased with decreasing diameter of the tubes. However, optical absorption and photoluminescence of titanate-based nanotubes are not influenced by their diameter or morphology, since very small variations in bandgap energy with decreasing diameter were obtained. [107, 108] The conduction of semiconductor with a noble metal which serves as a sink for photo-generated electrons and promotes interfacial charge separation represents successful route toward suppressing the charge recombination rate and the maximization of the efficiency of photocatalytic reactions.

The absorption spectra of pure Ti-NBs and the composite Ag(N)/Ti-NBs are shown in Figure 35. The spectra show an absorption edge in the UV regime at about 250 nm for the pure Ti-NBs and for the composites. The absorption in the UV region is in all cases assigned to bandgap transition of the semiconductor. For the composites the absorption maxima obtained at energy corresponding to the UV region is followed by an absorption peak in the visible region at 410 nm. While the absorption in the UV regime is assigned to the band to band transitions of the semiconductive Ti-NBs, the visible-regime absorption maxima is induced by the local surface plasmon resonance (LSPR) of the Ag nanoparticles on the surface of the Ti-NBs. With an increase in the Ag nanoparticle density on the surface of the Ti-NBs a higher intensity of the LSPR absorption band was obtained. The photons that interact with the metallic nanoparticles induce an oscillation in the metal's conduction-electron charge density, which results in a localized, surface plasmon, resonance absorption (LSPR) band in the visible regime of the electromagnetic spectrum [109]. For the metallic nanostructure attached to a dielectric, the bandwidth, the position and the intensity of the LSPR are mostly affected by the density, the shape and the dielectric properties of the surrounding metallic nanoparticles [93, 110]. The existence of the single absorption band confirms the observations from the TEM images that the Ag nanoparticles in Ag(N)/Ti-NBs are essentially spherical. Since based on Mie theory [111], the LSPR is independent of the particle size for particle diameters that are much smaller than the incident wavelength, it appears that increase in the LSPR intensity could be mainly caused by a larger concentration of Ag nanoparticles in the Ag(N)/Ti-NBs composite as the number of Ag loading cycles is decreased.

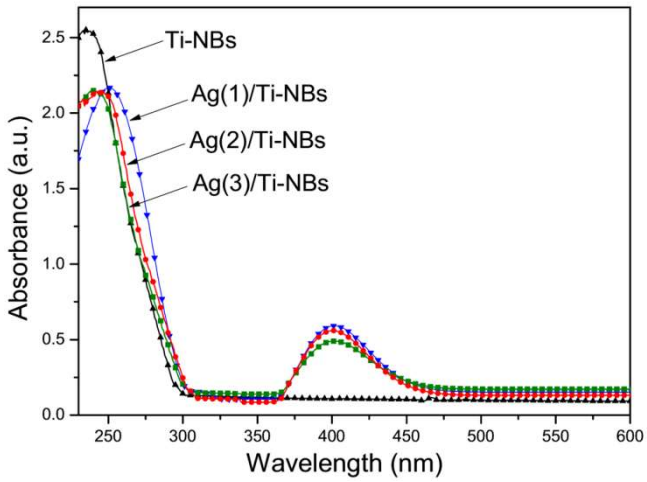

Figure 35: The UV-visible absorption spectra of crystalline pure Ti-NBs, Ag(1)/Ti-NBs, Ag(2)/Ti-NBs, and Ag(3)/Ti-NBs composites.

According to the differences of the absorption properties of pure Ti-NBs and Ag(N)/Ti-NBs these nanostructures are expected to exhibit different photocatalytic activities when exposed to UV- and visible-light irradiation. Since characteristic absorption peak of the pure Ti-NBs is in UV region it is expected that the photocatalytic efficiency of the composites in comparison to the pure Ti-NBs will be enhanced due to the expected change of the electron transport modified by the presence of metallic component building the composite. It is well established that conduction band electrons (e_{CB}^-) and valence band holes (h_{VB}^+) are generated as the semiconductor is irradiated with a light of energy greater than its band gap (Equation 26). The electrons from the semiconductor conduction band are transferred to the metallic Ag as the two particles undergo charge equilibration (Equation 27).

$$TiO_2 + h\upsilon(UV) \rightarrow TiO_2(e_{CB} + h_{VB}) \quad (3)$$
$$TiO_2(e) + Ag \rightarrow TiO_2 \cdots Ag \quad (4)$$

Relevant reactions induced by UV-light charge separation at the semiconductor-metal surface causing the degradation of dyes can be expressed by following reactions:

$$TiO_2(h_{VB}^+) + H_2O_{ads} \rightarrow TiO_2 + H^+ + OH^{\cdot} \quad (5)$$
$$TiO_2(h_{VB}^+) + OH_{ads}^- \rightarrow TiO_2 + OH^{\cdot} \quad (6)$$
$$TiO_2(e_{CB}^-) + O_{2ads} \rightarrow TiO_2 + O_2^{\cdot -} \quad (7)$$
$$TiO_2 - Ag(e) + O_{2ads} \rightarrow TiO_2 \cdots Ag + O_2^{\cdot -} \quad (8)$$
$$Dye + OH^{\cdot} \rightarrow degradation\ products \quad (9)$$
$$Dye + O_2^{\cdot -} \rightarrow degradation\ products \quad (10)$$

The photocatalytic activities of the Ti-NBs and Ag(N)/Ti-NBs measured under the UV-light by the degradation of the MB, as a model reaction, are shown in Figure 36. The Langmuir-Hinshelwood kinetics has been used to describe the reaction rate for heterogeneous photocatalysis [112, 113] of Ti-NBs where more adsorbents participate in the reaction. According to this model, the reaction rate for second-order surface decomposition of MB dye is:

$$-\frac{d[C]}{dt} = k\frac{K_e C}{1+K_e[C_0]} \tag{11}$$

where K_e is the equilibrium adsorption constant of MB, k is the second-order reaction rate of MB degradation, C is the concentration of MB after time t and C_0 is the initial concentration of the MB solution.

Based on Equation (11) the photocatalytic degradation of MB (low C_0) in the presence of Ti-NBs exhibits pseudo first order with respect to the concentration of dye:

$$-\frac{d[C]}{dt} = K_{obs}[C] \tag{12}$$

where K_{obs} is the pseudo first order reaction constant for the photocatalytic oxidation of MB dye. The integration of Equation (12) results in:

$$ln\left(\frac{C_0}{C}\right) = K_{obs}t \tag{13}$$

where the slope K_{obs} is the apparent reaction rate.

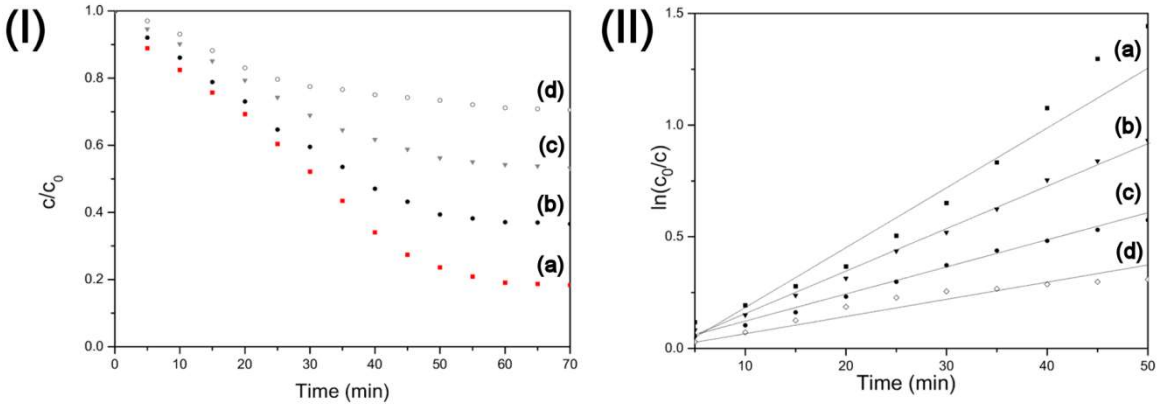

Figure 36: (I) The concentration profile and (II) the pseudo-first-order kinetic rate plot for the photocatalytic degradation of MB for (a) Ag(1)/Ti-NBs, (b) Ag(2)/Ti-NBs, (c) Ag(3)/Ti-NBs and (d) pure Ti-NBs under UV-light irradiation.

Based on the pseudo-first-order reaction, the UV degradation reaction rates were calculated to be 0.008/min, 0.011/min, 0.019/min and 0.027/min for the pure Ti-NBs, Ag(3)/Ti-NBs, Ag(2)/Ti-NBs and Ag(1)/Ti-NBs, respectively (Table 4). Compared to pure Ti-NBs, 3.4 and 1.4 times larger photo-degradation rates were obtained for 1 and 3 Ag loading cycles. It was shown previously that the photo-catalytic activity of the nanostructured titanates is strongly influenced by their crystallinity and morphology [8, 114, 115]. Due to their high specific area these nanostructures exhibit photo-catalytic activity in the UV regime [8, 19, 116]. However with the attachment of Ag nanoparticles to the surface of the Ti-NBs, enhanced photo-activity is obtained. The highest UV photocatalytic activity was observed in the composite formed with a single Ag nanoparticle loading cycle. In the titanate-metal nanocomposites, the electron transfer from the excited semiconductor to the metallic (Ag) nanoparticle at the interface is thermodynamically favourable because the Fermi level of the metal is lower than that of the Ti-NBs resulting in large potential difference between the conduction band of the semiconductor and the Fermi level of the metal facilitating electron accumulation in the metal. As a result of electron accumulation, the Fermi level of the Ag shifts towards the

conduction band of the semiconductor until an equilibrium between the semiconductor and the metal is attained. Due to the more negative potential of the as-formed composite Ag(N)/Ti-NBs a greater reductive power of the composite system is achieved [92, 117]. By increasing the Ag nanoparticle loading cycles, reduced photocatalytic activities were obtained for the as-formed Ag(N)/Ti-NBs. Since after a single Ag nanoparticle loading cycle the largest density of the smallest Ag nanoparticles on Ti-NBs was obtained, an increased metal-semiconductor contact area enables better electron transfer from the Ti-NBs to the Ag nanoparticles. Due to the discrete energy levels of the Ag nanoparticles, in smaller-sized Ag nanoparticles, a greater negative shift in the Fermi level for each accumulated electron is expected [117]. This better charge separation may result in an enhanced photocatalytic efficiency of the composite Ag(N)/Ti-NBs formed with fewer Ag loading cycles.

In Figure 37 the photocatalytic activity of the Ti-NBs and the composite Ag(N)/Ti-NBs in the visible region is shown.

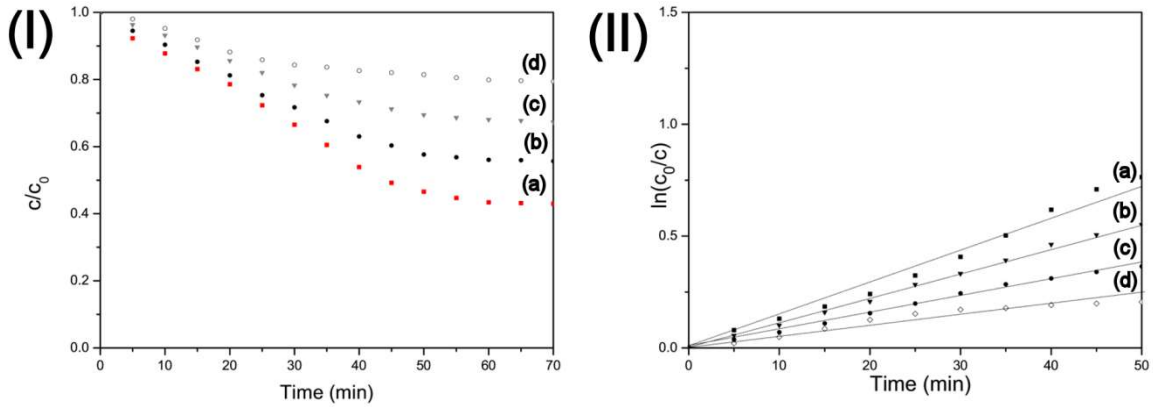

Figure 37: (I) The concentration profile and (II) the pseudo-first-order kinetic rate plot for the photocatalytic degradation of MB in (a) Ag(1)/Ti-NBs, (b) Ag(2)/Ti-NBs, (c) Ag(3)/Ti-NBs, and (d) pure Ti-NBs under visible-light irradiation.

Compared to the photo-activity in the UV regime, in the visible region, Ti-NBs and Ag(N)/Ti-NBs exhibit lower degradation reaction rates (Table 4). Since no absorption of pure Ti-NBs was observed in the visible spectrum, a degradation of MB in the presence of Ti-NBs can be assigned to the self-photosensitization of MB under visible-light irradiation. Under visible irradiation, the MB is transferred into its excited state. Then, due to the suitable energy-level positions between the MB and the Ti-NBs the excited dye may inject an electron into the conduction band of the Ti-NBs [118]. In this process, the MB is converted into a cationic radical, while the electron at the semiconductor surface reacts with adsorbed oxidants to produce oxygen radicals. An efficient charge separation of the injected electron and the cationic MB radical, which acts as a hole, may yield the photocatalytic activity of pure Ti-NBs under visible-light irradiation.

Table 4: UV and visible degradation-rate constants k (min^{-1}) for the Ti-NBs and Ag(N)/Ti-NBs nanocomposites.

Sample	k (min^{-1}) UV degradation	k (min^{-1}) visible degradation
Ti-NBs	0.008	0.005
Ag(1)/Ti-NBs	0.027	0.014
Ag(2)/Ti-NBs	0.019	0.011
Ag(3)/Ti-NBs	0.011	0.008

For Ag(N)/Ti-NBs an enhanced photocatalytic activity was observed in comparison to pure Ti-NBs under visible-light irradiation. As in the UV irradiation, the highest photocatalytic activity was obtained for the case of the Ag(1)/Ti-NBs. The visible photoactivity of the Ag(N)/Ti-NBs can be induced by the LSPR of the Ag nanoparticles [94, 95]. With the Ag nanoparticle-semiconductor contact at their interface, Schottky barrier banding may occur. Due to the LSPR of the Ag nanoparticles in the near-UV region, the photo-excitation can induce charge separation by the subsequent transport of the electrons from the Ag to the conduction band of the Ti-NBs. In the absorption spectra (Figure 35) the interactions between the Ag and the Ti-NBs are reflected in the red-shift of the absorption edge of the Ti-NBs. A more pronounced shift was observed with increasing densities of Ag nanoparticles on the Ti-NBs surface. A more intense LSPR band and enhanced interactions between the metallic Ag and the Ti-NBs in the composite with a larger Ag nanoparticle density yield a stronger transfer of the electrons from the Ag nanoparticles to the conduction band of Ti-NBs, which can explain the enhanced photo-reactivity of the composite Ag(N)/Ti-NBs under visible-light irradiation as the number of Ag loading cycles is decreased.

In addition, after a longer irradiation period the photocatalytic activity of the Ag(N)/Ti-NBs in the visible regime can also be induced by narrowing the band gap of the semiconductor by introducing impurity states within the band of the Ti-NBs. The presence of metal-ion dopants in the titanate matrix directly affects its photoreactivity, the charge-carrier recombination rates and the interfacial charge-transfer rates [119, 120]. In the metal-semiconductor composite, due to their redox potential level, a hole and/or OH radical thermodynamically favours the oxidation of metals. The possibility that metal nanoparticles might undergo a chemical transformation during UV-vis light exposure is especially pronounced for the nanosized domain and unprotected surface of the metallic particles [121]. The Ag ions generated at the interface of the Ag nanoparticle and Ti-NBs may then get intercalated into the titanate-lattice, which increases the photocatalytic activity of the composite Ag(N)/Ti-NBs in the visible region.

4.3.2 Cu/Ti-NBs composites

With increased demand for preventing the environment burdening with various pollutants, the biodegradation and other conventional methods, which produce secondary products and need additional post-treatments, the heterogeneous photocatalysis that in general includes semiconductor as a photocatalyst is expected to be adopted in such processes. Besides, TiO_2 as a most intensively investigated photocatalyst, the one-dimensional titanate nanostructures (titanate nanotubes-Ti-NTs and nanobelts-Ti-NBs) has been utilized as semiconductor component of metal-semiconductor nanocomposites that are expected to improve quantum efficiency of photocatalytic degradation of pollutants. In particular coupling of wide-bandgap semiconductive 1D titanate-based nanostructures with noble metal spherical nanoparticles, homogeneously distributed on the surface of

titanate nanostructures opens new possibilities for development of efficient photo-catalysts that may enhance photo-induced reactions under UV irradiation and simultaneously trigger the absorption of visible light. Among noble metals such are Au and Ag nanosized Cu has been increasingly investigated as it exhibit clear LSPR features in optical spectra located in visible region of light wavelengths. However, recently, compared to gold and silver, copper has received more attention due to its good photocatalytic activity and lower price of the source ions as well, which is of great importance due to the rising demands for more economic routes to the manufacturing of a long wavelength visible-light absorption catalysts. The absorption spectra of Cu nanoparticles dominated by higher order modes and severely damped dipolar surface plasmon resonance appears very different from those of Au and Ag. Unlike Ag, the surface plasmon resonance that is enhanced due to the higher order SP modes is a small feature in extinction spectrum of copper nanoparticles and scattering contribution to the overall extinction spectra is little. It is assumed that interband transitions dominantly contribute to the spectra by strong damping of the surface plasmon resonance. For the Cu nanoparticles mainly broadening of surface plasmon resonance that is related to the close proximity of the SPR (2.22 eV) energy to the quasi-particle interband continuum i.e. interband transition (2.17 eV) accompanied by the minor red shift was obtained.

The optical properties of metal particles of nanometer dimensions depend on concentration, size, crystallinity, morphology and crystal structure of the nanostructures. Various synthetic approaches for preparation of copper nanoparticles such as thermal and sonochemical reduction, UV irradiation, micro emulsion technique and chemical reduction of copper-based salts lack the control over the shape and particle size distribution and yield particles of the size in submicron and micron regimes. A versatile methodology for the formation of spherical, non-agglomerated nanosized particles with narrow size distribution has been achieved by a weak-polyelectrolyte assisted LbL method which in addition has been proven as an effective strategy toward controlled fabrication of Cu/Ti-NBs nanocomposites with high intercontact area between metallic and semiconductor component of as-synthesized composites.

4.3.2.1 Structural and morphological properties of Cu/Ti-NBs composites

First, for the formation of weak polyelectrolyte multilayer-PEM/Ti-NBs composite 6.5 bilayers of appositively charged weak-polyelectrolytes were assembled by LbL method on the hydrophilic surface of the hydrothermally synthesized crystalline Ti-NBs. In next step of a fabrication procedure, multilayered matrix comprised of polyelectrolytes forming a coating on the Ti-NBs (PEM/Ti-NBs composite) was subsequently utilized as a nanoreactor for the *in-situ* synthesis of metallic Cu nanoparticles as shown schematically in Figure 20. Figure 38 shows TEM images of as-formed nanostructures after sequential procedure steps.

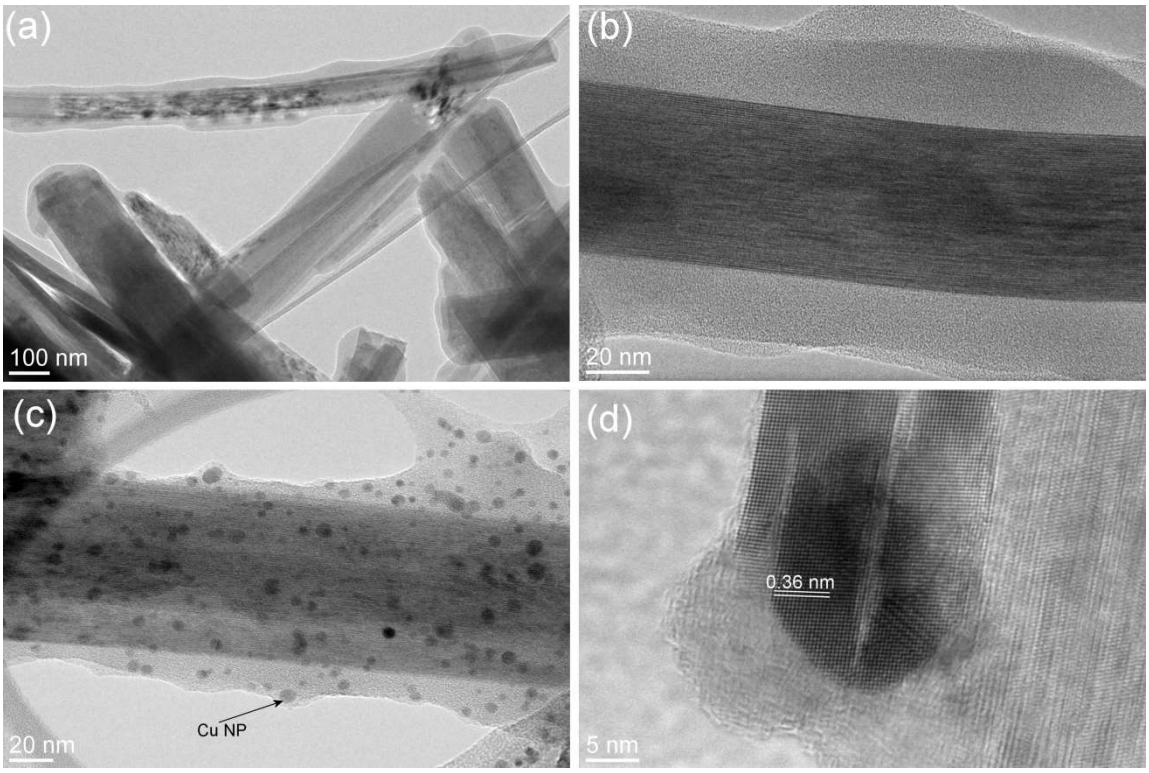

Figure 38: Bright-field TEM images of precursor (a) PEM/Ti-NBs, (b) PEM/Ti-NBs, (c) Cu loaded PEM/Ti-NBs and (d) HRTEM of Cu nanoparticle in PEM.

As the PEM/Ti-NBs composite was exposed to the Cu^{2+} ion aqueous solution at pH value higher than this during the PEM assembly process, Cu^{2+} bind to the free carboxylic groups of the PAA polyelectrolyte forming PEM. After chemical reduction of Cu^{2+} cations the surrounding polymeric matrix prevents agglomeration of proximate particles and constrains their growth, thus subsequently spherical Cu nanoparticles uniformly distributed within PEM film are obtained (Figure 38(c)). From the TEM images estimated average particle diameter was 4.8±1.2 nm, while the Cu nanoparticle density of $5.9*10^3$ μm^{-2} in PEM was obtained. In comparison to the Ag nanoparticle density obtained for the Ag/Ti-NBs composite after one loading cycle, the Cu particle density is lower, which, in contrast to the Ag^+ ion binding, is related to the consumption of two COO^- groups per one Cu^{2+} ion. The highest density of smallest Ag nanoparticles was achieved after one loading cycle, while the final Cu/Ti-NBs-PEM composite was obtained after single Cu ion-binding/reduction cycle. From the HRTEM investigation it was conducted that after reduction within PEM spherical nanoparticles are single crystalline cubic Cu nanoparticles (Figure 38(d)). In addition, coexistence of highly crystalline cubic Cu and titanate-based phases was confirmed by XRD analysis. The XRD patterns of PEM coated pure Ti-NBs and Cu-loaded Ti-NBs, respectively, are shown in Figure 39.

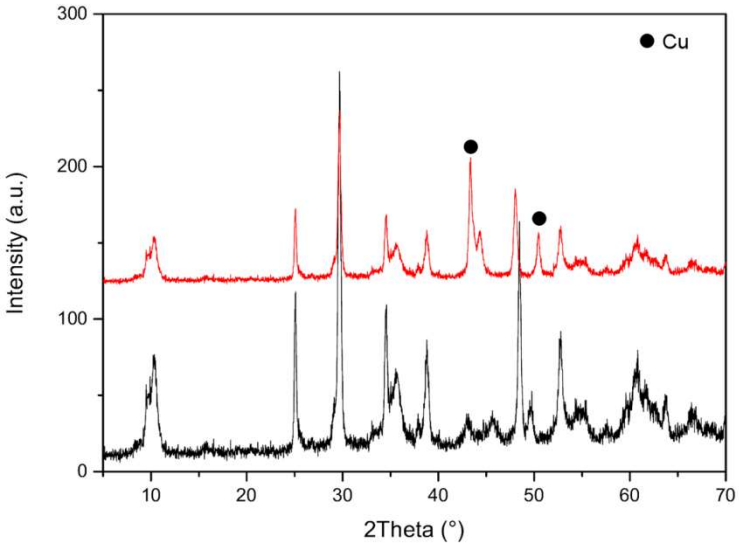

Figure 39: XRD pattern of PEM/Ti-NBs (black pattern) and Cu-loaded PEM/Ti-NBs (red pattern) composite structures.

For the fabrication of inorganic Cu/Ti-NBs one dimensional composite, the Cu/Ti-NBs-PEM composite was first annealed in air at 500°C to remove polymeric matrix and then subsequently exposed to the hydrogen atmosphere at ramping heating to 300°C. During annealing in air the decomposition of organic matrix is accompanied by the oxidation of metallic Cu nanoparticles. A typical SAED pattern (Figure 40(c)) of as-treated composites indicates formation of crystalline, monoclinic CuO nanoparticles on the surface of Ti-NBs. After annealing in air the CuO particles retain spherical morphology accompanied with a slight increment of the particle size, whereas the particle density and uniform distribution of nanoparticles attached to the surface of titanate nanobelts are preserved (Figure 40(a)).

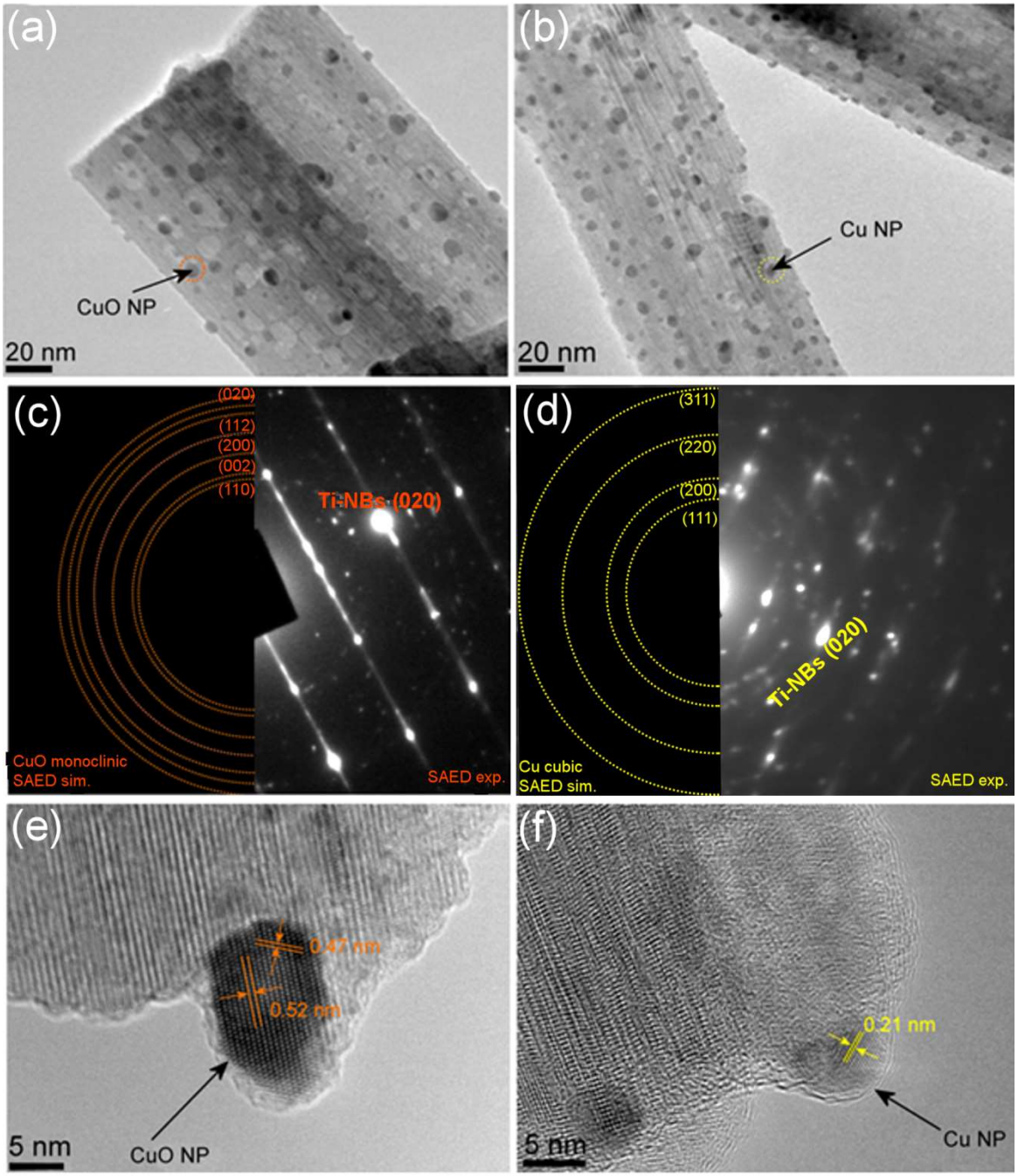

Figure 40: Bright-field TEM images of (a) CuO/Ti-NBs, (b Cu/Ti-NBs), (c) the simulated SAED pattern of monoclinic CuO and the experimental SAED pattern of the crystalline CuO/Ti-NBs, (d) the simulated and experimental SAED pattern of cubic Cu and Cu/Ti-NBs, respectively, (e) HRTEM of CuO nanoparticles attached to the Ti-NBs and (f) HRTEM of Cu nanoparticles of Cu/Ti-NBs composite.

With the subsequent annealing of the CuO/Ti-NBs composites in the presence of hydrogen atmosphere CuO nanoparticles were transformed to metallic Cu nanoparticles. The SAED pattern in Figure 40(d) confirms coexistence of cubic Cu nanoparticles and single crystalline Ti-NBs. The morphology, size and crystal structure of Ti-NBs are not affected by the exposure of these nanostructures to the hydrogen environment at elevated temperatures below 500°C. [122] Spherical Cu nanoparticles remain uniformly distributed through the surface of Ti-NBs. The average particle size is comprisable to the particle size of initially formed Cu nanoparticles within PEM in the third step of Cu/Ti-NBs composite fabrication procedure shown in Figure 20. In addition to the SAED

analyses of CuO- and Cu-loaded Ti-NBs composites the XRD patterns in Figure 41 indicate the formation of monoclinic CuO and cubic Cu particles on the surface of Ti-NBs formed during annealing in air and hydrogen atmosphere, respectively. In comparison to the specific surface area of pure Ti-NBs the attachment of Cu nanoparticles onto the surface of Ti-NBs yields a decrease in BET surface of the composite Cu/Ti-NBs. By the BET method measured specific surface area of the Cu/Ti-NBs composite was 23.7 m^2/g.

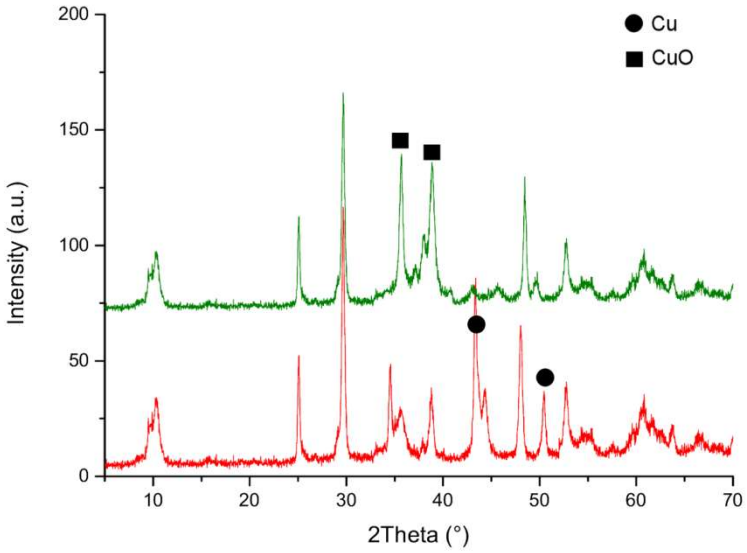

Figure 41: XRD pattern of Cu/Ti-NBs (red) and CuO/Ti-NBs (green) composite.

For the determination of valence states of Ti in the Cu/Ti-NBs composite the XPS analysis was employed. Figure 42 shows titanium $2p_{3/2}$ and $2p_{1/2}$ peaks building the XPS spectra of the pure Ti-NBs and Cu/Ti-NBs composite. The oxygen O 1s spectrum is decomposed to the two contributions, namely the main peak is followed by the shoulder shifted to higher energies. The main peak located at the binding energy of 530.6 eV is assigned to the Ti-O bond in the titania-based oxide Ti-NBs, while the second feature resolved at 531.8 eV corresponds to the existence of Ti-OH at the surface indicating hydrophilic nature of nanostructures' surface. The Ti $2p_{1/2}$ and Ti $2p_{3/2}$ spin-orbital splitting photoelectrons giving rise to the peaks in the XPS spectrum at binding energies of 464.5 eV and 459 eV, assigned to the titanium in its 4+ valence state.

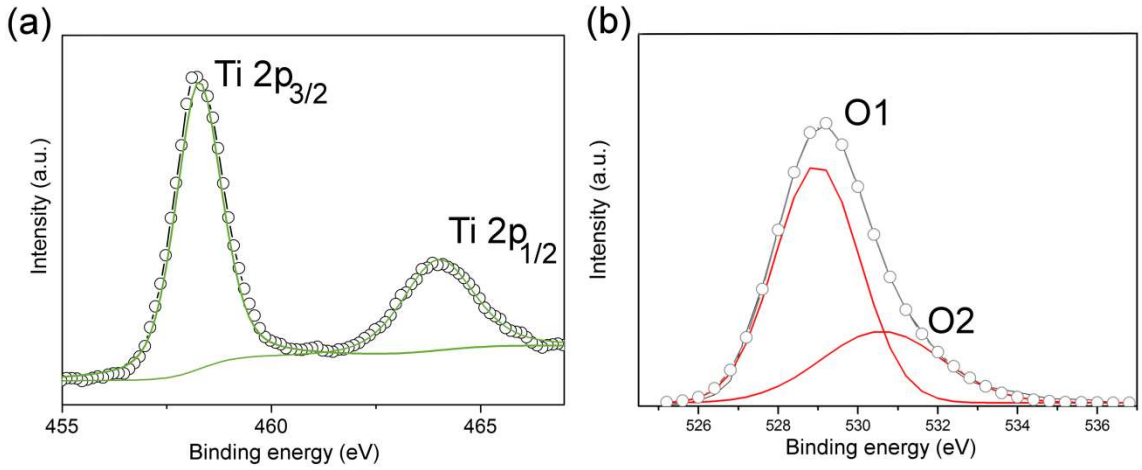

Figure 42: The XPS spectra of (a) Ti 2p and (b) O 1s of the nanostructured composite.

4.3.2.2 Optical properties and photocatalytic activity of Cu/Ti-NBs composites

Figure 43 shows the absorption characteristics of pure Ti-NBs and Cu/Ti-NBs nanocomposite.

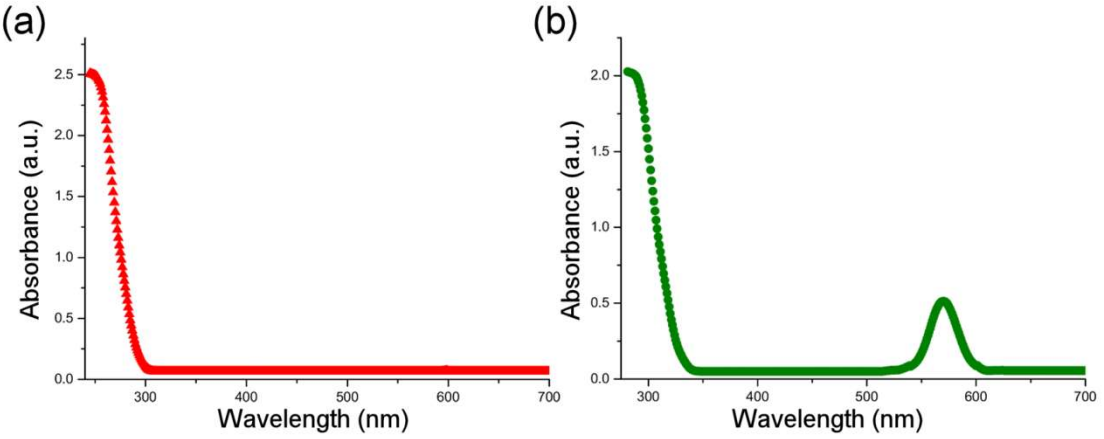

Figure 43: The absorption spectra of (a) pure Ti-NBs and (b) Cu/Ti-NBs nanocomposite.

The Ti-NBs absorption spectrum is characterized by a single absorption band in UV region of wavelengths located at about 250 nm, which is assigned to the band-gap transitions of the Ti-NBs. For the Cu/Ti-NBs composite spectrum absorption edge of the Ti-NBs located in the UV regime is followed by an additional band located at higher (visible) wavelengths. This visible absorption maximum at 573 nm is induced by the local surface plasmon resonance (LSPR) of the Cu nanoparticles attached to the surface of Ti-NBs. As the average size of the metallic Cu nanoparticles attached to the semiconducting Ti-NBs is much smaller than the wavelength of the exciting light, the bandwidth, the position and the intensity of the LSPR is highly affected by the shape and size of metallic nanoparticles. The rise of a single absorption band related to the LSPR of the Cu nanoparticles is in agreement with the TEM observations that the Cu nanoparticles attached to the surface of Ti-NBs are essentially spherical. However, for the nanoparticles much smaller than the wavelength of incident light the LSPR is independent of the particle size, thus the increase in the LSPR intensity may be manipulated by increased dielectric constant of the composite induced by a larger concentration of Cu

nanoparticles.

As the Ti-NBs and Cu/Ti-NBs nanocomposite are introduced as photo-catalysts into the degradation process of organic dye Methylene Blue (MB) based on absorption characteristics of both materials, the composite is expected to exhibit different photo-response in the UV-vis regime of interest as compared to the Ti-NBs. Figure 44 shows the photocatalytic properties of pure Ti-NBs and Cu/Ti-NB multilayered films under UV and visible irradiation.

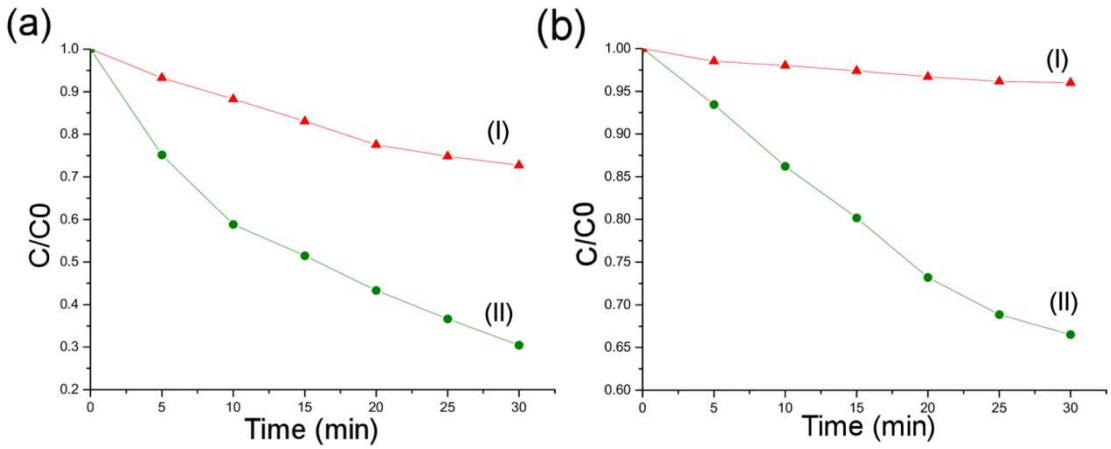

Figure 44: (a) The concentration profiles for the photocatalytic degradation of MB for (I)Ti-NBs and (II) Cu/Ti-NBs under UV irradiation and (b) the concentration profiles for the degradation of dye under visible irradiation for (I) Ti-NBs and (II) Cu/Ti-NBs.

Based on the linear relationship of $ln\frac{C_0}{C}$ vs. time, photocatalytic degradation reaction follows the pseudo-first-order kinetics. Pseudo first order reaction rates in the UV regime were calculated for this experiment to be 0.012/min for the Ti-NBs, and 0.037/min for the Cu/Ti-NBs hybrid material, respectively. The elongated morphology of 1D Ti-NBs hinders the ability of exciton recombination which resulted in enhanced photo-activity of 1D Ti-NBs under UV radiation. The additional increase in the photo-catalytic activity was obtained for Cu nanoparticles attached to the surface of Ti-NBs. Based on the UV absorption characteristics, Cu/Ti-NBs composite exhibited highest photocatalytic activity compared to Ti-NBs as they were exposed to the UV radiation. With a high inter-contact of Cu nanoparticles and Ti-NBs in the Cu/Ti-NB composite, the transfer of the photo-generated electrons from the excited Ti-NB to the metallic Cu nanoparticle at the interface is thermo-dynamically favourable due to lower position of the copper Fermi level in comparison to that of the Ti-NBs. Due to the subsequent electron accumulation in Cu nanoparticles the Fermi level of the Cu shifts closer to the conduction band of the semiconductor Ti-NBs until the two systems attain equilibrium, resulting in a more negative potential of the Fermi level of the composite Cu/Ti-NB nanostructures, which result in enhanced reductive power. [117] Scheme of corresponding interactions of Cu/Ti-NBs composite with UV and visible irradiation is shown in Figure 45. A favourable more positive potential of the metallic Cu Fermi level may increase the efficiency of electron transfer from the Ti-NBs to the Cu nanoparticles. In addition, increased concentration of superoxide anion radicals O^{2-} on the surface of Cu/Ti-NBs induced by the hydrogen treatment enables stabilization of hydroxyl radicals, hence preventing mediated exciton recombination as follows: [123]

$$O_2 + e^- \rightarrow O^{2-}(super\ oxide\ radical\ ion) \quad (28)$$
$$H_2O/OH^- + h^+ \rightarrow \cdot OH(hydroxyl\ radical) \quad (29)$$
$$\cdot OH + e^- \rightarrow OH^-(inhibited\ hydroxyl\ radical) \quad (30)$$

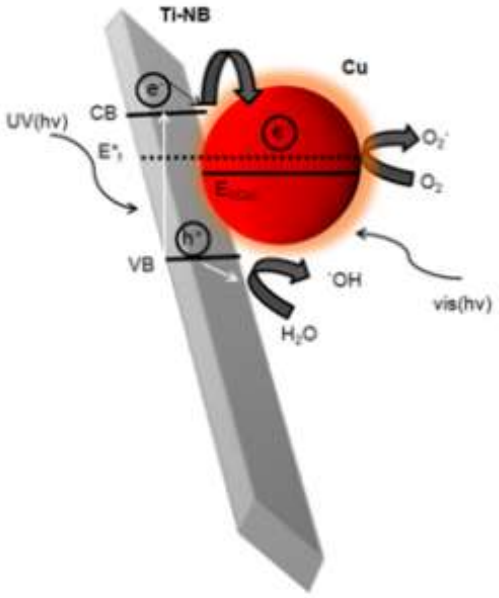

Figure 45: Stepwise electron transfer from Ti-NBs to metallic Cu nanoparticle following excitation of the Ti-NBs with the corresponding Fermi-level equilibration in a metal - semiconductor nanocomposite system.

In comparison to the photo-degradation in UV, under visible light irradiation the pure Ti-NBs and Ti-NBs-based nanocomposite exhibit lower degradation reaction rates. As conducted from the Figure 44(b). Pseudo-first order reaction rates in the visible regime were calculated to be 0.0012/min and 0.015/min for the Ti-NBs and Cu/Ti-NBs composite, respectively.

Although the Ti-NBs showed negligible absorption in the visible regime, they exhibit some photo-catalytic activity for the degradation of MB in the visible region (Figure 44(b) (I)) which may be assigned to the self-photosensitization of MB under visible-light irradiation. Due to the suitable energy level positions between the MB and the semiconductor, upon visible light irradiation, the excitation of MB may be agitated enabling the injection of an electron to the conduction band of the Ti-NBs. [118] As a result an efficient charge separation of the injected electron and the cationic MB, induce the photocatalytic activity of the pure Ti-NBs under the visible-light irradiation. The increase in the photocatalytic activity observed for the Cu/Ti-NBs composite under visible-light irradiation as compared to Ti-NBs is a result of the metallic nanoparticle LSPR mediated photoexcitation of the neighbouring semiconducting nanostructure as it was shown for Ag/Ti-NBs composite also[124]. Under visible light excitation, the LSPR induces a near electromagnetic field in the vicinity of the Cu nanoparticle. A high inter-contact area and increased concentration of Cu nanoparticles on the surface of Ti-NBs

induces more intense LSPR, thus the near field yields in photo-excitation of the semiconductor resulting in enhanced photocatalytic efficiency of the Cu/Ti-NBs composite under visible light irradiation.

4.4 Thin films

Recently, many investigations are focused on the issue of recovery and separation of photo-catalysts after the photo-induced processes from the treated waste waters. In particular, their utilization in large scale or industrial processes is strongly hindered since the removal of photo-catalytically active materials is closely related to the costs of separation processes. One of the proposed strategies for resolving these problems is fabrication of magnetic hybrid nanostructured photo-catalysts which may be removed after the reaction by applying external magnetic field. [125] However, pretentious synthesis, photo-dissolution of the magnetic component, formation of undesirable components, etc. hinder successful utilization of this approach. On the other hand deposition of photo-sensitive material on the substrates that are compatible with photo-catalytic material and are transparent to the light offers an effective strategy for fabrication of photo-active materials in form that is not difficult to handle.

In order to develop novel and efficient nanostructured photo-catalysts the layer by layer film assembly approach and the recent achievements of weak polyelectrolyte-assisted nanoparticle loading onto the surface of titanate nanobelts were combined and utilized for the fabrication of photo-active nanostructures in 3D configuration, which would enable low photocatalyst's separation and recycling costs after photo-induced treatment of polluted systems, and will be easy to handle.

Recently, electrostatic layer by layer (LbL) assembly technique has been utilized for the fabrication of multilayered films where various inorganic nanostructures such as multiwall nanotubes (MWNT), TiO_2 and SiO_2 nanoparticles, have been assembled with polymers for the thin film fabrication with thickness control in the nanometer scale. [126, 127, 128, 129] Assembling of dispersed nanostructures onto various substrates using LbL assembly approach, which consist of the repeated, sequential deposition of complementary functionalized species is schematically shown in Figure 46.

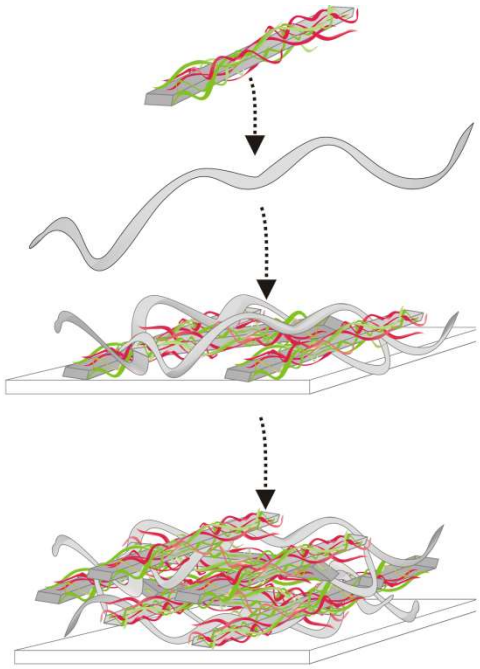

Figure 46: Scheme of thin film fabrication on a wafer by Layer-by-Layer assembly of PEM functionalized 1D nanostructures and appositively charged polyelectrolyte.

Polyelectrolyte assisted LbL synthesis was used for the construction of 3D network structures composed of Ti-NBs. By this synthetic procedure the thickness of fabricated films is tuneable by varying the number of repeated, sequential deposition steps. In Figure 48 (a), (b) SEM top view images of the multilayer films formed of 10 and 20 layers of Ti-NBs show random arrangement of individual Ti-NBs in the network structures. The film thicknesses determined from the cross-sectional FE-SEM images in Figure 48 (c), (d) of the multilayered nanostructured films reveal increment of the film thickness as the number of deposited layers increases. Figure 47 shows linear increment of thickness of the multilayered films as the number of layers increases from 5 to 20. During electrostatic assembly of 10 and 20 bilayered films of PEM/Ti-NBs at pH value of 9 an average thicknesses of 1.8 µm and 3.9 µm were measured. This yield for as-assembled multilayer films an average thickness increment of about 180 nm per one PEM/Ti-NBs-PSS bilayer forming the multilayer assembly. With the layer-by-layer methodology the thickness of the formed multilayers film primarily depends on the charge density of the assembled species and is further controlled by the number of assembled layers. [130]

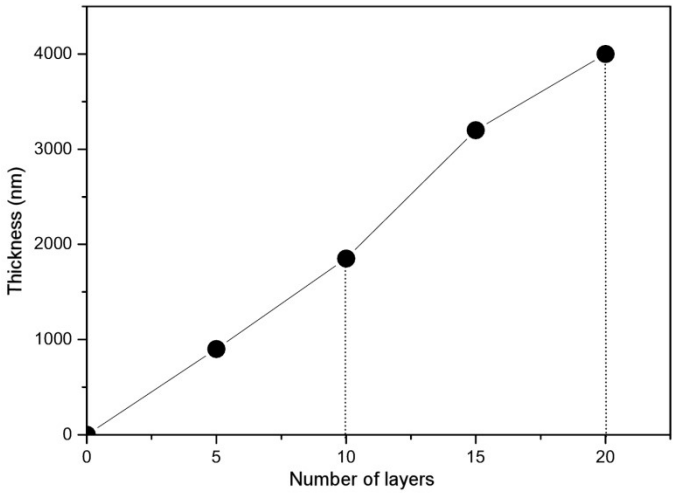

Figure 47: The thickness of the multilayered assembly vs. number of assembled layers of PEM/Ti-NBs fabricated by the layer by layer approach.

The cross-sectional FE-SEM images of 10 and 20 layered Ti-NBs films revealed that multilayered films formed by the layer by layer assembly yield orientation of Ti-NBs in the film, which is not parallel with the substrate (Figure 48 (c),(d)). This induces nanoscale porosity and yields high specific area of the as formed nanostructured films.

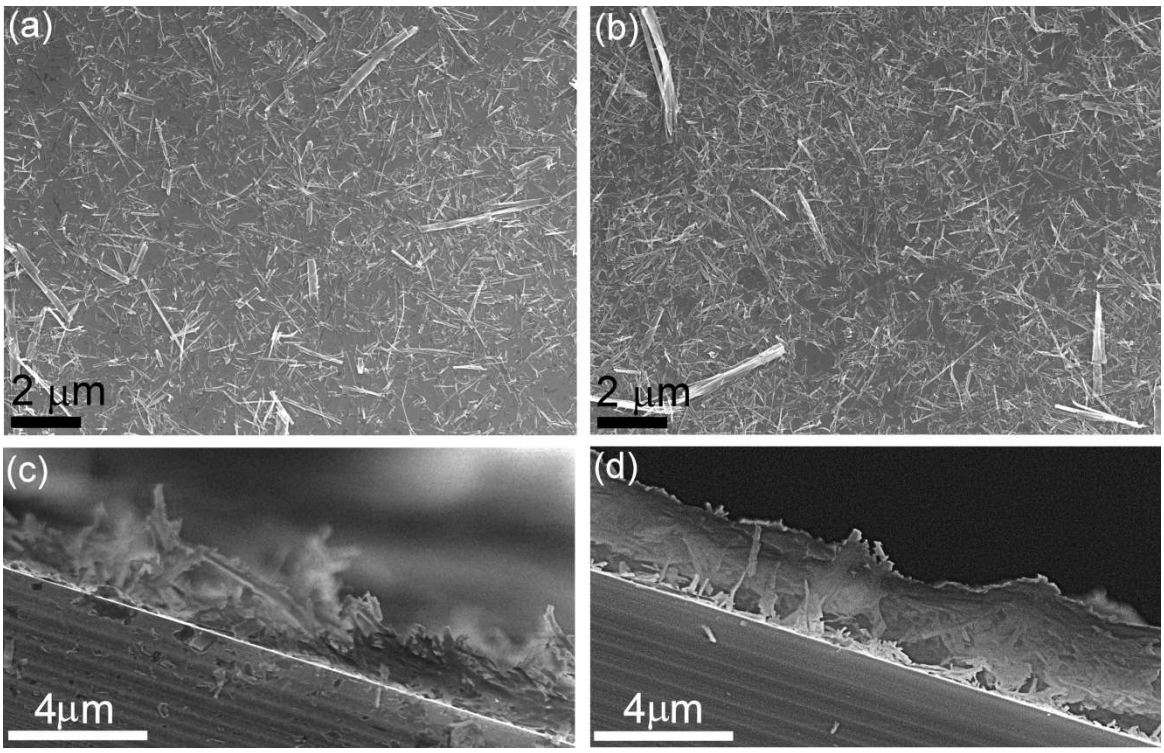

Figure 48: Comparison of the surface morphology and cross sections of nanostructured Ti-NB films formed of (a, c) 10 layers of Ti-NBs and (b, d) 20 layers of Ti-NBs.

After annealing in air at 500°C 10 and 20 layered Ti-NBs thin films possess interconnected network morphologies composed of separated individual Ti-NBs. According to the AFM measurements (Figure 49) the root-mean-square roughness

increased from 40 nm to 50 nm for the films assembled of 10 and 20 layers of Ti-NBs. The higher roughness may be explained by the higher thickness of the films and looser adsorption of the assembled Ti-NBs as number of layers is increased. [131]

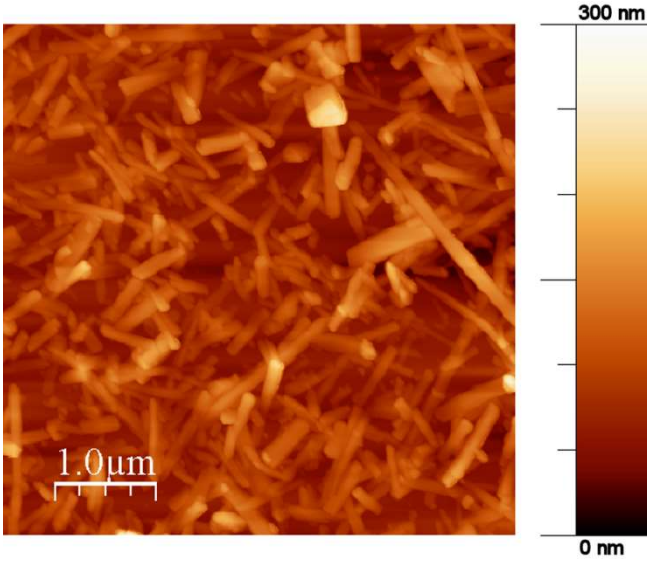

Figure 49: Atomic force microscopy images of nanostructured films formed of 10 layers of Ti-NBs after annealing in air at 500°C.

Nanoporosity of the multilayer films induced by the laterally random arrangement of individual Ti-NBs in the 3D structures yielding high specific area and hence enhanced adsorption capacity of the organic dye combined with the simultaneous increase in thickness and roughness of the films induced by the higher number of layers render these multilayered Ti-NBs films an efficient 3D building blocks for enhanced photocatalytic degradation of organic contaminants in water and air.

In addition, assembly of the multilayer nanoreactor onto the surface of 1D Ti-NBs provides the ability to control the size and density of the metallic (Ag, Cu) or semiconductive (CuO) component in a form of nanoparticles on the Ti-NBs surface resulting in greater inter-contact area between the two components in the as synthesized composite nanostructures. On the other hand the LbL approach provides a simple and versatile method to assemble wide range of nanostructures into thin films deposited on various substrates. By an association of advantages of both approaches a novel route for production of conformable thin films composed of various functionalized one-dimensional nanostructures is proposed as an efficient methodology for controlled design of the 3D multilayered structures as represented schematically in Figure 50.

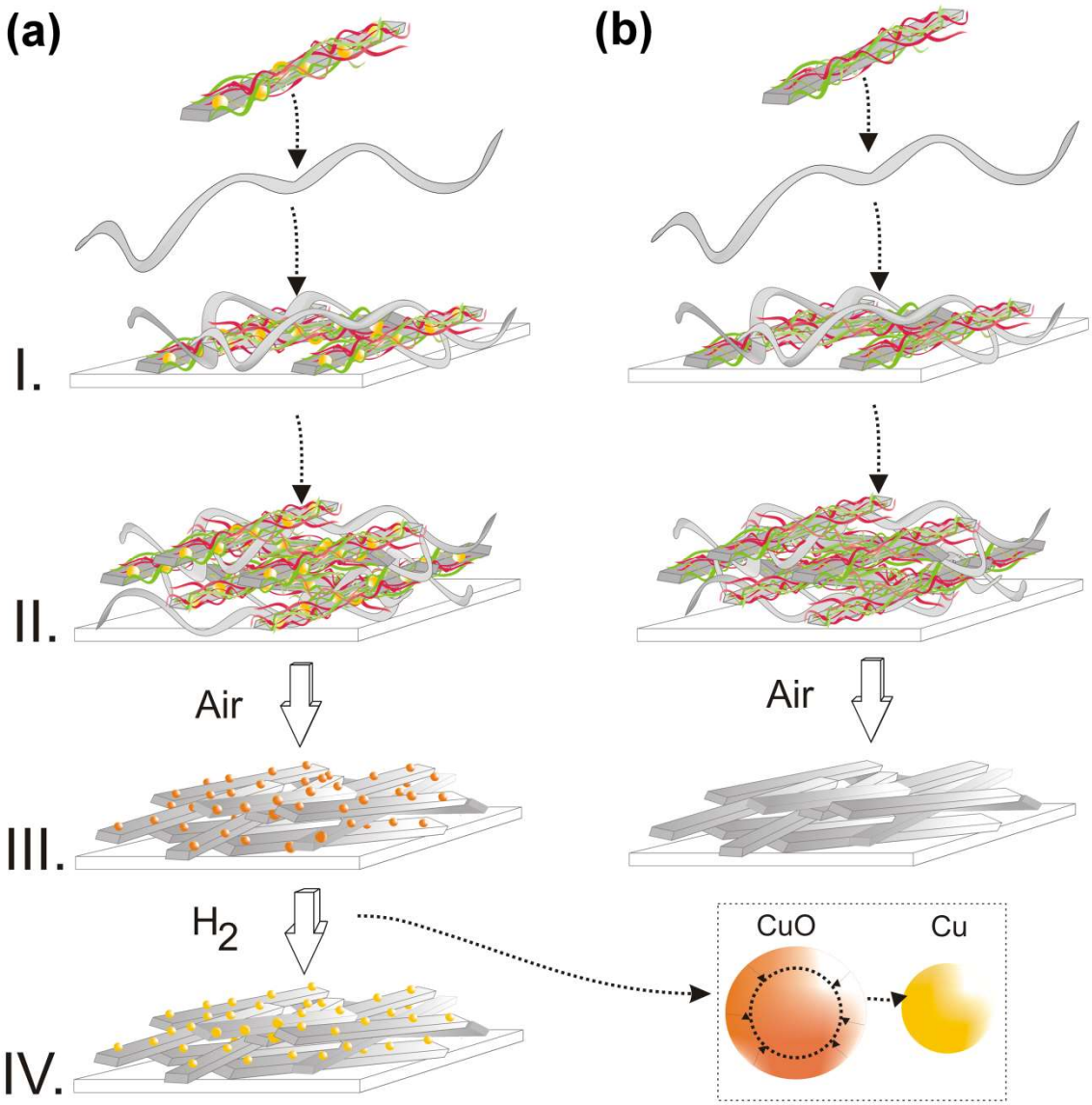

Figure 50: proposed fabrication methodology for (a) CuO-loaded Ti-NBs (step III.) and Cu-attached Ti-NBs (step IV.) and (b) pure Ti-NBs multilayered films with the LbL self-assembly of precursor structures.

5 Conclusions

This thesis has shown that 1D hydrothermally synthesized titanate based nanostructures present unique system for fabrication of multifunctional materials that exhibit enhanced properties rendering these nanostructures as active materials in various processes. With respect to their ion-exchange properties, highly hydrophilic surface, high specific surface area and semiconducting properties, titanate-based nanobelts and nanotubes have been studied in the field of heterogeneous catalytic processes, dye sensitized solar cells, rechargeable lithium batteries, and as materials for the photocatalytic degradation of organic compounds.

The tubular morphology and the dimensions of the Ti-NTs precursor were preserved and inherited by the calcium doped nanotubes (Ca/Ti-NTs) as the temperature of the hydrothermal reaction was increased up to 130°C. In the temperature range from 100°C to 130°C the maximum amount of incorporated calcium that corresponds to a Ca/Ti ratio of approximately 0.5 was achieved. Temperatures higher than 130°C led to the formation of nanosized single crystalline, well crystalline $CaTiO_3$ crystals. Irregular rectangular crystals with partially scrolled edges are joined in clusters. Individual $CaTiO_3$ crystals forming cluster grow in the [010] direction. Formation of nanocrystals with the edges curled perpendicular to the crystal growth direction indicates that the morphology of as-formed $CaTiO_3$ is partially affected by the precursor's tubular morphology. By the exploitation of their high ion-exchange ability, morphology and dimensionality, high specific surface area and semiconducting nature the one-dimensional titanate nanostructures were demonstrated as an affective system for fabrication of nanostructured perovskites and functionalised one-dimensional nanostructures as promising bioactive/biocompatible materials for implementation in biomedical applications.

For the fabrication of hybrid materials based on 1D titanate nanostructures a weak-polyelectrolyte multilayer assembled on a surface of Ti-NBs was successfully utilized as a nanoreactor for *in situ* Ag and Cu nanoparticles synthesis in the fabrication of Ag- or Cu-loaded Ti-NBs nanocomposites. With the *in-situ* synthesis approach in PEM, after annealing, aggregation growth has been observed between the neighbouring particles within the PEM. Nevertheless, the average particle size, controlled by the number of the reaction cycles, below 10 nm was observed. In addition with this approach uniform particle size and control of the Ag (Cu) nanoparticle density on the Ti-NBs surface was obtained by repeating the ion-loading/reduction cycle. Therefore, a small particle size results in large metal-semiconductor contact area and narrow particle size distribution that are important parameters for the envisioned applications of such metal-semiconductor composite nanostructures.

The metallic silver nanoparticles on a Ti-NBs surface can be obtained by the thermal reduction of Ag_2O nanoparticles formed by a reaction with hydroxyl groups detached from the surface of Ti-NBs. The density and size of Ag nanoparticles in the Ag/Ti-NBs composite was controlled by repeating the ion-loading/precipitation cycles. By realizing the ability to manipulate the size and density of the Ag nanoparticles on the Ti-NBs surface the metal–semiconductor interfacial area can be controlled.

The fusion of Ag or Cu nanoparticles and Ti-NBs resulted in an enhanced UV photo-efficiency as compared to photo response characteristic for pure, pristine hydrothermally

synthesized Ti-NBs. 3.4 times higher photo-induced degradation rate was obtained for the Ag/Ti-NBs nanocomposite of highest density of smallest Ag nanoparticles on the surface of Ti-NBs, while in the case of Cu/Ti-NBs composite 3.1 times higher degradation rate was determined. The as formed Ag/Ti-NBs and Cu/Ti-NBs composites also exhibited visible photoactivity assisted by the near-field amplitudes of the localized surface plasmon resonance (LSPR) of Ag and Cu nanoparticles in the 1D nanocomposite.

The synthesis route for the fabrication of 3D architectures formed of Ti-NBs was demonstrated. The PEM/Ti-NBs organic/inorganic composite was fabricated by layer-by-layer self-assembly of weak polyelectrolytes on the surface of Ti-NBs. As-functionalised titanate nanobelts (PEM-Ti-NBs) were assembled in sequential steps with strongly negatively charged polyelectrolyte Poly(styrenesulfonic acid) (PSS) to build film assemblies of various thicknesses on the substrate. The positive charge of PEM assembled on the negatively charged surface of Ti-NBs enables strong electrostatic coupling with negatively charged PSS yielding multilayered organic-inorganic film with linear film thickness increment as the number of layers in the multilayered film is increased. After annealing in air at 450°C the organic compounds are removed and inorganic film composed of individual randomly oriented Ti-NBs is obtained. The orientation of Ti-NBs in the film, which is not parallel to the substrate, induces nanoscale porosity resulting in higher specific area rendering these 3D architectures potentially efficient in photo-catalytic degradation of organic contaminants. Additionally by increasing the number of layers in Ti-NBs-based films higher adsorption capacity for the organic compounds was achieved, facilitating enhanced photo-catalytic efficiency.

This thesis has shown that with the *in-situ* precipitation and subsequent formation of metallic (Ag or Cu) nanoparticles in PEM nanoreactor assembled on the surface of Ti-NBs the control over the density, size and uniform distribution of inorganic nanoparticles in the hybrid structures is possible. Besides the surface reactions induced by the hydrophilic nature of Ti-NBs, intense electronic interactions between metallic nanoparticles and Ti-NBs control the exciton transfer and recombination dynamics resulting in enhanced photo-catalytic efficiency of Ti-NBs-based composites as compared to the pure Ti-NBs. For that reason the utilization of polyelectrolytes for the fabrication of films of various Ti-NBs-based composites is expected to be implemented as a promising procedure toward the development of highly efficient metal or semiconductive nanoparticles/Ti-NBs composite photocatalysts.

Finally, by combining fabrication unique properties of one-dimensional titanate-based nanostructures such as intercalation ability, surface area, porosity, morphology, dimensionality and semiconductive properties, the possibilities ensured by the use of PEM matrixes as nanoreactors for controlled synthesis of nanosized entities and achievements of the LbL method in the field of thin films, the synthesis of various multifunctional nanostructures and construction of 3D structures based on these functionalized nanostructures is expected.

6 Acknowledgements

First of all I would like to acknowledge my supervisor Prof. Dr. Danilo Suvorov for giving me an opportunity to continue my education, for his guidance, constant support and encouragement during my Ph.D study.

I would like to acknowledge my co-supervisor Assist. Prof. Dr. Boštjan Jančar for the guidance, suggestions and remarks about my work, and for introducing me to transmission electron microscopy.

Especially, I would like to thank Dr. Manca Logar for all the help particularly during the last three years of my Ph.D study. Thank you for fruitful collaboration and valuable, comprehensive discussions contributing so much to my work.

I would like to thank Damjan Vengust for helping me with characterisation of materials. Thanks for your different point of view that you share with me in many discussions and influencing my work this way.

I am also indebted to the members of my thesis committee: Prof. Dr. Miran Čeh, Prof. Dr. Maja Remškar and Prof. Dr. Dragan P. Uskoković for their comments and remarks.

Thanks to all my co-workers in the Advanced materials department and friends in other departments for their help, collaborations and company and support. Especially, thank you all for the moments we spent together in different periods of my time at the Jožef Stefan Institute.

Finally, I would like to thank my family for being there for me at any time. Thank you for your patience, constant moral support and encouragement.

7 References

[1] Bavykin, D. V. and Walsh, F. C. *Titanate and Titania Nanotubes: Synthesis, Properties and Applications* (RSCPublishing, UK, 2010).

[2] Yang, P. (ed.) *The Chemistry of Nanostructured Materials* (World Scientific Publishing Co. Pte. Ltd., Singapore, 2003).

[3] Iijima, S. Helical microtubules of graphitic carbon. *Nature* **354**, 56 (1991).

[4] Ivanovskii, A. L. Non-carbon nanotubes: synthesis and simulation. *Russian Chemical Reviews* **71**, 175 (2002).

[5] Zhu, B.; Guo, Q.; Huang, X.; Wang, S.; Zhang, S.; Wu, S.; Huang, W. Characterization and catalytic performance of TiO_2 nanotubes-supported gold and copper particles. *Journal of Molecular Catalysis A: Chemical* **249**, 211 (2006).

[6] Adachi, M.; Murata, Y.; Okada, I.; Yoshikawa, S. Formation of titania nanotubes and applicatios for dye-sentisized solar cells. *Journal of the Electrochemical Society* **150,** G488 (2003).

[7] Li, J.; Tang, Z.; Zhang, Z. Layered hydrogen titanate nanowires with novel lithium intercalation properties. *Chemistry of Materials* **17**, 5848 (2005).

[8] Yu, J.; Yu, H.; Cheng, B.; Trapalis, C. J. Effects of calcination temperature on the microstructures and photocatalytic activity of titanate nanotubes. *Journal of Molecular Catalysis A: Chemical* **249**, 135 (2006)

[9] Bavykin, D. V.; Friedrich, J. M.; Walsh, F. C. Protonated Titanates and TiO_2 Nanostructured Materials: Synthesis, Properties, and Applications. *Advanced Materials* **18**, 2807 (2006).

[10] Andersson, S.; Wadsley, A. D. The crystal structure of $Na_2Ti_3O_7$. *Acta Crystallographica* **14**, 1245 (1961).

[11] Izawa, H.; Kikkawa, S.; Kolzumi, M. Ion exchange and dehydration of layered titanates, $Na_2Ti_3O_7$ and $K_2Ti_4O_9$. *Journal of Physical Chemistry* **86**, 5023 (1982).

[12] Andersson, S.; Wadsley, A. D. The crystal structure of $Na_2Ti_6O_{13}$ and $Rb_2Ti_6O_{13}$ and the alkali metal titanates. *Acta Crystallographica* **15**, 194 (1962).

[13] Umek, P.; Cerc Korošec, R.; Jančar, B.; Dominko, R.; Arčon, D. The influence of the reaction temperature on the morphology of sodium titanate 1D nanostructures and a study of their thermal stability. *Journal of Nanoscience and Nanotechnology* **7**, 1 (2007).

[14] Kasuga, T.; Hiramatsu, M.; Hoson, A,; Sekino, T.; Niihara, K. Formation of titanium oxide nanotube. *Langmuir* **14**, 3160 (1998).

[15] Yao, B. D.; Chan, Y. F.; Zhang, X. Y.; Zhang, W. F.; Yang, Z. Y.; Wang, N. Formation mechanism of TiO_2 nanotubes. *Applied Physics Letters* **82**, 281 (2003).

[16] Zhang, M.; Jin, Z.; Zhang, J.; Guo, X.; Yang, J.; Li, W.; Wang, X.; Zhang, Z. Effect of annealing temperature on morphology, structure and photocatalytic behavior of nanotubed $H_2Ti_2O_4(OH)_2$. *Journal of Molecular Catalysis A: Chemical* **217**, 203 (2004).

[17] Yang, J.; Jin, Z.; Wang, X.; Li, W.; Zhang, J.; Zhang, S.; Guo, X.; Zhang, Z. Study on composition, structure and formation of nanotube $Na_2Ti_2O_4(OH)_2$. *Dalton*

Transactions, 3898 (2003).
[18] Chen, W.; Guo, X.; Zhang, S.; Jin, Z. TEM study on the formation mechanism of sodium titanate nanotubes. *Journal of Nanoparticle Research* **9**, 1173 (2007).
[19] Song, H.; Jiang, H.; Liu, T.; Liu, X.; Meng, G. Preparation and photocatalytic activity of alkali titanate nano materials $A_2Ti_nO_{2n+1}$ (A = Li, Na and K). *Materials Research Bulletin* **42**, 334 (2007).
[20] Chen, Q.; Zhou, W.; Du, G.; Peng, L.-M. Trititanate nanotubes made via a single alkali treatment. *Advanced Materials* **14**, 1208 (2002).
[21] Chen, Q,; Du, G. H.; Zhang, S.; Peng, L.-M. The structure of trititanate nanotubes. *Acta Crystallographica B* **58**, 587 (2002).
[22] Zhang, S.; Peng, L.-M.; Chen, Q.; Du, G. H.; Dawson, G.; Zhou, W. Z. Formation Mechanism of $H_2Ti_3O_7$ Nanotubes. *Physical Review Letters* **91**, 256103-1 (2003).
[23] Zhang, S.; Chen, Q.; Peng, L.-M. Structure and formation of $H_2Ti_3O_7$ nanotubes in an alkali environment. *Physical Review B* **71** 014104-1 (2005).
[24] Tsai, C.-C.; Teng, H. Nanotube formation from sodium titanate powder via low-temperature acid treatment. *Langmuir* **24**, 3434 (2008).
[25] Ma, R.; Fukuda, K.; Sasaki, T.; Osada, M.; Bando, Y. Structural features of titanate nanotubes/nanobelts revealed by Raman, X-ray absorption fine structure and electron diffraction characterizations. *Journal of Physical Chemistry B* **109**, 6210 (2005).
[26] Ma, R.; Bando, Y.; Sasaki, T. Nanotubes of lepidocrocite titanates. *Chemical Physical Letters* **380**, 577 (2003).
[27] Chen, Q.; Peng, L.-M. Structure and application of titanate and related nanostructures. *International Journal of Nanotechnology* **4**, 44 (2007).
[28] Du, G. H.; Chen, Q.; Che, r. c.; Yuan, Z. Y.; Peng, L.-M. Preparation and structure analysis of titanium oxide nanotubes. *Applied Physics Letters* **79**, 3702 (2001).
[29] Yuan, Z.-Y.;Su, B.-L. Titanium oxide nanotubes, nanofibres and nanowires. *Colloids and Surfaces A: Physicochemical and Engineering Aspects* **241**, 173 (2004).
[30] Sun, X.; Chen, X.; Li, Y. Large-scale synthesis of sodium and potassium titanate nanobelts. *Inorganic Chemistry Communication* **41**, 4996 (2002).
[31] Wang, B. L.; Chen, Q.; Wang, R. H.; Peng, L.-M. Synthesis and characterization of $K_2Ti_6O_{13}$ nanowires. *Chemical Physics Letters* **376**, 726 (2003).
[32] Seo D.-S.; Kim, H.; Lee, J.-K. Hydrothermal synthesis of $Na_2Ti_6O_{13}$ and TiO_2 whiskers. *Journal of Crystal Growth* **275**, e2371 (2005).
[33] Kiatkittipong, K.; Ye, C.; Scott, J.; Amal, R. Understanding hydrothermal titanate nanoribbon formation. *Crystal Growth & Design* **10**, 3618 (2010).
[34] Kolen'ko, Y. V.; Kovnir, K. A.; Gavrilov, A. I.; Garseh, A. V.; Frantti, J.; Lebedev, O. I.; Churagulov, B. R.; Van Tendeloo, G.; Yoshimura, M. Hydrothermal synthesis and characterization of nanorods of various titanates and titanium dioxide. *The Journal of Physical Chemistry B* **110**, 4030 (2006).
[35] Bavykin, D. V.; Walsh, F. C. Kinetics of alkali metal ion exchange into nanotubular and nanofibrous titanates. *The Journal of Physical Chemistry C* **111**, 14644 (2007).
[36] Yang, H. G.; Zeng, H. C. Synthetic architectures of $TiO_2/H_2Ti_5O_{11}\cdot H_2O$, ZnO/ $TiO_2/H_2Ti_5O_{11}\cdot H$, $ZnO/TiO_2/H_2Ti_5O_{11}\cdot H_2O$, and ZnO/TiO_2 nanocomposites. *Journal of American Chemical Society* **127**, 270 (2005).
[37] Mao, Y.; Wong, S. S. Size- and shape-dependent transformation of nanosized titanate into analogous anatase titania nanostructures. *Journal of American Chemical Society* **128**, 8217 (2006).
[38] Andrusenko, I.; Mugnaioli, E.; Gorelik, T. E., Koll, D.; Panthöfer, M.; Tremel, W.; Kolb, U. Structure analysis of titanate nanorods by automated electron diffraction

tomography. *Acta Crystallographica B* **67**, 218 (2011).
[39] Štengl, V.; Bakardjieva, S.; Šubrt, J.; Večerníková, E.; Szatmary, L.; Klementová, M.; Balek, V. Sodium titanate nanorods: Preparation, microstructure characterization and photocatalytic activity. *Applied Catalysis B: Environmental* **63**, 20 (2006).
[40] Yoshida, R.; Suzuki, Y.; Yoshikawa, S. Syntheses of TiO_2(B) and TiO_2 anatase nanowires by hydrothermal and post-heat treatments. *Journal of Solid State Chemistry* **178**, 2179 (2005).
[41] Bavykin, D. V.; Kulak, A. N.; Walsh, F. C. Metastable nature of titanate nanotubes in an alkaline environment. *Crystal Growth & Design* **10**, 4421 (2010).
[42] Mori, M.; Kumagai, Y.; Matsunaga, K.; Tanaka, I. First-principle investigation of atomic structures and stability of proton-exchanged layered sodium titanate. *Physical Review B* **79**, 144117 (2009).
[43] Viriya-empikul, N.; Sano, N.; Charinpanitkul, T.; Kikuchi, T.; Tanthapanichakoon, W. Astep towards length control of titanate nanotubes using hydrothermal reaction with sonication pretreatment. *Nanotechnology* **19**, 035601 (2008).
[44] Nakahira, A.; Kubo, T.; Numako, C. Formation mechanism of TiO_2-derived titanate nanotubes prepared by the hydrothermal process. *Inorganic Chemistry* **49**, 5845 (2010).
[45] Israelachvili, J. N. *Intermolecular & Surface Forces* (Academic Press Limited, UK, 1991).
[46] Bavykin, D. V.; Parmon, V. N.; Lapkin, A. A.; Walsh, F. C. The effect of hydrothermal conditions on the mesoporous structure of TiO_2 nanotubes. *Journal of Materials Chemistry* **14**, 3370 (2004).
[47] Horváth, E.; Kukovecz, Á.; Kónya, Z.; Kiricsi, I. Hydrothermal conversion of self-assembled titanate nanotubes into nanowires in a revolving autoclave. *Chemistry of Materials* **19**, 927 (2007).
[48] Huang, J.; Cao, Y.; Huang, Q.; He, H.; Liu, Y.; Guo,W.; Hong, M. High-temperature formation of titanate nanotubes and the transformation mechanism of nanotubes into nanowires. *Crystal Growth & Design* **9**, 3632 (2009).
[49] Viana, B. C.; Ferreira, O. P.; Souza Filho, A. G.; Hidalgo, A. A.; Filho, M. J.; Alves, O. L. Highlighting the mechanisms of the titanate nanotubes to titanate nanoribbons transformation. *Journal of Nanoparticle Research* **13**, 3259 (2011).
[50] Byrappa, K. and Yoshimura, M. *Handbook of Hydrothermal Technology: Technology for Crystal Growth and Materials Processing* (Noyes Publications/William Andrew Publishing, LLC, USA, 2001).
[51] Riman, R. E.; Suchanek, W. L.; Lencka, M. M. Hydrothermal crystallization of ceramics. *Annales de Chimie Science des Matériaux* **27**, 15 (2002).
[52] West, A. R. *Basic Solid State Chemistry* (John Wiley&Sons, ltd, UK, 2000).
[53] Kruse, A.; Dinjus, E. Hot compressed water as reaction medium and reactant: Properties and synthesis reactions. *The Journal of Supercritical Fluids* **39**, 362 (2007).
[54] Yoshimura, M.; Byrappa, K. Hydrothermal processing of materials: past, present and future. *Journal of Materials Science* **43**, 2085 (2008).
[55] Suchanek, W. L.; Riman, R. E. Hydrothermal synthesis of advanced ceramic powders. *Advances in Science and Technology* **45**, 184 (2006).
[56] Dawson, W. J. Hydrothermal synthesis of advanced ceramic powders. *Ceramic Bulletin* **67**, 1673 (1988).
[57] Poudel, B.; Wang, W. Z.; Dames, C.; Huang, J. Y.; Kunwar, S.; Wang, D. Z.; Banerjee, D.; Chen, G.; Ren, Z. F. Formation of crystallized titania nanotubes and their transformation into nanowires. *Nanotechnology* **16**, 1935 (2005).
[58] Sōmiya, S.; Roy, R. Hydrothermal synthesis of fine oxide powders. *Bulletin of*

Materials Science **23**, 453 (2000).
[59] Mao, Y.; Park, T.-J.; Wong, S. S. Synthesis of classes of ternary metal oxide nanostructures. *Chemical Communications* 5721 (2005).
[60] Hu, Y.; Gu, H.; Sun, X.; You, J. Photoluminescence and Raman scattering studies on PbTiO3 nanowires fabricated by hydrothermal method at low temperature. *Applied Physics Letters* **8**, 193120 (2006).
[61] Mao, Y.; Banerjee, S.; Wong, S. S. Hydrothermal synthesis of perovskite nanotubes. *Chemical Communications* 408 (2003).
[62] Huang, J.; Cao, Y.; Wang, M.; Huang, C.; Deng, Z.; Tong, H.; Liu, Z. Tailoring of low-dimensional titanate nanostructures. *The Journal of Physical Chemistry C* **114**, 14748 (2010).
[63] Wu, D.; Liu, J.; Zhao, X.; Li, A.; Chen, Y.; Ming, N. Sequence of events for the formation of titanate nanotubes, nanofibers, nanowires, and nanobelts. *Chemistry of Materials* **18**, 547 (2006).
[64] Morgan, D. L.; Triani, G.; Blackford, M. G.; Raftery, N. A.; Frost, R. L.; Waclawik, E. R. Alkaline hydrothermal kinetics in titanate nanostructure formation. *Journal of Materials Science* **46**, 548 (2011).
[65] Bavykin, D. V.; Cressey, B. A.; Light, M. E.; Walsh, F. C. An aqueous, alkaline route to titanate nanotubes under atmospheric pressure conditions. *Nanotechnology* **19**, 275604 (2008).
[66] Kamat, P. V. Photochemistry on nonreactive and reactive (semiconductor) surfaces. *Chemical Reviews* **93**, 267 (1993).
[67] Kreibing, U. and Vollmer, M. *Optical Properties of Metal Clusters* (Springer-Verlag, Germany, 1995).
[68] Kelly, K. L.; Coronado, E.; Zhao, L. L.; Schatz, G. C. The optical properties of metal nanoparticles: The influence of size, shape, and dielectric environment. *The Journal of Physical Chemistry B* **107**, 668 (2003).
[69] Achermann, M. Exciton-plasmon interaction sin metal-semiconductor nanostructures. *The Journal of Physical Chemistry Letters* **1**, 2837 (2010).
[70] Schwartzberg, A. M.; Zhang, J. Z. Novel optical properties ans emerging applications of metal nanostructures. *The Journal of Physical Chemistry C* **112**, 10323 (2008).
[71] Mie, G. Beiträge zur Optik trüber Medien, speziell kolloidaler Metallösungen. *Annalen der Physik (Leipzig)* **25**, 376 (1908).
[72] Link, S.; El-Sayed, M. A. Size and temperature dependence of the plasmon absorption of colloidal gold nanoparticles. *The Journal of Physical Chemistry B* **103**, 4212 (1999).
[73] Link, S.; El-Sayed, M. A. Shape and size dependence of radiative, non-radiative, and photothermal properties of gold nanocrystals. *International Reviews in Physical Chemistry* **19**, 409 (2000).
[74] Maier, S. A.; Atwater, H. A. Plasmonic: Localization and guiding of electromagnetic energy in metal/dielectric structures. *Journal of Applied Physics* **98**, 011101 (2005).
[75] Jain, P. K.; Huang, X.; El-Sayed, I. H.; El-Sayed, M. A. Review of some interesting surface plasmon resonance-enhanced properties of nobel metal nanoparticles and their applications to biosystems. *Plasmonics* **2,** 107 (2007).
[76] Doremus, R. H. Optical properties of small gold particles. *The Journal of Chemical Physics* **40**, 2389 (1964).
[77] Wiley, B. J.; Im, S. H.; Li, Z.-Y.; McLellan, J.; Siekkinen, A.; Xia, Y. Maneuvering the surface plasmon resonance of silver nanostructures through shape-controlled synthesis. *The Journal of Physical Chemistry B* **110**, 15666 (2006).

[78] Hutter, E.; Fendler, J. H. Exploitation of localized surface plasmon resonance. *Advanced Materials* **16,** 1685 (2004).
[79] Luther, J. M.; Jain, P. K.; Ewers, T.; Alivisatos, A. P. Localized surface plasmon resonance arising from free carriers in doped quantum dots. *Nature Materials* **10,** 361 (2011).
[80] Beecroft, L.; Ober, C. K. Nanocomposite materials for optical applications. *Chemistry of Materials* **9,** 1302 (1997).
[81] Mohanty, M.; Acharya, A.; Panda, B.; Balamurgan, S.; Pattnaik, S.; Roy, G. Characterization of ZnS quantum dot (q-dot) by ultraviolet visible (UV-VIS) absorption spectrum studies & comparison with CuO nanocrystal. *Journal of American Science* **7,** 348 (2011).
[82] Gaponenko, S. *Optical properties of semiconductor nanocrystals* (Cambridge university press, New York, 1998).
[83] Bruss, L. Chemical approaches to semiconductor nanocrystals. *Journal of Physics and Chemistry of Solids* **59,** 459 (1998).
[84] Kim, G.-S.; Ansari, S. G.; Seo, H.-K.; Kim, Y.-S.; Shin, H.-S. Effect of annealing temperature on structural and bonded states of titanate nanotube films. *Journal of Applied Physics* **101**, 024314 (2007).
[85] Yavuz, M. S.; Cheng, Y. ; Chen, J.; Cobley, C. M.; Zhang, Q.; Rycenga, M.; Xie, J.; Kim, C.; Song, K. H.; Schwartz, A. G.; Wang, L. V.; Xia, Y. Gold nanocages covered by smart polymers for controlled release with near-infrared light. *Nature Materials* **8,** 935 (2009).
[86] An, K.; Hyeon, T. Synthesis and biomedical applications of hollow nanostructures. *Nano Today* **4,** 359 (2009).
[87] Kasuga, T. Formation of titanium nanotubes using chemical treatments and their characteristic properties. *Thin Solid Films* **496,** 141 (2006).
[88] Ohtsu, N.; Sato, K.; Yanagawa, A.; Saito, K.; Imai, Y.; Kohgo, T.; Yokoyama, A.; Asami, K.; Hanawa, T. $CaTiO_3$ coating on titanium for biomaterial application-Optimum thickness and tissue response. *Journal of Biomedical Materials Research Part A* **82A,** 304 (2007).
[89] Adamopoulos, O.; Papadopoulos, T. Nanostructured bioceramics for maxillofacial applications. *Journal of Materials Science:Materials in Medicine* **18,** 1587 (2007).
[90] Bao, N.; Shen, L.; Srinivasan, G.; Yanagisawa, K.; Gupta, A. Shape-controlled monocrystalline ferroelectric barium titanate nanostructures: From nanotubes and nanowires to ordered nanostructures. *Journal of Physical Chemistry C* **112,** 8634 (2008).
[91] Maxim, F.; Ferreira, P.; Vilarinho, P. M.; Reaney, I. Haydrothermal synthesis and crystal growth studies of $BaTiO_3$ using Ti nanotube precursors. *Crystal Growth & Design* **8,** 3309 (2008).
[92] Hirakawa, T.; Kamat, P. V. Charge separation and catalytic activity of $Ag@TiO_2$ core-shell composite clusters under UV-irradiation. *Journal of American Chemical Society* **127**, 3928 (2005).
[93] Awazu, K.; Fujimaki, M.; Rockstuhl, C.; Tominaga, J.; Murakami, H.; Ohki, Y.; Yoshida, N.; Watanabe, T. A plasmonic photocatalyst consisting of silver nanoparticles embedded in titanium dioxide. *Journal of American Chemical Society* **130**, 1676 (2008).
[94] Ma, R.; Sasaki, T.; Bando, Y. Layer-by-layer assembled multilayer films of titanate nanotubes, Ag- or Au-loaded nanotubes, and nanotubes/nanosheets with polycations. *Journal of American Chemical Society* **126**, 10382 (2004).
[95] Logar, M.; Jančar, B.; Šturm, S.; Suvorov, D. Weak polyion multilayer assisted in-

situ synthesis as a route towards a plasmonic Ag/TiO_2 photocatalyst. *Langmuir* **26**, 12215 (2010).
[96] Wang, D.; Zhou, F.; Wang, C.; Liu, W. Synthesis and characterization of silver nanoparticles loaded mesoporous TiO_2 nanobelts. *Microporous and Mesoporous Materials* **116**, 658 (2008).
[97] Li, H.; Duan, X.; Liu, G.; Liu, X. Photochemical synthesis and characterization of Ag/TiO_2 nanotube composite. *Journal of Materials Science* **43**, 1669 (2008).
[98] Toledo-Antonio, J. A.; Cortes-Jácome, M. A.; Angeles-Chavez, C.; López-Salinas, E.; Quintana, P. Highly quasi-monodisperse Ag nanoparticles on titania nanotubes by impregnative aqueous ion exchange. *Langmuir* **25**, 10195 (2009).
[99] Logar, M.; Jančar, B.; Suvorov, D.; Kostanjšek, R. In situ synthesis of Ag nanoparticles in polyelectrolyte multilayers. *Nanotechnology* **18,** 325601 (2007).
[100] Logar, M.; Jančar, B.; Rečnik, A.; Suvorov, D. Controlled synthesis of pure and doped ZnS nanoparticles in weak polyion assemblies: growth characteristics and fluorescence properties. *Nanotechnology* **20,** 275601 (2009).
[101] Yoo, D.; Shiratori, S. S.; Rubner, M. F. Controlling bilayer composition and surface wettability of sequentially adsorbed multilayers of weak polyelectrolytes. *Macromolecules* **31,** 4309 (1998).
[102] Huang, Z.-Y.; Mills, G.; Hajek, B. Spontaneous formation of silver particles in basic 2-propanol. *Journal of Physical Chemistry* **97**, 11542 (1993).
[103] Weaver, J. F.; Hoflund, G. B. Surface characterization study of the thermal decomposition of AgO. *Journal of Physical Chemistry* **98**, 8519 (1994).
[104] Waterhouse, G. I. N.; Bowmaker, G. A.; Metson, J. B. The thermal decomposition of silver (I, III) oxide: A combined XRD, FT-IRand Raman spectroscopic study. *Physical Chemistry Chemical Physics* **3,** 3838 (2001).
[105] Mendelsohn, J. D.; Barrett, C. J.; Chan, V. V.; Pal, A. J.; Mayes, A. M.; Rubner, M. F. Fabrication of microporous thin films from polyelectrolyte multilayers. *Langmuir* **16**, 5017 (2000).
[106] Bowker, M., Broughton, M.; Carley, A.; Davies, P.; Morgan, D.; Crouch, J. Influence of thermal treatment onnanostructured gold model catalysts. *Langmuir* **26**, 16261 (2010).
[107] Bavykin, D. V.; Gordeev, S. N.; Moskalenko, A. V.; Lapkin, A. A.; Walsh, F. C. Apparent two-dimensional behavior of TiO_2 nanotubes revealed by light absorption and luminescence. *The Journal of Physical Chemistry B: Letters* **109,** 8565 (2005).
[108] Riss, A.; Berger, T.; Grothe, H.; Bernardi, J.; Diwald, O.; Knölzinger, E. Chemical control of photoexcited states in titanate nanostructures. *Nano Letters* **7,** 433 (2007).
[109] Hutter, E.; Fendler, J. H. Exploitation of localized surface Plasmon resonance. *Advanced Materials* **16,** 1685 (2004).
[110] Eustis, S.; El-Sayed, M. A. Whay gold nanoparticles are more precious than pretty gold: Noble metal surface Plasmon resonance and its enhancement of the radiative and nonradiative properties of nanocrystals of different shapes. *Chemical Society Reviews* **35,** 209 (2006).
[111] Kreibing, U. and Vollmer, M. *Optical Properties of Metal Clusters* (Springer Series in Materials Science vol. 25, Springer, Berlin, 1995).
[112] Son, H.-S.; Lee, S.-J.; Cho, I.-H.; Zoh, K.-D. Kinetics and mechanism of TNT degradation in TiO_2 photocatalysis. *Chemosphere* **57,** 309 (2004).
[113] Wu, C.-H.; Chern, J.-M- Kinetics of photocatalytic decomposition of methylene blue. *Industrial & Engineering Chemistry Research* **45,** 6450 (2006).
[114] Tachikawa, T.; Tojo, S.; Fujitsuka, M.; Sekino, T.; Majima, T. Photoinduced charge separation in titania nanotubes. *The Journal of Physical Chemistry B: Letters* **110,**

14055 (2006).
[115] Riss, A.; Elser, M. J.; Bernardi, J.; Diwald, O. Stability and photoelectronic properties of layered titanate nanostructures. *Journal of American Chemical Society* **131**, 6198 (2009).
[116] Bavykin, D. V.; Walsh, F. C. Elongated titanate nanostructures and their applications. *European Journal of Inorganic Chemistry* 977 (2009).
[117] Subramanian, V.; Wolf, E. E.; Kamat, P. V. Catalysis with TiO_2/gold nanocomposites. Effect of metal particle size in the Fermi level equilibration. *Journal of American Chemical Society* **126**, 4943 (2004).
[118] Chatterjee, D.; Dasgupta, S.; Rao, N. N. Visible light assisted photodegradation of halocarbons on the dye modified TiO_2 surface using visible light. *Solar Energy Materials & Solar Cells* **90,** 1013 (2006).
[119] Zhang, S.; Chen, Y.; Yu, Y.; Wu, H.; Wang, S.; Zhu, B.; Huang, W.; Wu, S. Synthesis, characterization of Cr-doped TiO_2 nanotubes with high photocatalytic activity. *Journal of Nanoparticle Research* **10,** 871 (2008).
[120] Ding, X.; Xu, X. G.; Chen, Q.; Peng, L.-M. Preparation and characterization of Fe-incorporated titanate nanotubes. *Nanotechnology* **17,** 5423 (2006).
[121] Zhang, H.; Wang, G.; Chen, D.; Lv, X.; Li, J. Tuning photoelectrochemical performances of Ag-TiO_2 nanocomposites via reduction/oxidation of Ag. *Chemistry of Materials* **20,** 6543 (2008).
[122] Liu, H.; Ma, H. T.; Li, W. Z.; Wu, M.; Bao, X. H. The enhancement of TiO_2 photoctatalytic activity by hydrogen thermal treatment. *Chemosphere* **50,** 39 (2003).
[123] Yu, J. C.; Lin, J.; Lo, D.; Lam, S. K. Influence of thermal treatment on the adsorption of oxygen and photocatalytic activity of TiO_2. *Langmuir* **16,** 7304 (2000**)**.
[124] Bračko, I.; Jančar, B.; Logar, M.; Caglič, D.; Suvorov, D. Silver nanoparticles on titanate nanobelts via the self-assembly of weak polyelectrolytes: synthesis and photocatalytic properties. *Nanotechnology* **22,** 085705 (2011).
[125] Jiang, J.; Gao, Q.; Chen, Z.; Hu, J.; Wu, C. Syntheses, characterization and properties of novel nanostructures consisting of Ni/titanate and Ni/titania. *Materials Letters* **60,** 3803 (2006).
[126] Zhang, M.; Gong, K.; Zhang, H.; Mao, L. Layer-by-layer assembled carbon nanotubes for selective determination of dopamine in the presence of ascorbic acid. *Biosensors and Bioelectronics* **20,** 1270 (2005).
[127] Kommireddy, D. S.; Patel, A. A.; Shutava, T. G.; Mills, D. K.; Lvov, Y. M. Layer-by-layer assembly of TiO_2 nanoparticles for stable hydrophilic biocompatible coatings. *Journal of Nanoscience and Nanotechnology* **5,** 1081 (2005).
[128] He, P.; Hu, N.; Rusling, J. F. Driving forces for layer-by-layer self-assembly of films of SiO_2 nanoparticles and heme proteins. *Langmuir* **20,** 722 (2004).
[129] Crespo-Biel, O.; Dordi, B.; Reinhoudt, D. N.; Huskens, J. Supramolecular layer-by-layer assembly: alternating adsorptions of guest- and host-functionalized molecules and particles using multivalent supramolecular interactions. *Journal of American Chemical Society* **127,** 7594 (2005).
[130] Schoeler, B.; Kumaraswamy, G.; Caruso, F. Investigation of the influence of polyelectrolyte charge density on the growth of multilayer thin films prepared by the layer-by-layer technique. *Macromolecules* **35,** 889 (2002).
[131] Kovtyukhova, N. I.; Ollivier, P. J.; Martin, B. R.; Mallouk, T. E.; Chizhik, S. A.; Buzaneva, E. V.; Gorchinskiy, A. D. Layer-by-layer assembly of ultrathin composite films from micron-sized graphite oxide sheets and polycations. *Chemistry of Materials* **11,** 771 (1999).

Index of Figures

Index of Tables

Appendix

Publications

Original scientific articles

1. Veselinović, L.; Karanović, L.; Stojanović, Z.; Bračko, I.; Marković, S.; Ignjatović, N.; Uskoković, D. Crystal structure of cobalt-substituted calcium hydroxyapatite nanopowders prepared by hydrothermal processing. *Journal of Applied Crystallography* **43,** 320 (2010).

2. Žunič, V.; Škapin, S. D.; Maček, M.; Bračko, I.; Sever Škapin, A.; Suvorov, D. Influence of the triblock copolymer P123 and phosphorous on the physico-chemical properties of TiO_2. *Applied Catalysis A: General* **397**, 241 (2011).

3. Marković, S.; Veselinović, L.; Lukić, M.; Karanović, L.; Bračko, I.; Ignjatović, N.; Uskoković, D. Synthetical bone-like and biological hydroxyapatites : a comparative study of crystal structure and morphology. *Biomedical materials* **6,** 045005-1 (2011).

4. Vukomanović, M.; Zavašnik-Bergant, T.; Bračko, I.; Škapin, S. D.; Ignjatović, N.; Radmilović, V.; Uskoković, D. Poly(D,L-lactide-co-glycolide)/hydroxyapatite core-shell nanosphere. Pt. 3, Properties of hydroxyapatite nano-rods and investigation of a distribution of the drug within the composite. *Colloids and Surfaces B: Biointerfaces*. **87,** 226 (2011).

5. Vukomanović, M.; Bračko, I.; Poljanšek, I.; Uskoković, D.; Škapin, S. D.; Suvorov, D. The growth of silver nanoparticles and their combination with hydroxyapatite to form composites via a sonochemical approach. *Crystal Growth & Design* **11,** 3802 (2011), vol. 11, issue 9, pp 3802-3812.

6. Bračko, I.; Jančar, B.; Logar, M.; Caglič, D.; Suvorov, D. Silver nanoparticles on titanate nanobelts via the self-assembly of weak polyelectrolytes: synthesis and photocatalytic properties. *Nanotechnology* **22,** 085705-1 (2011).

7. Stevanović, M.; Savanović, I.; Uskoković, V.; Škapin, S. D.; Bračko, I.; Jovanović, U.; Uskoković, D. A new, simple, green, and one-pot four-component synthesis of bare and poly([alpha],[gamma],L-glutamic acid)-capped silver nanoparticles. *Colloid & Polymer Science* **290,** 221 (2012).

8. Lukić, M.; Veselinović, L.; Maček, M.; Bračko, I.; Škapin, S. D.; Marković, S.; Uskoković, D. Peculiarities in sintering behavior of Ca-deficient hydroxyapatite

nanopowders. *Materials Letters* **68,** 331 (2012).

9. Stevanović, M.; Škapin, S. D.; Bračko, I.; Milenković, M.; Petković, J.; Filipič, M.; Uskoković, D. Poly(lactide-co-glycolide)/silver nanoparticles : synthesis, characterization, antimicrobial activity, cytotoxicity assessment and ROS-inducing potential. *Polymer (Guildf)* **31,** in press (2012).

10. Bianchetti, M.; Bračko, I.; Škapin, S. D.; Walsöe De Reca, N. E. Nanocrystalline Tin oxide to be applied in a gas sensor. *Sensors and Transducers Journal* **137,** 155 (2012). http://www.sensorsportal.com/HTML/DIGEST/P_933.htm.

Published scientific conference contribution

11. ŠTURM, Sašo, JANČAR, Boštjan, BRAČKO, Ines. Towards understanding the hydrothermal synthesis of nanostructured $CaTiO_3$: HRTEM and EELS study. V: NEBESÁŘOVÁ, Jana (ed.), HOZÁK, Pavel (ed.). 8th Multinational Congress on Microscopy, June 17-21, 2007, Prague, Czech Republic. *Proceedings: Czechoslovak Microscopy Society*, 165 (2007).

12. BRAČKO, Ines, LOGAR, Manca, JANČAR, Boštjan, SUVOROV, Danilo. Cu decorated titanate nanobelts composite thin film for photo-catalytic applications. November 1-3, 2011, New York, NY. *Nanotechnology 2011: conference and workshops, [S. l.: s. n.]* 55 (2011).

Published scientific conference contribution abstracts

13. BRAČKO, Ines, JANČAR, Boštjan, ŠTURM, Sašo, SUVOROV, Danilo. Razumevanje nastanka nanostrukturnega perovskita $CaTiO_3$ pod hidrotermalnimi pogoji = Understanding the formation of nanostructured perovskite $CaTiO_3$ under hydrothermal conditions. *Materiali in tehnologije* **41,** 317 (2007).

14. BRAČKO, Ines, JANČAR, Boštjan, ŠTURM, Sašo, SUVOROV, Danilo. Razumevanje nastanka nanostrukturnega perovskita $CaTiO_3$ pod hidrotermalnimi pogoji (Understanding the formation of nanostructured perovskite $CaTiO_3$ under hydrothermal conditions). JENKO, Monika (ed.). 15. konferenca o materialih in tehnologijah = 15^{th} Conference on Materials and Technology, 8-10 October, 2007 Portorož, Slovenia. *Program in knjiga povzetkov* (Inštitut za kovinske materiale in tehnologije, Ljubljana (2007), pp 50).

15. ŠTURM, Sašo, JANČAR, Boštjan, BRAČKO, Ines. EELS/HRTEM characterization of phases obtained during the hydrotermal synthesis of CaTiO[sub]3. V: USKOKOVIĆ, Dragan (ed.). Ninth Annual Conference of the Yugoslav Materials Research Society YUCOMAT 2007, Herceg Novi, September 10-14, 2007. *Programme and the book of abstracts* (Institute of Technical Sciences of SASA, Belgrade, 2007, pp 145).

16. JANČAR, Boštjan, BRAČKO, Ines, ŠTURM, Sašo, SUVOROV, Danilo. Calcium titanate nanostructures synthesized from hydrothermally derived templates. V: NANO - 2008, 9th International Conference on Nanostructured Materials, 01-06 June 2008, Rio de Janeiro, Brazil. *Abstracts*. [S. l.: s. n.], 2008, pp 364.

17. BRAČKO, Ines, JANČAR, Boštjan, ŠTURM, Sašo, SUVOROV, Danilo. Synthesis and characterization of Ca^{2+}-exchanged Na-Ti-based nanotubes. V: MIHAILOVIĆ, Dragan (ed.), KOBE, Spomenka (ed.), REMŠKAR, Maja (ed.), JAMNIK, Janko (ed.), ČOPIČ, Martin (ed.), DROBNE, Damjana (ed.). *Hot nano topics 2008 : incorporating SLONANO 2008, 3 overlapping workshops on current hot subjects in nanoscience, 23-30 May, Portorož, Slovenia: abstract book*. Ljubljana: [s. n.], 2008, pp 126.

18. BRAČKO, Ines, JANČAR, Boštjan, ŠTURM, Sašo, SUVOROV, Danilo. The synthesis and characterization of Ca-Ti-based one-dimensional nanostructures. V: USKOKOVIĆ, Dragan (ed.). Tenth Annual Conference of the Yugoslav Materials Research Society YUCOMAT 2008, Herceg Novi, Montenegro, September 8-12, 2008. *Programme and the book of abstracts* (Institute of Technical Sciences of SASA, Belgrade, 2008, pp 134).

19. JEVTIĆ, Marija, MITRIĆ, Miodrag, ŠKAPIN, Srečo D., BRAČKO, Ines, IGNJATOVIĆ, Nenad, USKOKOVIĆ, Dragan. Ultrasonic deagglomeration and particle size reduction of hyroxyapatite by coating with poly(D, L-lactide-CO-glycolide). USKOKOVIĆ, Dragan (ed.). Tenth Annual Conference of the Yugoslav Materials Research Society YUCOMAT 2008, Herceg Novi, Montenegro, September 8-12,2008. *Programme and the book of abstracts* (Institute of Technical Sciences of SASA, Belgrade, 2008, pp 158).

20. BRAČKO, Ines, JANČAR, Boštjan, ŠTURM, Sašo, SUVOROV, Danilo. The formation of 1D nanostructures calcium titanates bt the hydrothermal tretament of sodium titanate 1D nanostructured precursors. KOBE, Spomenka (ed.), ŽUŽEK ROŽMAN, Kristina (ed.), NOVAK, Saša (ed.), FIDLER, Sanja (ed.). *WomenInNano winter school: 7-9 February 2008, Kranjska Gora, Slovenia : abstract book*. [S.l.: s.n.], 2008, pp 48.

21. BRAČKO, Ines, JANČAR, Boštjan, ŠTURM, Sašo, SUVOROV, Danilo. Hidrotermalna priprava in karakterizacija Ca - Ti nanostruktur (Hydrothermal synthesis and characterization of Ca - Ti based nanostructures). GLAVIČ, Peter (ed.), BRODNJAK-VONČINA, Darinka (ed.). Slovenski kemijski dnevi 2008, Maribor, 25. in 26. september 2008. *Zbornik povzetkov referatov s posvetovanja* (FKKT, Maribor, 2008, pp 40).

22. BRAČKO, Ines, JANČAR, Boštjan, SUVOROV, Danilo. Hidrotermalna sinteza in karakterizacija titanatnih nanocevk. ISKRA, Jernej (ed.), MILOŠEV, Ingrid (ed.). *Dan mladih raziskovalcev 2009* (Institut "Jožef Stefan", Ljubljana, 2009, pp1).

23. BRAČKO, Ines, JANČAR, Boštjan, SUVOROV, Danilo. Hydrothermal synthesis of modified titanate-based one-dimensional nanostructures. SRDIĆ, Vladimir V. (ed.), RANOGAJEC, Jonjaua (ed.). The Eighth Students' Meeting Processing and

Application of Ceramics, SM 2009, December 2-5, 2009, Novi Sad, Serbia. *Programme and book of abstracts* (Faculty of Technology, University of Novi Sad, Novi Sad, 2009, pp 40).

24. BRAČKO, Ines. The formation of nanostructured $CaTiO_3$ by the hydrothermal treatment of Na-Ti-based one-dimensionally nanostructured precursor. ŠETINA, Barbara (ed.), JUNKAR, Ita (ed.), KALUŽA, Boštjan (ed.), ELERŠIČ, Kristina (ed.). 1. študentska konferenca Mednarodne podiplomske šole Jožefa Stefana, 19.-20. maj 2009, Ljubljana, Slovenija = 1st Jožef Stefan International Postgraduate School Student's Conference, 19th-20th May 2009, Ljubljana, Slovenia. *Zbornik prispevkov* (Mednarodna podiplomska šola Jožefa Stefana, Ljubljana, 2009, pp 6-7).

25. BRAČKO, Ines, VEBER, Asja, OTONIČAR, Mojca, ŠETINC, Tina, DOŠLER, Urban, ŽUNIČ, Vojka. Predstavitev mladih raziskovalcev Odseka za raziskave sodobnih materialov. ŠETINA, Barbara (ed.), JUNKAR, Ita (ed.), KALUŽA, Boštjan (ed.), ELERŠIČ, Kristina (ed.). 1. študentska konferenca Mednarodne podiplomske šole Jožefa Stefana, 19.-20. maj 2009, Ljubljana, Slovenija = 1st Jožef Stefan International Postgraduate School Student's Conference, 19th-20th May 2009, Ljubljana, Slovenia. *Zbornik prispevkov* (Mednarodna podiplomska šola Jožefa Stefana, Ljubljana, 2009, pp 8-9).

26. BRAČKO, Ines, LOGAR, Manca, JANČAR, Boštjan, SUVOROV, Danilo. Ag-titanate nanofibers composite prepared via polyelectrolyte multilayers. NANO 2010, X^{th} International Conference on Nanostructured Materials, Roma, Italy, September 13-17, 2010. *Abstract book* ([S. l.: s. n.], 2010, pp 231).

27. BRAČKO, Ines, LOGAR, Manca, JANČAR, Boštjan, SUVOROV, Danilo. Ag nanoparticles on titanate nanobelts via self-assembly of weak polyelectrolytes. MIHAILOVIĆ, Dragan (ed.), HOČEVAR, Samo B. (ed.), ARČON, Denis (ed.), KUNEJ, Špela (ed.), UMEK, Polona (ed.), KNAVS, Martina (ed.). *Book of abstracts: SLONANO 2010, 20-22 October 2010, Ljubljana, Slovenia* (National Institute of Chemistry, Ljubljana, 2010, pp 17).

28. BRAČKO, Ines, JANČAR, Boštjan, SUVOROV, Danilo. Nanostrukture pripravljene na osnovi 1D nanostrukturiranih alkalijskih titanatov. KUŠČER, Danjela (ed.), PERC, Branka (ed.). 4. Dan Mladih Raziskovalcev KMBO, Ljubljana, Slovenija, 11.2.2010. *Program in povzetki* (Institut "Jožef Stefan", Ljubljana, 2010).

29. VUKOMANOVIĆ, Marija, BRAČKO, Ines, ŠKAPIN, Srečo D., SUVOROV, Danilo, USKOKOVIĆ, Dragan. Sonochemical synthesis of silver nanoparticles and silver/hydroxyapatite nanocomposites. USKOKOVIĆ, Dragan (ed.). Twelfth Annual Conference YUCOMAT 2010, Herceg Novi, Montenegro, September 6-10, 2010. *Programme and the book of abstracts* (Institute of Technical Sciences of the Serbian Academy of Sciences & Arts, Belgrade, 2010, pp 63).

30. STANKOVIĆ, A., STOJANOVIĆ, Z., ŠKAPIN, Srečo D., BRAČKO, Ines, USKOKOVIĆ, Dragan. Influence of ZnO nanoparticles size and morphology on antibacterial activity against Eschericia coli and Staphylococus aureus. USKOKOVIĆ, Dragan (ed.). Twelfth Annual Conference YUCOMAT 2010, Herceg Novi,

Montenegro, September 6-10, 2010. *Programme and the book of abstracts* (Institute of Technical Sciences of the Serbian Academy of Sciences & Arts, Belgrade, 2010, pp 91).

31. BRAČKO, Ines. Hidrotermalna sinteza fotokatalitsko aktivnih alkalijskih titanatnih nanocevk. KALUŽA, Boštjan (ed.), ELERŠIČ, Kristina (ed.), POGORELC, Bogdan (ed.), ŠETINA, Barbara (ed.), VAHČIČ, Mitja (ed.). 2. študentska konferenca Mednarodne podiplomske šole Jožefa Stefana = 2nd Jožef Stefan International Postgraduate School Students Conference, 27. maj 2010, Ljubljana, Slovenija. *Zbornik prispevkov* (Mednarodna podiplomska šola Jožefa Stefana, Ljubljana, 2010, pp 44).

32. ŽUNIČ, Vojka, BRAČKO, Ines, OTONIČAR, Mojca, ŠETINC, Tina, VUKOMANOVIĆ, Marija. Development of materials for industrial applications. KALUŽA, Boštjan (ed.), ELERŠIČ, Kristina (ed.), POGORELC, Bogdan (ed.), ŠETINA, Barbara (ed.), VAHČIČ, Mitja (ed.). 2. študentska konferenca Mednarodne podiplomske šole Jožefa Stefana = 2nd Jožef Stefan International Postgraduate School Students Conference, 27. maj 2010, Ljubljana, Slovenija. *Zbornik prispevkov* (Mednarodna podiplomska šola Jožefa Stefana, Ljubljana, 2010, pp 76).

33. BRAČKO, Ines. Fotokatalitsko aktivni nanokompozit na osnovi Ag nanodelcev in titanatnih nanotrakov. PRIBOŠIČ, Irena (ed.), KRNEL, Kristoffer (ed.). 5. dan mladih raziskovalcev, Ljubljana, Februar 2011. *Program in povzetki* (Institut "Jožef Stefan", Ljubljana, 2011, pp 67).

34. LENART, Alenka, BRAČKO, Ines, PLODINEC, Milivoj, ŠTURM, Sašo, MIRTIČ, Breda. Formation mechanism of [alpha]-quartz from opal-a by hydrothermal synthesis : [presented at Joint 5th Mineral Sciences In The Carpathians Conference (MSCC) and 3rd Central-European Mineralogical Conference (CEMC) Miskolc, Hungary, 19-21 April 2012]. *Acta Mineralogica Petrographica, Abstract series* **7,** 78 (2012).

35. LENART, Alenka, BRAČKO, Ines, PLODINEC, Milivoj, ŠTURM, Sašo, MIRTIČ, Breda. Development of [alpha]-quarz crystals from opal-A at hydrothermal conditions. ŽAGAR, Kristina (ed.), LENART, Alenka (ed.), PEČKO, Darja (ed.). 6th Young Researcher's Day 2012, 27 and 28 febraury, 2012, Ljubljana. *Program and abstract book (*Jožef Stefan Institute, Department of Nanostructured Materials, Ljubljana, 2012, pp 34).